Electronic Thesis and Dissertation Repository

4-29-2016 12:00 AM

In-situ Ultrasound Calibration

Azharhosein Faraz
The University of Western Ontario

Supervisor
Dr. Terry M. Peters
The University of Western Ontario

Recommended Citation

Abstract

In minimally invasive navigated mitral valve repair surgery, the spatial calibration of the trans-esophageal echocardiography (TEE) ultrasound probe to the magnetic tracking system is an essential requisite. The standard calibration approach requires scanning a specialized phantom prior to the surgery, which is associated with the scaling mismatch issue. Preoperative estimation of the speed-of-sound at the target site of surgery is impractical as it varies among individual patients, leading to significant calibration errors during surgery.

In order to resolve this issue, we propose an un-precedented method of 'in-situ' ultrasound calibration, utilizing the tracked surgical tool, which is scanned by the bi-plane ultrasound while the tool is introduced into the left ventricle of the heart. In this method the ultrasound probe is calibrated based on the high-quality 2D bi-plane images, and the ultrasound reflection of the tool is being automatically segmented. In addition, we propose an 'online 3D' ultrasound calibration, which is derived from the bi-plane calibration followed by the fixed relationship between the TEE bi-plane and the 3D coordinate systems. The intrinsic transform is inferred based on the internal parameters of the imaging system. Note that calibration of the bi-plane and 3D ultrasound imaging modes are essential throughout the surgical procedure for the targeting and positioning tasks. Our approach achieved sub-millimeter accuracy in a simulated surgical environment and compensated for the correct speed-of-sound of the target medium. This was obtained within the limited range of movement available for manipulating the tool and the TEE probe during the process.

Keywords: In-situ ultrasound calibration, bi-plane ultrasound imaging, trans-apical mitral valve surgery, 3D ultrasound calibration.

Acknowlegements

First of all, I would like to thank my supervisor, Dr. Terry Peters, for having me as his graduate student and I am honored about that. I gratefully appreciate you, for your guidance, support and patience during my time in your lab. After pursuing my study in your lab, I am even more interested and intrigued by the field of image guidance than ever before. I have learned a lot throughout this time and I hope that I can apply them effectively in future.

I also would like to thank my mentor, Dr. Elvis Chen, for his tremendous help and advice throughout my Masters program. We have had a lot of discussions over different topics and this gave me the opportunity to gain enormous insights. Thank you for your contribution, you have my complete appreciation.

Special thanks to John Moore, for your suggestions, advice and help over the course of my study, in particular, in developing the phantoms for my project. To, Dr. Ali Khan, thank you for your suggestions, encouragement and guidance as a member of my advisory committee. I thank you, Dr. Xiongbiao Luo, for your friendly discussions during coffee breaks and invaluable advice. I have learned a lot from you.

I am particularly grateful to Jonathan McLeod, for your assistance and useful scientific discussions along the way. Thanks for your patience over my many questions. To Uditha Jayarathne, thank you for your great and kind advice and discussions about many different things during my study. I am honored to call you my friend. To Loxlan Kasa, Utsav Pardasani, Adam Rankin, Golafsoun Ameri and other members of the Peters lab, thank you for your support. I would also like to thank, Dr. David Tessier, Dr. Jiro Inoue and Dr. Ali Tavallaei. Also, thanks to all of my great friends at Robarts and UWO.

Last, but certainly not the least, I would like to thank my Mom, Dad and my brother for their love, encouragement and support all the time. I am always thankful for having them and could not get to where I am without them.

Dedication

This dissertation is dedicated to my parents and my younger brother.

Contents

List of Figures

ix

xi

List of Tables

List of Abbreviations

MRI	Magnetic Resonance Imaging
CT	Computed Tomography
Hz	Hertz
A-mode	Amplitude mode
1D	One-Dimensional
B-mode	Brightness mode
FOV	Field of View
2D	Two-Dimensional
3D	Three-Dimensional
4D	Four-Dimensional
DOF	Degrees of Freedom
TTE	Transthoracic Echocardiography
TEE	Trans-esophageal Echocardiography
IGS	Image Guided Surgery
CAS	Computer-Assisted Surgery
CABG	Coronary Artery Bypass Grafting
PVs	Pulmonary Veins
AF	Atrial Fibrillation
ASDFs	Atrial Septal Defects
VSDs	Ventricular Septal Defects
PFO	Patent Foramen Ovale
MV	Mitral Valve
DMVD	Degenerative Mitral Valve Disease
LV	Left Ventricle
MTS	Magnetic Tracking System
FG	Field Generator
RMS	Root Mean Square
FRE	Fiducial Registration Error
TRE	Target Registration Error
FLE	Fiducial Localization Error
TLE	Target Localization Error
SD	Standard Deviation
RP	Reconstruction Precision
AV	Augmented Virtuality
AR	Augmented Reality

OR	Operating Room
CS RT	Corrected Scale, solves for Rotation and Translation Parameters
RTS	Solves for Rotation, Translation and Scaling Parameters
VR	Volume Reconstruction
PR	Point Reconstruction
ROI	Region of Interest
RHT	Randomized Hough Transform

List of Symbols

c	Speed of Sound
k	compressibility
p	pressure
v	velocity
S	area
I_r	Reflection of incident energy
Z	Impedance
R	Rotation Matrix, 3×3
t	Translation Matrix, 3×1
S_x	Scale in x direction
‖ . ‖	Euclidean distance between the two points
^bT_a	A transformation matrix, mapping (a) to (b)
N	Number
P_{US}	Fiducial or Target Points

Chapter 1

Introduction

1.0.1   Ultrasound Imaging

Ultrasound is the most commonly used diagnostic imaging modality, covering about 25% of all imaging examinations performed worldwide on a daily basis since the beginning of the twenty-first century [19]. The advantages of ultrasound over other imaging modalities, such as MRI and CT, is in terms of its portability, cost, the non-ionizing nature of ultrasound waves, and the ability to produce real-time images of moving structures (e.g. a beating heart).

Ultrasound is a range of sound beyond human hearing, with frequencies above 20,000 Hertz (Hz). The frequency of diagnostic ultrasound typically ranges between 1-30 MHz, and the choice of frequency in ultrasound imaging varies depending on the application. Higher spatial resolution is attainable with shorter wavelengths (i.e. wavelength being inversely proportional to the frequency). However higher frequency causes greater attenuation (loss of signal strength) resulting in shorter depth of penetration.

In ultrasound imaging the key concept is the 'pulse-echo' principle. A short burst of ultrasound is emitted from a transducer and directed into the tissue. As a result of the sound's interaction with the tissue, echoes are produced, and some of them travel back to the transducer. The time delay between the emission of the pulse and the reception of the echo allows for the measurement of the distance between the transducer and the echo-producing structure
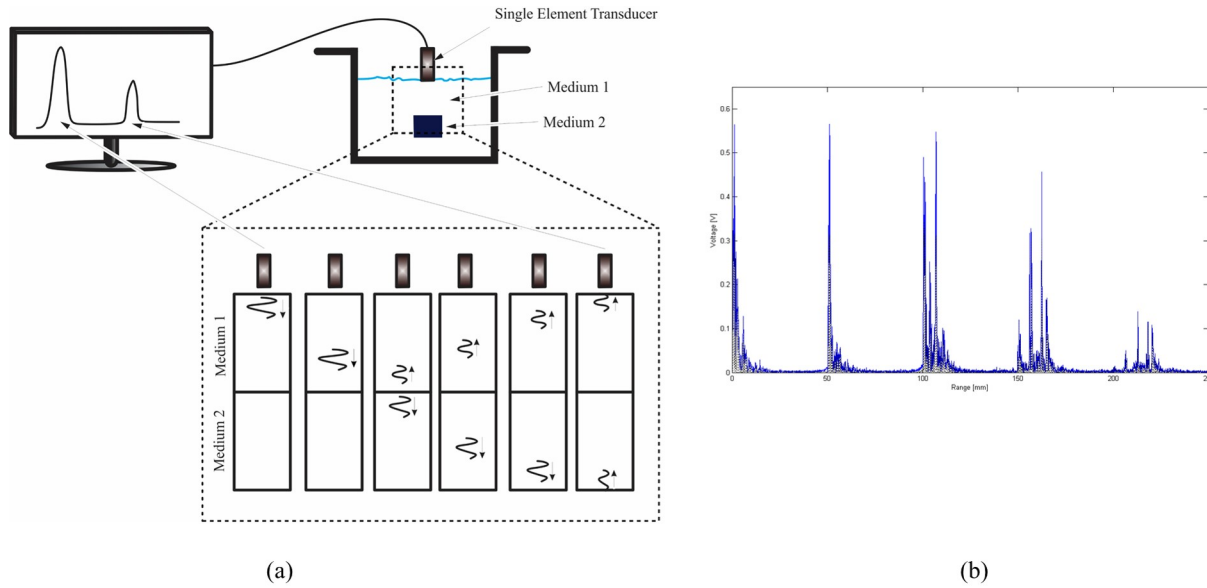
Figure 1.1: (a) Schematic diagram describing A-Mode ultrasound. (b) Real A-mode data.

and therefore helps in the formation of an image. Echoes are generated based on the differences between acoustic impedance of the tissue, which depends on its density and the speed at which sound propagates. Therefore, ultrasound fundamentally maps the mechanical property of a tissue.

Acoustic impedance of any two structures within a tissue might be slightly different and that cause only a small proportion of the ultrasound pulse to reflect back towards the transducer. Echoes arriving back are separated in time in proportion to the distance between the structures. Amplitude mode or A-mode display consists of a 1D trace where the pattern of display appears as spikes (See Fig.1.1). The amplitude of the reflected echoes corresponds to the height of the spikes. The distance between the two spikes represents the time taken by an echo to return to the transducer. On the other hand, an image can be formed based on a large number of pulse-echo acquisitions, incrementing the scan-line direction between each pulse-echo operation, which is known as B-mode (**B**rightness **mode**) imaging. In a B-mode, the amplitude of the reflected signal is displayed as bright dots along the line of sight. The term B-mode imaging means that the echo magnitude from each point in the field of view is mapped as a gray scale value for each pixel in an image.

1.0.2 Sound Wave Propagation

The tissue is a medium for propagation of the sound wave, where an exchange of the kinetic energy and the potential energy occurs. The propagation of the wave in the tissue is based on the alternate compression and decompression of tissue particles. The propagation of a wave is basically the propagation of pressure, represented by $p(x, t)$, where x is the position and t the time at which the pressure is measured. Waves are often longitudinal in the biological tissue and in the homogeneous media, without the attenuation they can be described by a one-dimensional, second order differential equation:

$$\frac{\partial^2 p(x, t)}{\partial x^2} - \frac{1}{c^2}\frac{\partial^2 p(x, t)}{\partial t^2} = 0, \tag{1.1}$$

where the pressure is proportional to the speed of sound (c) in the medium. Therefore by using the medium compressibility k [Pa^{-1}], the speed of sound can be computed based on the density of the medium as follows:

$$c = \frac{1}{\sqrt{k\rho}} \tag{1.2}$$

The acoustic properties of the medium are characterized by the acoustic impedance, defined as the pressure (p) per velocity (v) per area (S). When the wave propagates into the tissue, some portion of the incident energy may reflect (I_r) while the other portion is transmitted (I_t). Consider a plane wave traveling in a medium with speed-of-sound (c_1) and the acoustic Z of (Z_1) incidents with the second medium of sound speed (c_2) and impedance (Z_2) (See Fig.1.2). Snell's law explains the relation between the angles of incidence (θ_i), reflection (θ_r) and transmission (θ_t):

$$\sin \theta_t = \frac{c_2}{c_1} \sin \theta_i \tag{1.3}$$

$$\theta_r = \theta_i \tag{1.4}$$

Once the wave transmits into the second medium, if $c_1 > c_2$, the wave bends towards the normal, and if $c_1 < c_2$, it bends away from the normal. This change in direction is termed
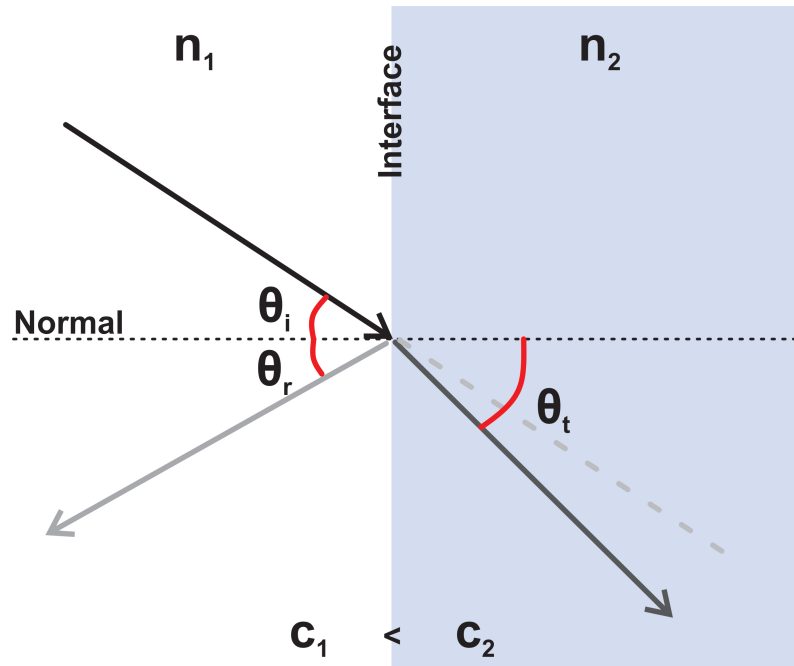
Figure 1.2: Schematic diagram of a sound wave transmitted from the lower to the higher speed-of-sound medium ($C_1 < C_2$).

refraction and can be an important source of artifact in some imaging applications.

1.0.3   Transducer Array System

In early B-mode imaging systems, a transducer was mounted on a position-sensing arm, such that the line of view of the acoustic beam could be made to correspond with the orientation of the brightness modulated A-scan line on the display screen. By moving the arm across the object of interest (e.g. patient's skin) it produced a series of dots that corresponded to the cross-section of the interface within the tissue. Thus a B-mode image was formed.

In modern ultrasound systems, the array transducers use high-speed electronic focusing and beam-steering methods to achieve high frame rates for producing an image. Beam-steering increments the direction of the scan line to sweep out the B-mode field of view (FOV). However, in modern ultrasound transducers beam-steering technology differs slightly depending on the type of the array used. There are three main types of arrays commonly used for producing the 2D images: linear array, curvilinear array, and phased array transducers.
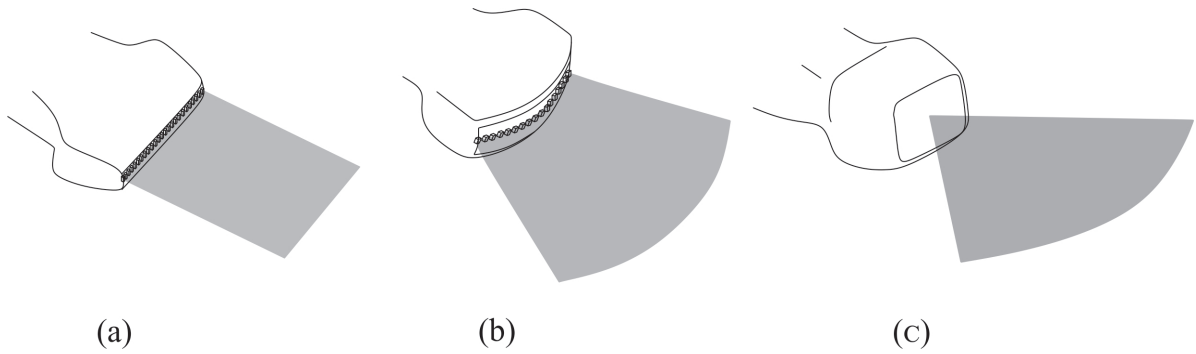
Figure 1.3: Ultrasound transducer of different geometry (a) linear array (b) curvilinear array (c) phased array.

A **linear array** consists of as many as 256 elements arranged in a line. In this type of array, each pulse-echo operation is performed by selecting a small *subaperture* of the adjacent element. The scan line is usually directed along the axial dimension of the image, perpendicular to the array and from the center of the active subaperture. The scan line goes across the face of the array and once all the echoes have been received along the resulting line, the next pulse is issued from the adjacent series of elements. The movement of the beam from the first to the last element of the transducer forms an image. A rectangular FOV whose lateral width equals the length of the array results from this procedure (Fig.1.3a). The second type is the **curvilinear array** transducer, which is similar to the linear array with the only difference that the face of the array is convex rather than linear. This allows the scan line to be translated laterally and rotate in an azimuth angle. Thus a sector image is produced (Fig.1.3b).

The **phased array** transducer produces a sector format image by controlling the timing at which each element in a small rectangular array of transducers is excited (Fig.1.3c). The array sizes in this type of transducers are usually as low as 48 and up to 128 elements. Elements in this format excite simultaneously with a small delay or phase difference between each of them. The beam is steered electronically by controlling the phase between repeated bursts, which is achieved by using an independent electronic delay circuit for each element of the transducer. Then, delays are applied to the received signals so as to know the direction of the transmitted signals. These transducers are smaller in size, which proves advantages because

there is no need for moving parts, and they are capable of producing an electronically focused beam. Often, manufacturers of these transducers assume the speed-of-sound to be 1540 m.s^{-1}, which is in fact the average speed-of-sound in human tissue.

Two-dimensional ultrasound is extensively used in routine ultrasound imaging where users are able to manipulate the ultrasound transducer freely over the region of interest in the body to generate necessary images. Although this imaging technique is popular in many interventional procedures, 3D image visualization may prove more useful in some of the interventions. Physicians often image the anatomy of the interest by acquiring many 2D ultrasound images (moving the ultrasound probe manually over the anatomy of interest) and mentally integrating images to get the impression of the anatomy in a 3D context. This process can be time consuming and may result in inconsistent guidance during the intervention. The advancement of ultrasound technology has enabled conventional 2D B-mode imaging to be enhanced by 3D or volumetric imaging that is also called 4D imaging, where dynamic 3D rays are acquired. There are three main methods for acquiring the three-dimensional images.

1.0.4   Mechanical 3D Ultrasound

Mechanical 3D ultrasound is based on the mechanical motorized mechanism that translates, tilts, or rotates a linear/curvilinear array transducer over the object of interest [8, 25]. Therefore a series of 2D ultrasound images that can be reconstructed into a 3D volume are produced. In this type of 3D ultrasound imaging, the scanning geometry is predefined and known by the mechanical system. Implementation of mechanical 3D ultrasound is straight-forward but slow, and if it is used for imaging dynamic structures, such as a beating heart, it would require extensive cardiac gating.

1.0.5   Free-Hand 3D Ultrasound

Free-hand scanning is another common method for 3D ultrasound imaging [32]. In this approach, the user manually translates or rotates the linear or curvilinear array over the object

of interest. To reconstruct 3D ultrasound volume based on the 2D images, position and orientation of the ultrasound transducer are tracked during the free-hand scanning process. Often the motion of the transducer is measured by an external magnetic/optical tracking system or a robotic system that is synchronized with the 2D image acquisition.

Free-hand 3D ultrasound is most successful in interventional procedures such as echocardiography with the use of magnetic sensors [6, 41]. In these procedures, a small receiver is mounted on the transducer with the purpose of sensing its 6 degrees-of-freedom (DOF). So the position and orientation of the transducer are determined continuously. The main advantage of a free-hand 3D ultrasound is the ability to scan an arbitrarily large volume. It is often more applicable when scanning the anatomy of interest with a single sweep which is impossible due to the limited FOV. Then, the transducer can be moved over the object from different angles and with separate free-hand sweeps to create a surface model and estimate the volume. However, the quality of the free-hand 3D ultrasound is dependent on the ability of the user to sweep the transducer in a regular smooth pattern, so that the 3D volume is uniformly filled with constituent 2D images.

1.0.6 Real-Time 3D Ultrasound

Real-time 3D ultrasound, using a 2D matrix array, is one of the most technologically advanced methods for 3D imaging. The 2D array transducer consists of square elements that allow beam-steering in both the azimuth and elevation angles. The result is a 3D pyramidal sector shape volume. Another approach is to construct a 2D array of slightly larger elements and acquire images in a similar way as the conventional linear array systems [19]. The 2D sub-aperture of active elements is focused straight ahead to form the 3D rectilinear volume.

One of the first 2D array techniques was developed at Duke University. Their system employed parallel beam-forming to produce real-time volumetric acquisitions [77]. The system had a 256 channel beam-former for both transmission and reception, with the ability to acquire 30 volumes/second. Today, with the advancement of this technology, dense probes with 2500

elements are able to acquire 20-25 volumes/second using the parallel processing technique.

1.0.7   3D Ultrasound in Cardiac Imaging

1.0.7.1   Transthoracic Echocardiography Imaging

One of the main areas where ultrasound imaging has been highly applicable is in cardiac procedures. Transthoracic echocardiography (TTE) is a technique that is used to monitor the anatomy and dynamic behavior of the heart. In this procedure, a TTE probe is placed on the chest of the patient to acquire images of the heart. To produce 3D images, either the free-hand 3D technique or matrix-array transducer can be used. TTE imaging is typically used to determine the size and function of the heart valves, with the disadvantage that there is limited space between the ribs for placing the probe [67, 26]. In obese patients or those with chronic lung disease, the penetration depth is often an issue due to the thickness of the layers, which results in poor imaging. Another limitation of TTE imaging is the inability to acquire posterior cardiac structures such as the pulmonary vein, left atrium, and mitral valve, and interference by the respiratory cycle. Also, this imaging technique is not suitable for intra-operative cardiac procedures since the probe has to stay in contact with the patient's chest continuously.

1.0.7.2   Trans-esophageal Echocardiography Imaging

Transesophageal echocardiography (TEE) probes are designed to be placed inside the esophagus, in the interior of the thorax [78, 30]. The TEE probe allows for imaging the heart from a closer proximity with less interaction with the tissues outside the region of interest and less obstruction from fatty tissues. In recent years, TEE has been extensively used for rapid, real-time cardiac assessment [56]. TEE provides a direct 'window' into the heart, facilitating the prompt evaluation of both cardiac function and left ventricular volume status. Continued monitoring of left ventricular function during cardiac surgery was described in 1980 [58]. Also, TEE is an appropriate indicator for evaluating regional ventricular wall motion [44, 54, 79]. Other investi-

gations using TEE imaging showed the association between the cardiac chamber size, preload, volume status, and cardiac output in the ICU for patients with cardiac illnesses [82, 67, 37, 80].

In the past, TEE probes were operated by remote and mechanical rotation of the transducer using a manual knob. This included mechanical movement of the ultrasound transducer either linearly or annularly. There were problems associated with this technique, such as size, motion artifact, and extensive mechanical equipment which required many cardiac cycles. Later on, the 3D rotational reconstruction was developed via an omni-plane TEE probe which has multiple arrays rotating in either 3 or 5 degree increments. ECG timing permits assembly of these datasets to form a 3D rotational reconstruction of the heart [45].

The most recent TEE probes are designed on the matrix-array technology. The 3D TEE matrix transducer (X7-2t, Philips, inc) is one example that is commonly used in day-to-day clinical procedures. This probe has the ability to provide standard 2D images, in addition to the Doppler mode. Also, it is able to image in bi-Plane mode, where two distinct 2D image planes are acquired simultaneously and are separated by a known angle. Live 3D is another mode which has a pyramid wedge shape of approximately $50° \times 30°$ angles, which makes the visualization of any cardiac anatomy in the near field possible [87].

1.1 Image Guided Cardiac Surgery

Image guided surgery (IGS) systems have revolutionized the traditional surgery. Advanced computing and imaging technologies are used to guide and help surgeons whenever direct vision of the surgical target is inadequate or unavailable. IGS was first introduced in neuro-surgery, in which a stereotactic frame was rigidly attached and fixed to the patients' head [68]. In this approach, a surgical tool could be guided precisely across a known coordinate frame, using mechanical guides.

According to [68] the definition of IGS is:

Image-guided procedure is a minimally invasive procedure performed using imaging for guidance. Example image-guided procedures include angioplasty, needle biopsy, vertebroplasty, [and stereotactic neurosurgery]. An image-guided system, as noted above, includes a three-dimensional localizer, a registration method, and an image-overlay display. Image-guided systems are sold by several vendors and sometimes called navigation systems.

Computer-Assisted Surgery (CAS) is an advancement of IGS, being described as:

computer-aided surgery in its broadest sense is the use of computers to aid in medical procedures. More specifically, it connotes the use of computers to plan, execute, or evaluate surgical procedures.

Minimally invasive approaches have been applied in a wide range of cardiac procedures such as: mitral valve repair and replacement, aortic valve replacement and repair [84, 81, 89], coronary artery bypass grafting (CABG) [88], ablation to electrically isolate the pulmonary veins (PVs) and/or targets for treatment of the atrial fibrillation (AF) [75] and repair of congenital pathologies such as atrial septal defects (ASDFs), ventricular septal defects (VSDs) or patent foramen ovale (PFO) [20]. In the minimally invasive procedures the main goals are: reduction of trauma, improvement of the survival rate, decreased risk of infection, decreased bleeding, reduction of postoperative pain and shorter recovery times.

1.1.1   IGS in Mitral Valve Repair Surgery

Traditional cardiac surgery, began in early 1953 [15] where surgeons employed cardiopulmonary bypass (i.e. heart-lung machine takes over the functionality of the heart and the lungs during surgery) to facilitate the procedure. Median sternotomy and temporary cardiac arrest were essentials for these procedures, resulting in longer recovery periods which are often not appropriate for elderly patients and in those with multiple co-morbidities [2].

Among all cardiovascular diseases, mitral valve (MV) insufficiency, is the second most common heart valve disease, occurring in about 2% of the general population [31]. Degenerative mitral valve disease (DMVD) is an example where the valve ruptures or a prolapsing valve leaflet results in an incomplete MV closure. The advancement in MV repair techniques dramatically changed the conventional procedure and improved the short/long term outcome of the patients [38].

Minimally invasive techniques were developed to replace the conventional median sternotomy. Firstly, minimal invasive MV surgeries were performed through parasternal and hemisternotomy approaches in 1990s [65]. The second achievement was video-assisted MV repair through minithoractomy in 1996 [10]. Currently, the most popular approach is through a minithoracotomy even though it still requires cardiopulmonary bypass [14]. The main issue in the on-pump surgery is the inability to assess the success of the MV repair in the moment, during procedure, since the heart is arrested. Alternative techniques have been introduced to fill the left ventricle (LV) and inspect the MV in an arrested condition. nonetheless these post-assessment procedures are not accurate because they evaluate the function of the valves in non-physiological conditions. Currently, the best technique to assess the post-repair mitral valve competence is by using TEE imaging on the beating heart, after separation from cardiopulmonary bypass. TEE provides excellent 2D and bi-plane evaluation of the repair of the MV. However, while TEE interpretation of the repair is relatively standardized, there is always a level of uncertainty around the true physiological consequences [76]. So if the repair is considered to be unsuccessful, then cardiopulmonary bypass must be re-established and the heart must be arrested.

To overcome this limitation, off-pump techniques have been developed in which the patient's heart remains beating and blood flows naturally through the valves [76, 71]. The off-pump process provides real-time and direct-view of the MV during surgery. Currently there are several techniques available for minimal invasive off-pump MV repair, two of which are discussed below.
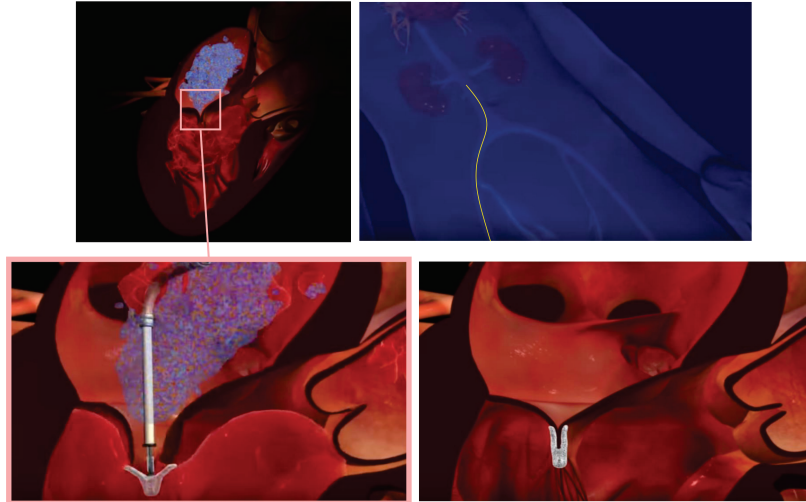
Figure 1.4: Minimally invasive off-pump MV repair based on MitraClip device.
†Adapted from MitraClip(www.MitralClip.com)

Percutaneous Edge-to-Edge Leaflet Clipping (MitraClip©) (Fig.1.4) is a system designed to perform edge-to-edge clipping by creating a double orifice valve [24]. In this system an implant catheter is inserted through the femoral vein and into the left atrium. The clip attached at the tip of the catheter, is cautiously positioned at the closest distance to both the leaflets so that it can grasp and clip the two leaflets together. A double orifice valve allows a greater valve closure and less regurgitation. The interventionist in this system has the ability to release the clip and re-grasp the leaflets repeatedly and can determine and adjust the grasping position using Doppler echocardiography.

Transapical beating-heart MV repair is another approach where a device called NeoChord DS1000 (Fig.1.5) can perform off-pump MV repair [16]. The NeoChord device enters the chest through a 5cm incision between the ribs and is then inserted through a hole at the apex of the heart, allowing access to the left ventricle. This device carries a grasping mechanism to catch the respective prolapsing leaflet segment and has the ability to confirm successful grasping by using fiber-optic technology. In addition, it has a semi dull needle to puncture the leaflet and secure the nechord to the leaflet and retract the neochord extracardially. The process of suturing with the needle may be performed multiple times to limit the movement of the leaflets during systole.
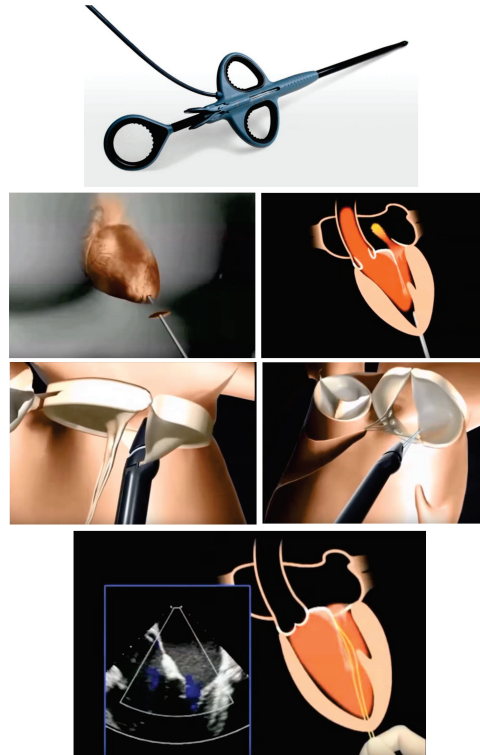
Figure 1.5: Minimally invasive off-pump MV repair based on NeoChord DS1000 device.
†Adapted from NeoChord (www.NeoChord.com)

Since the transapical MV repair is performed in an off-pump environment, TEE ultrasound imaging was used for real-time guidance of the tool to the target area. TEE imaging is not limited to the trasapical MV repair approach but is widely used in most off-pump mitral and aortic valve procedures [23]. In the NeoChord implantation, the successful repair depends on precise localization of the regurgitation site and this requires effective intraoperative communication between the echocardiographer and the surgeon. Both 2D and 3D TEE imaging are essential tools for the surgeon's guidance throughout all phases of this procedure. The 3D TEE allows the possibility of seeing the valvular anatomy and the NeoChord device in one context and is used for the positioning task. In contrast, 2D bi-plane TEE is mostly preferred for assessing the MV anatomy and for guiding the device from apex of the left ventricle across the mitral annulus. The TEE view is changed from 2D biplane to 3D once the MV has been crossed (See Fig.1.6). 3D TEE provides the optimal orientation of the tip of the device with respect to the prolapsing segment of the leaflet.
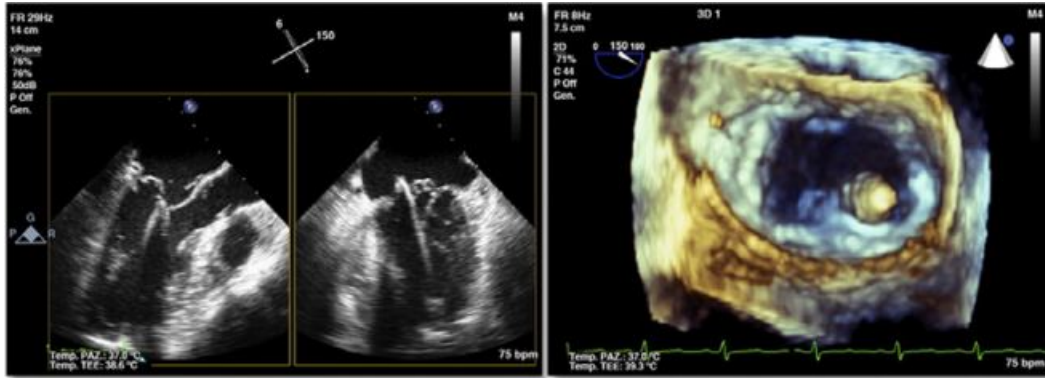
Figure 1.6: TEE bi-plane and 3D ultrasound imaging of the NeoChord tool while it has been placed inside the heart. [†]Aadopted from [16].

1.2 Tracked Ultrasound in IGS

Characteristics of ultrasound imaging makes it a valuable intra-operative tool for surgical guidance procedures. However, navigating the surgical tool only based on ultrasound imaging is considered to be a challenging task, which the tracked ultrasound has improved and simplified it. Tracking the spatial location of the ultrasound transducer and the surgical tool allows us to know the pose of the ultrasound image and the surgical tool in a common 3D context so as to further assist a surgeon in a navigation task.

1.2.1 Types of Tracking

Tracking the ultrasound probe is often done by an optical marker, a magnetic tracking sensor, or a robot end-effector. Optical tracking systems (Fig.1.7) are able to track multiple devices simultaneously with high accuracy, covering a larger work space. One of the main challenges with this system is the necessity for line-of-sight, requiring a marker or a pattern to be attached to the devices so that the camera can track them. That said, the main limitation is that the markers need to be clean and clear enough to be accurately tracked by a camera. In addition it is not a suitable tracking system for a TEE probe that is inserted into the esophagus of the patient. On the other hand, robot end-effector is also not an appropriate tracking tool for intra-operative image-guided procedures using TEE imaging.
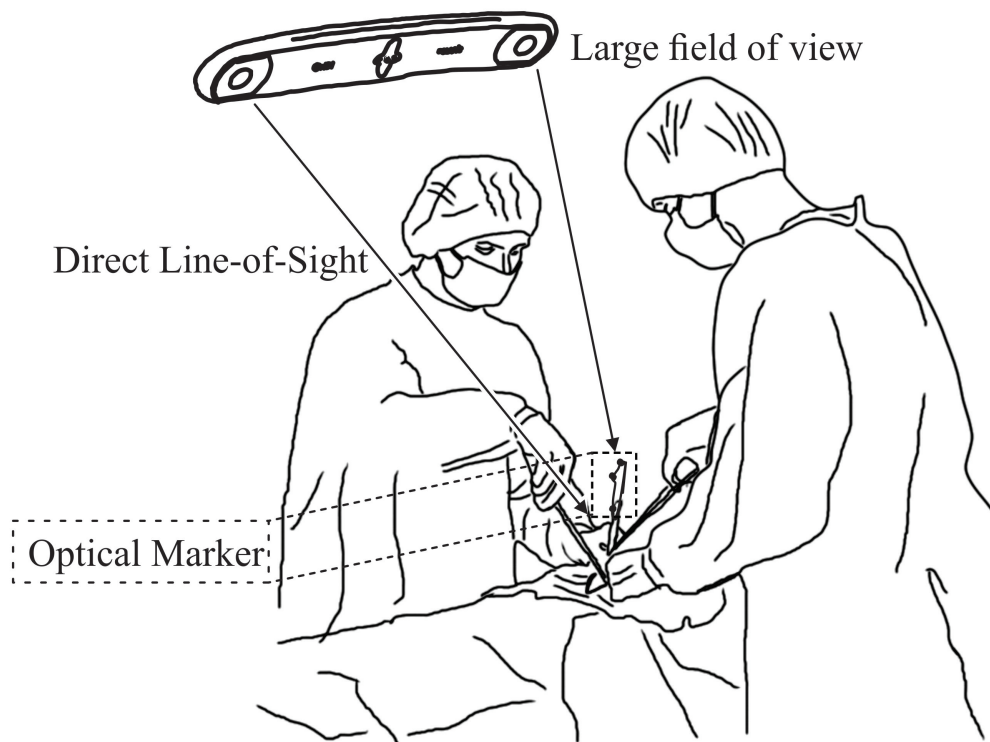
Figure 1.7: Optical tracking

Magnetic tracking system (MTS)[1] is an alternative approach with no line-of-sight related issue. In this approach small sensors are localized within a magnetic field of known geometry that is created by a field generator (FG) (See Fig.1.8). Attaching a sensor to flexible instruments such as TEE probes, catheters, or flexible endoscopes allows for the real-time tracking of these devices. Magnetic based tracking has been applied to various surgical interventions, such as deployment of stent grafts [1], catheter-based ablation therapies for treatment of the arterial fibrillation [92], navigated bronchoscopies [35], radiofrequency ablation of liver tumors, guidance of flexible laproscopic ultrasound probes [3], and tracking the TEE probe in minimally invasive cardiac procedures [61]. However the most critical problem with magnetic tracking systems is the impact of metallic objects on the surgical environment.

---

[1]The magnetic tracking system in literature is often referred to as an electromagnetic tracking system. However, since electric signal is not directly involved in the actual tracking process, the more appropriate terminology of 'magnetic tracking system' preferably is used throughout this thesis.
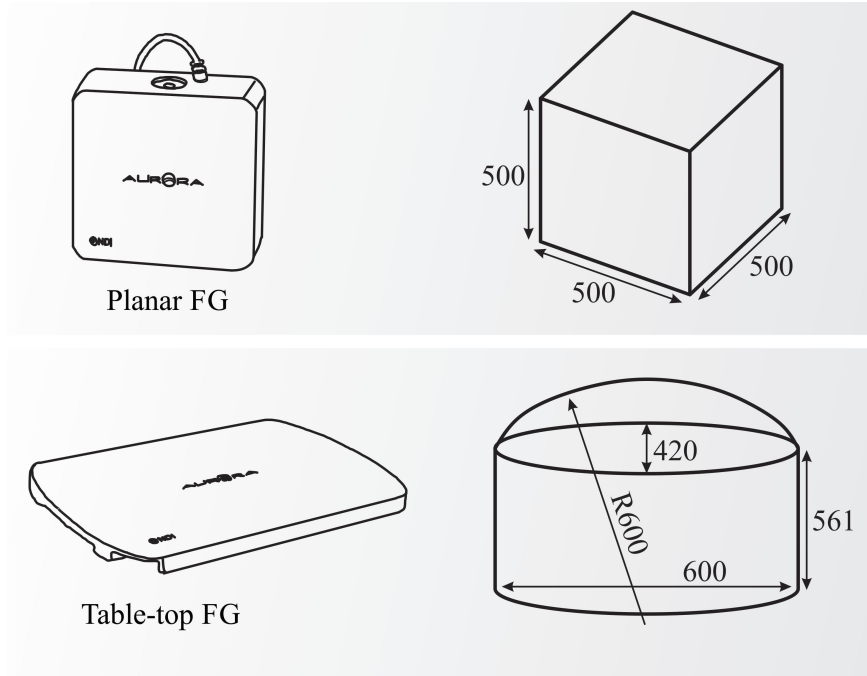
Figure 1.8: Magnetic tracking system's FG. The corresponding magnetic field generated by Aurora Planar and table-top FG are presented in the top right figure. All of the measurements are given in millimetre. Table-top magnetic tracking FG (NDI Waterloo, Canada) was used throughout this thesis. †Adapted from NDI.

1.2.2   Ultrasound Calibration

Ultrasound calibration has been an active research area for the last 20 years [42]. It maps the coordinate system of the ultrasound image to that of the tracking system (See Fig.1.9). The coordinate system of the FG, due to its stationary position, often serves as a world coordinate[2], and most of the computations are obtained at this coordinate. The calibration transform consists of scaling parameters followed by rotation and translation. There are three rotations of azimuth, elevation and roll; three translations in the x-, y- and z- axes direction; two scale factors in the x- and y- axes (in 2D ultrasound); or three scale factors in the x-, y- and z- axes (in bi-plane or 3D ultrasound).

---

[2]The coordinate system of the table-top FG is referred to as a world coordinate throughout this thesis.
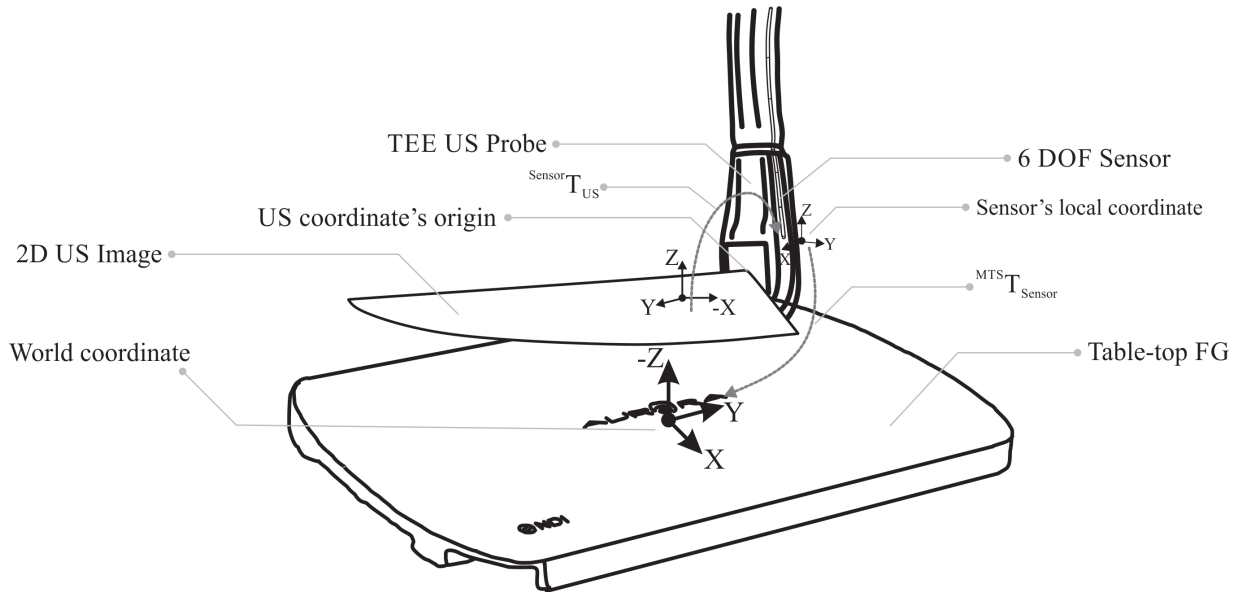
Figure 1.9: A tracked TEE ultrasound probe within a magnetic field. The figure above demonstrates the transformation ($^{\text{Sensor}}T_{\text{US}}$) (i.e. US calibration) that maps the ultrasound image to the sensor coordinate (i.e. attached at the tip of the probe). In addition, ultrasound information can be sent to the world coordinate by applying the transformation between the position sensor at the probe to the MTS.

1.2.2.1 Registration in Ultrasound Calibration

Mapping two sets of data from one coordinate system to another is accomplished by a transformation that is generally called registration. Paired-Point registration is a common approach where the correspondence of each point is known within the other coordinate system. Also, in order to achieve an unique solution, three or more non-collinear points are required. Registration in ultrasound calibration context can be categorized into rigid and similarity modes. Similarity mode can be nailed down into isotropic and anisotropic scales. The complexity of registration is defined by the number of parameters to be solved (i.e. DOF) (See Fig.1.10).

Among all registrations, rigid has the fewest DOF because the same geometry is being transferred as a result of rotation and translation. This is achieved while scale parameters of the pixel/voxel are known a priori. The (R) and (t) matrices consist of three parameters each and are applied to a point (x) as demonstrated in Eq.1.5. The rotation and translation parameters are combined together and form a 4×4 matrix which is known as a homogeneous transform Eq.1.6.
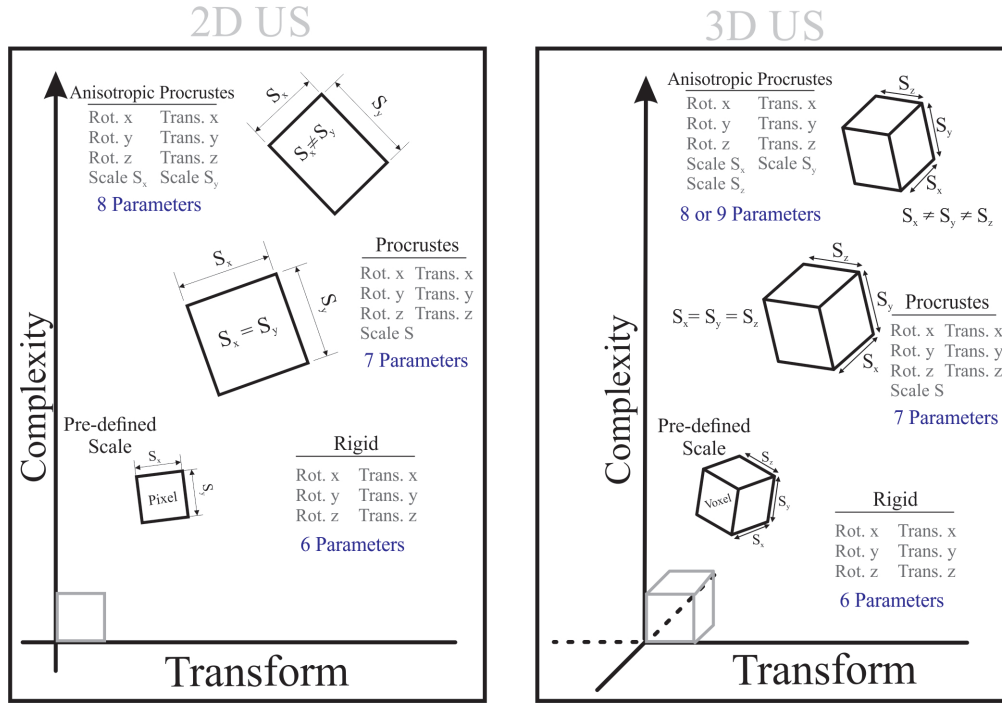
Figure 1.10: Complexity of calibration transform depending on the type of registration. The above demo illustrates an increase in degrees of freedom for both 2D and 3D ultrasound calibration.

In similarity mode registration with isotropic scale, a uniform scale is added to the rotation and translation parameters (1.7). It occurs when pixel/voxel has a uniform scale in each direction (1.8). In contrast, anisotropic S_x includes either two or three different scale parameters each corresponding to x-, y- and z- directions.

$$T = Rx + t \tag{1.5}$$

$$T_{4\times4} = \begin{pmatrix} R_{3\times3} & t_{3\times1} \\ 0_{1\times3} & 1 \end{pmatrix} \tag{1.6}$$

$$T = RSx + t \tag{1.7}$$

$$S = \begin{pmatrix} S_x & 0 & 0 \\ 0 & S_y & 0 \\ 0 & 0 & S_z \end{pmatrix} \tag{1.8}$$

1.2.2.2 Fiducial Registration Error

Fiducial refers to a point used in the registration process. Aligning two sets of fiducials can be obtained through, first, computing the average or centroid of the fiducials in each set, and then followed by the distance between the computed centroids which implies the translation. The fiducials are rotated about the new centroid, until the sum of squared distance between each corresponding paired-point is minimized [39]. The root mean square (RMS) distance between the two point sets is reported as the goodness of alignment. The RMS error, or residual error, or fiducial registration error (FRE) are terminologies commonly used for reporting the quality of registration. FRE in ultrasound calibration is measured as:

$$\text{FRE} = \sqrt{\frac{1}{N} \sum_{i=1}^{N} |\text{T}(p_i) - q_i|^2}, \tag{1.9}$$

Where N is the number of fiducials, p_i and q_i are positions of the (i^{th}) fiducial in ultrasound and tracking coordinate, respectively. Note that, FRE only represents the goodness of fit between data sets and is not a proper metric for goodness of the calibration transform [27]. Reporting FRE may be associated with issues such as overestimation or underestimation [28]. In the underestimation process, FRE will not reflect some components of registration error since locations of the same fiducials are used to determine the registration transform. In this situation, the system does its best within the limits of transformations to align fiducials regardless of whether they truly correspond. For instance, when a consistent error occurs in one direction for all the fiducials of the first set, the error reflects as an additional value to the translation in the registration transform. On the other hand, in the overestimation scenario, random errors may occur in localizing of the fiducials, that are uncorrelated, in a dataset. Therefore, upon applying the registration transform to the same dataset, errors associated with some fiducials tend to be canceled out through the influence of others.

1.2.2.3   Target Registration Error

The target should be an information different than the fiducials used in the registration pro-cess. The appropriate way to determine the registration error is through knowledge of the position/feature of a target in one coordinate and transferring the correspondence through the registration transform into a common coordinate so as to measure the goodness of their align-ment. In ultrasound calibration, targets can be anatomical landmarks, the tip of a tracked pointer or features of a phantom. Indeed, changes of the target registration error (TRE) over the FOV of an ultrasound image is the most important metric for determining the quality of registration [27].

1.2.2.4   Localization in Ultrasound Calibration

In ultrasound calibration, identifying the true location of an object in the ultrasound image/volume is referred to as localization. Fiducial localization error (FLE) and target localization error (TLE) are the two terminologies[3] for reporting the error in locating the fiducial and the target point in ultrasound images [90]. Specifically, FLE could be the reason for inaccurate calibra-tion whereas TLE leads to inaccuracy in reporting the goodness of calibration result.

Factors causing localization error are: ultrasound beam-thickness, material properties of an object, resolution of an ultrasound image, image processing (e.g. segmentation) and user experience. The beam-thickness is an issue which varies among different transducers; from a few millimeters up to one centimeter along the elevation direction. Nevertheless, as the fidu-cial/target moves further away from the focal point, its reflection in ultrasound does not truly correspond to its intersection with the scan plane. Issues regarding the beam profile have been addressed more specifically in [13, 36]. The appearance of an object in an ultrasound image can be greatly influenced by the material properties of a scanned object. In an ideal situa-

---

[3]information regarding TRE, FRE, TLE, FLE and as a whole the theory of errors have been advanced in the medical application domain through the work of the Fitzpatrick research group [29]. Additionally, detailed information about navigation accuracy for IGS procedures has been well explained in A. D. Wiles' research work [91].

tion, a pixel/voxel should determine a fiducial/target in the ultrasound image. But due to the properties of material (e.g. high scattering), a cloud of pixels/voxels reflect the corresponding object. Therefore, segmenting the ideal pixel/voxel among a cloud of pixels/voxels could be a challenging task (novice users tend to perform poorly).

1.2.2.5 2D Ultrasound in Calibration

Two-dimensional ultrasound imaging of a known geometrical, precisely manufactured, phantom is the basis for many calibration techniques that have been developed. Prior knowledge of the characteristics of a phantom and representation of the corresponding features in an ultrasound image allows to solve for the unknown calibration parameters. A Point phantom is one of the very first and most common methods for 2D ultrasound calibration, where a known point within physical space is used [21, 85]. Either the tip of a tracked pointer or the crossing point of a pair of wires can be used as the specified point. In a cross-wire phantom [21], stationary positioning of the phantom in the world coordinate is essential while ultrasound scanning is in process. The three-wire phantom is another wire-based approach designed to solve for the calibration transform [11, 70]. In this technique, three wires are positioned mutually orthogonal to form the three axes of the phantom's local coordinate. Scanning each wire along its length and corresponding the same axes in the image coordinate with the tracking coordinate allows to solve for the unknown parameters. The advantage of the three-wire method over the cross-wire was the easier scanning of the length of a wire in comparison to localizing a point at the intersection of wires. However, each wire needs to be individually scanned and the user must carefully track the image to identify which wire is being intersected with the ultrasound plane throughout the scanning process. Also, straightness of the wires and precise orthogonality among them are key points that affect the accuracy of the calibration.

Scanning a planar-surface is another popular calibration paradigm [63, 70, 93]. In this method a planar-surface, which can be the floor of a water bath, is scanned from a sufficient # of poses. The planar-surface corresponds to the xy-plane of its local coordinate system. Its
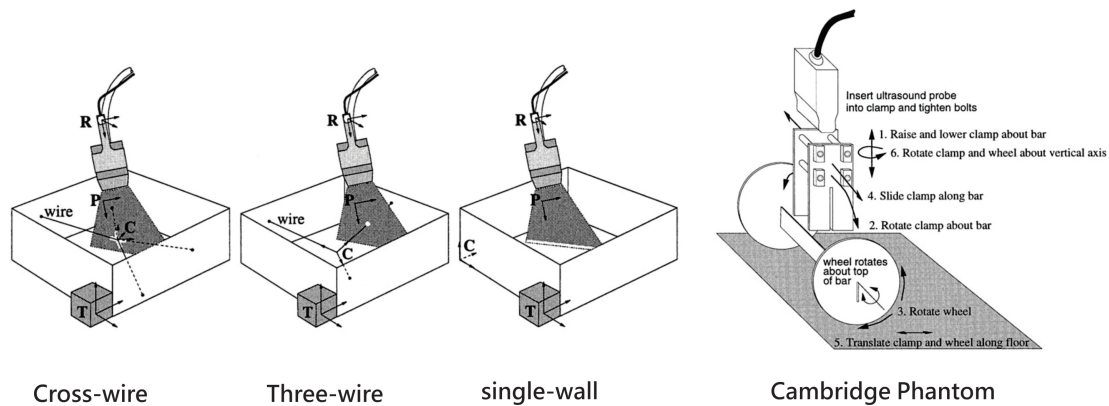
Figure 1.11: Schematic diagram of cross-wire, three-wire, single-wall/planar-surface and Cambridge methods. [†]Adapted from [70].

ultrasound reflection appears as a line in each B-mode scan. Thus, it is possible to relate the ultrasound reflections of a plane to the xy-plane of the planar-surface.

$$
\begin{pmatrix} x \\ y \\ 0 \\ 1 \end{pmatrix} = {}^{C}\mathbf{T}_T \, {}^{T}\mathbf{T}_R \, {}^{R}\mathbf{T}_P \begin{pmatrix} s_x u \\ s_y v \\ 0 \\ 1 \end{pmatrix} \tag{1.10}
$$

Where C is defined to be as the floor with the orthogonal z-axis. Any point (u, v) on the line in the ultrasound image should correspond to the xy-plane. While the advantage of this technique over the other methods is that no extra device is required, the accuracy of the calibration depends on the flatness and stationarity of the surface. One limitation of this technique is the large number of ultrasound acquisitions required for solving the unknown parameters. Also, when the beam is not normal to the planar-surface, echoes returning to the transducer come from the beam edge that is closest to the plane. Due to this effect, scanning a plane from oblique angles causes the returning intensity to be lower and introduces the positioning error in identifying the reflection of a plane in B-mode images. Angular scanning of a plane is necessary to solve for the calibration, and therefore, the aforementioned issue has been addressed by designing the Cambridge phantom [70]. The phantom consisted of a clamp that fits around the probe and a thin bar mounted between the two circular disks. The clamp constraints the thin bar to move only in the center of the ultrasound beam. The bar is attached to the disks such that as disks are
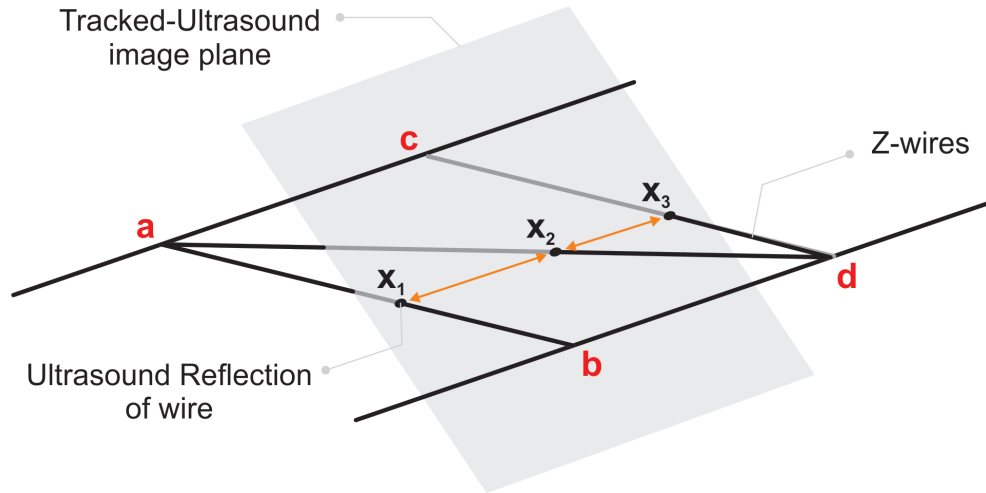
Figure 1.12: The concept of Z-bar phantom.

rolled, the upper edge of the bar stays at a constant height above the floor. Therefore, the top of the bar is assumed as a virtual-plane, and at every angle the bar is always oriented towards the ultrasound probe so that the resulted strong reflected beams produce clear reflections of a plane. Nevertheless, the phantom has its own drawbacks; it requires a precise manufacturing process and a custom-made clamp for each specific probe. As a result, it is costly and unavailable.

Z-bar is yet another wire-based method that is among the most easy-to-use and common approaches [42]. The concept of this technique was initially described in the context of constructing a stereotactic head-frame to use with computed tomographic (CT) scans in neurosurgery [9]. Later on it was introduced into ultrasound calibration by Comeau *et al.* [17] in 1998. In the Z-bar phantom, the ends of wires are precisely known within the body of a phantom either by a tracked stylus or pre-defined while manufacturing (See Fig.1.12). A position sensor is then attached to the phantom to track the position of wires in a tracking coordinate system. When the tracked-ultrasound scans the wires, three bright dots appear on ultrasound image that correspond to the respective wires; namely x_1, x_2, and x_3. Then, based on distances between specified points, $D_{12} = \| x_1 - x_2 \|$ and $D_{13} = \| x_1 - x_3 \|$, a ratio α can be achieved where a similar result is established through the triangles in the Z pattern.

$$\alpha = \frac{D_{12}}{D_{13}} = \frac{\| a - x_2 \|}{\| a - d \|}, \tag{1.11}$$

where $\| \cdot \|$ denotes the $\| \cdot \|$ distance between the two points. Also, a and d are the two tails of middle wire in tracking coordinate system. In which, based on α the position of x_2 is derived through the following equation:

$$^{T}X_2 =^{T} a + \alpha.(^{T}d -^{T} a) \tag{1.12}$$

$^{T}X_2$ represents the intersection of the ultrasound plane with the second wire of the Z pattern in the tracking coordinate system which is directly obtained from the ultrasound image of the phantom. To solve for an accurate calibration result, more images of the phantom are required. If three Z-bar phantoms are arranged to be scanned in a single frame, then there is sufficient information to solve for the unknown parameters. The Z-bar phantom is relatively easy to manufacture, and the user's experience has the least effect on the accuracy of the calibration. Nevertheless, the accuracy of this phantom has shown poorer result, compared to the Cambridge phantom [42]. The reviews of the aforementioned methods and other techniques have been detailed in [42].

1.2.2.5.1 Point-based Calibration   In 2001, Muratore *et al.* [62] proposed a method that did not require a custom-made phantom; instead the tip of a tracked pointer was used as a ground truth. The ultrasound reflection of the pointer's tip and its three-dimensional position in the tracking system were used to compute the calibration parameters. The main challenge with this technique is aligning the ultrasound plane with the exact tip location of the pointer, where often the experienced users tend to perform better than novice users.

1.2.2.5.2 Line-based Calibration   Khamene and Sauer [46] extended the aforementioned method to the 'phantomless' calibration. In their approach the limitation of localizing the tool tip in an ultrasound image was addressed by determining two or more points along the length of a calibration pointer so that the orientation of the tool is known. As a result instead of imaging the tip, anywhere along the length of the tool can be scanned and the calibration parameters

can be solved through the following formulation.

$$^{W}T_{S1}\,(P_{p_0} + \lambda\,\frac{P_{p_1} - P_{p_0}}{|P_{p_1} - P_{p_0}|}) = \,^{W}T_{S_0}T_cT_sP_u, \tag{1.13}$$

where λ is a real number within [0-1]; P_u is the ultrasound reflection of the intersecting tool with ultrasound plane; T_s and T_c are transformations of scale followed by rotation and translation parameters, $^{W}T_{S_0}$ is the $^{b}T_a$ of the probe-sensor to the world coordinate and $^{W}T_{S_1}$ is a specific tracked point in the tool. Also, P_{p_0} and P_{p_1} denote the two points along the length of the tracked tool in tracking coordinate system. In order to disregard the unknown factor of λ, the above equation can be rewritten as:

$$[L_{01}]_x[^{W}T_{S_0}T_cT_sP_u -^{W} T_{s1}P_{p_0}]_3 = 0_{3\times1}, \tag{1.14}$$

where $[.]_x$ converts a vector to a skew symmetric matrix, and $0_{3\times1}$ represents a null point. In the above equation L_{01} is the normalized vector within the world coordinate system, where two points P_{p_0} and P_{p_1} lie along the vector L_{01}.

$$L_{01} = \frac{^{W}R_{S_1}[P_{p_1}] -^{W} R_{S_1}[P_{p_0}]_3}{\|[P_{p_1} - P_{p_0}]_3\|} \tag{1.15}$$

$^{W}R_{S_1}$ is the 3×3 rotation matrix embedded in $^{W}T_{S_1}$. To achieve the optimal calibration, scanning the tool from various orientations is essential. An optimization method is developed to relax the constraint of the exact intersection of the pointer with the ultrasound plane. This technique minimizes the user dependency during data acquisition. However, one limitation is the requirement of a good initialization for the optimization process. Secondly, proper segmentation and identification of a point that refers to the specified tracked line is another key requirement that can affect the end result.

1.2.2.6   3D Ultrasound in Calibration

Conceptually, 3D ultrasound calibration is similar to the 2D calibration with the difference on mapping the 3D volume instead of the 2D image to the tracking coordinate system (See Fig.1.13). In reconstructed 3D ultrasound, where volume is created based on the mechanical sweeping or freehand movement of the 2D probe, calibrating the 2D image to the tracking system is equivalent to the calibration of 3D ultrasound. However, when dealing with real-time 3D ultrasound, volumetric representation of an object is the only source of information from ultrasound coordinate that relates the ultrasound to the tracking system. One advantage of the 3D volume over the 2D cross-sectional data in the calibration process could be the larger field of view for detecting the special features of a phantom leading to fewer rounds of data acquisition for computing the calibration parameters. The main drawback of 3D probes is their lower spatial resolution which impacts localization of an object, a source of error in calibration.

To date, few publications have addressed 3D calibration based on 3D ultrasound volume imaging. Lange *et al.* [62], employed a phantom with two egg-shaped objects that require registering geometrical model from the 3D ultrasound volume to the ground truth (CT volume). The other well-known method was 'hand-eye' calibration [49], where the idea is to register two or more ultrasound volumes from the same phantom, acquired from different directions, to form a registration loop. Each volume recorded by the tracking system had a different position, and therefore registering them established a fixed relationship between the tracking and ultrasound coordinate.

Wire-based techniques were also used for 3D ultrasound calibration, in particular Z-wire [7]. A phantom with 39 wires, in the form of Z patterns, was designed such that 13 Z-shape wires repeated over 13 different depths, and their position was exactly known within the phantom box. The position of the phantom was being tracked by position sensors, attached to the phantom box. After scanning the phantom, the shape and position of the wires appears in the ultrasound coordinate. Since the wire positions were known in the tracking system, calibrating the ultrasound volume to the tracking system was achieved through a line-to-line registration.
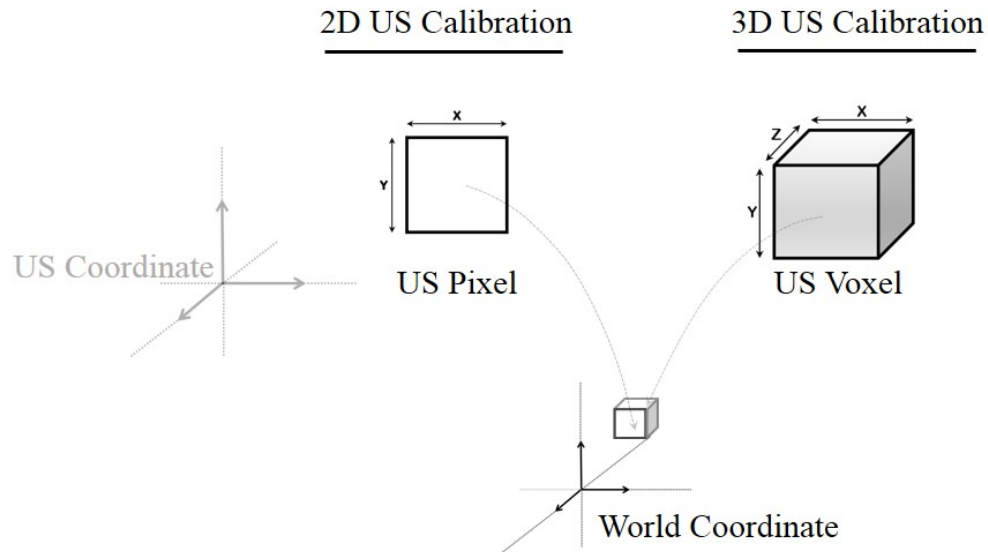
Figure 1.13: 2D vs 3D ultrasound calibration by mapping a pixel vs a voxel to the respective position in world coordinate.

Poon and Rohling [69] compared three other methods for 3D ultrasound calibration, namely the IXI phantom, the cube phantom, and the stylus-based approach. The IXI phantom was similar to the wire-based methods, and the cube phantom was similar to plane-based methods in 2D ultrasound calibration. In most of the approaches the biggest challenge was identifying the phantoms' features in the ultrasound volume due to the poor resolution. Moreover, precisely manufactured phantoms have demonstrated superior calibration results than the 'hand-eye' method. It has been suggested that 'hand-eye' calibration can only be used when tracking of the phantom is not possible [4]. The point- and line-based methods were also compared side-by-side for calibrating real-time 3D ultrasound [48]. Segmentation of the needle's tip served as a fiducial in the point-based approach, and any segmented voxel representing the length of the needle was used for the line-based approach. Due to reflection artifact in 3D ultrasound, localization of the tool tip, or anywhere along its length, was inaccurate, resulting in lower accuracy in 3D calibration.

Recently, a plane-based method was proposed to calibrate real-time 3D ultrasound [12]. The phantom consisted of 5 non-parallel planes, arranged in the form of 4 non-parallel and asymmetric planes connecting to the horizontal floor. The three adjacent planes appear as a

point in 3D ultrasound, resulting in six intersection landmarks serving as fiducials. A reference sensor is attached to the phantom so that the position of the phantom is known in a world coordinate, and a CT of the phantom serves as a ground truth. Therefore, the relationship between the fiducials and their tracked positions were solved by computing the anisotropic scale, rotation, and translation parameters.

1.2.3 Validation of Calibration

Assessment of the quality of calibration result is as important and challenging as the calibration procedure itself. The reliability of a calibration technique is tied to the proper validation methods. Unfortunately, to date a consensus has not been as to a standard approach for evaluating the quality of ultrasound calibration [42]. In addition, every research group, depending on the availability of tools and convenience, quantifies the calibration results differently.

1.2.3.1 Accuracy in Calibration

The overall accuracy of ultrasound calibration is defined based on its trueness and precision[4]. To validate the estimated transform, a target point can be scanned by the calibrated probe from different orientations and depths in an ultrasound image. Target points are transferred to a common coordinate by passing through the calibration transform. The result, is a cloud of points where the mean represents the trueness, and the standard deviation (SD) reflects the precision of the system. In the literature, a spread of points is referred to as reconstruction precision (RP) [21, 70, 43, 62, 64], in which this metric cannot be independently considered a proper quantification for the calibration's quality. On the other hand, the SD, besides representing the calibration error, may include the tracking, segmentation and alignment errors as well. Lower SD (smaller spread of points), suggests that the system is precise and stable, even

---

[4]Note that, the terminology of accuracy is referred to as the combination of trueness and precision (defined in the international standard ISO-5725-1:1994(E)). These correct terminologies are preferred for use in this thesis rather than the traditional definition of accuracy and precision often provided in ultrasound calibration validation literature.

in the presence of other sources of errors, but it is not sufficient to conclude about the goodness of calibration.

The robustness/reproducibility/repeatability of a system is another metric that can be assessed for any calibration method [70]. In this quantitative test, instead of measuring the error based on a single calibration transform and scanning a target from diverse locations, multiple calibration transforms are computed and applied to the same target. This spread of measurements explains the repeatability of the results. In this form of experiment the effects of tracking, segmentation, and alignment errors are diminished because scanning a target is not required, so that any pixel in an image can serve as a target. However, the selection of a pixel within an ultrasound plane is important. It has been suggested that pixels around the 4 corners of an ultrasound plane, as well as the center of the plane, be chosen, so that the calibration error can be analysed properly [40, 51, 33, 73, 5].

Measuring trueness of calibration is not straightforward and almost impossible to determine [42]. In fact, any technique that can exactly determine the calibration error could possibly be used as the calibration method in the first place [34]. Thus, most of the trueness measurement procedures try to quantify the approximate errors by analysing the individual parameters of a calibration transform. Validation of trueness can be categorized into *in vitro* and *in vivo* methods. The *in vitro* studies assess the trueness using a well-defined geometric phantom in an ideal environment, which is considered to be an appropriate metric for validation in laboratory setting. In contrast, *in vivo* studies test the feasibility of a system in real tissue within a clinical environment. In addition to these methods, qualitative visualization is an easy and commonly used strategy for on the spot assessment of calibration results. This is achieved by overlaying the calibrated ultrasound with the virtual model of a tracked tool or a phantom in a 3D context.

1.2.3.2 Distance Measurement

In the similarity mode calibration, independent evaluation of the scale factors can be obtained by measuring the distance between the known targets in physical space [52]. The two known

targets in space enable us to have the precise distance between them. So by scanning the points using the calibrated ultrasound probe, the points can be reconstructed in 3D space, and measuring the distance between them verifies the goodness of computed scaling factors through the calibration method. The only error that might be included in this type of measurement is the TLE, which occurs while segmenting the target points in the ultrasound image.

1.2.3.3 Volume Measurement

Volume measurement is another metric for assessing the overall performance of scaling factors. In this approach, an object with known volume is scanned by a 2D calibrated ultrasound from different directions and orientations [73]. After performing the segmentation of the object with 'known volume' in each ultrasound plane and applying the calibration transform to the fiducials, the resultant is the reconstructed volume of the object in physical space, which needs to be compared against its 'true' volume. The difference between the reconstructed and the 'true' volume demonstrates the accuracy of the estimated scaling parameters. In real-time 3D ultrasound, minimum a single acquisition is required to identify the boundary of the object and therefore reconstruct the specified volume in physical space. However, due to the poor resolution of the real-time 3D ultrasound compared to 2D ultrasound, the reconstructed volume from this approach may be worse.

1.3   Augmented Virtuality in IGS

Augmented Virtuality (AV) and Augmented Reality (AR) are the two principal means by which computer technology will be used in reality and offer the optimum surgical environment [60, 59]. The information can range from absolutely real (directly observed objects) to virtual (computerized simulations) and is aimed to enhance or enable delivery of therapy under limited visualization and access conditions. Cardiac interventions are special in this sense because of the complications in access, limited FOV, dynamic nature of the heart, and surgical

tools manipulation. The use of guidance technologies could be extremely helpful in these pro-
cedures [53]. As an example, Moore *et al.* [61] proposed a navigation platform that was used
for guidance of a transapical tool for MV repair procedures. The intended guidance system
overcame the safety concerns of the tool navigation, from the apex of the heart to the target
area, which was previously performed under TEE imaging alone (described in Sec. 1.1.1). This
approach demonstrated a significant improvement in terms of time, safety, and consequence of
surgeons experience, by providing a platform that contained the virtual model of the tracked
surgical tool, calibrated TEE probe, and high-risk areas in a common 3D space. The accu-
racy in these navigational systems is crucial since any type of inaccuracy may lead to wrong
targeting, misguidance, and may results in damage to healthy tissue. The performance of the
guidance system is tied to the accuracy of the tracking system, calibration of the surgical tool,
as well as calibration of the TEE probe which is the main focus of this study.

1.4 Ultrasound Calibration during Surgery

1.4.1 Speed-of-Sound Mismatch

The formation of an ultrasound image depends on the speed-of-sound of a medium. For exam-
ple, the appearance of an object in ultrasound differs when the speed-of-sound of the medium
changes. Most ultrasound manufacturers assume the scale parameters based on 1540 m.s^{-1}
speed-of-sound, which is the average speed-of-sound in human tissue. To perform the calibra-
tion, a medium often matches the speed-of-sound in human tissue or in water (20°C), where
the speed-of-sound of 1480 m.s^{-1} [22] is being used. When water is chosen, either the temper-
ature needs to be increased to 50°C, which increases the speed-of-sound to 1540 m.s^{-1}, or the
pre-defined scale parameters (by the manufacturer) need to be corrected based on room temper-
ature water [48, 43]. Alternatively, scaling parameters can be computed directly by scanning a
phantom.

Increasing the temperature of water to the required temperature and maintaining it through-
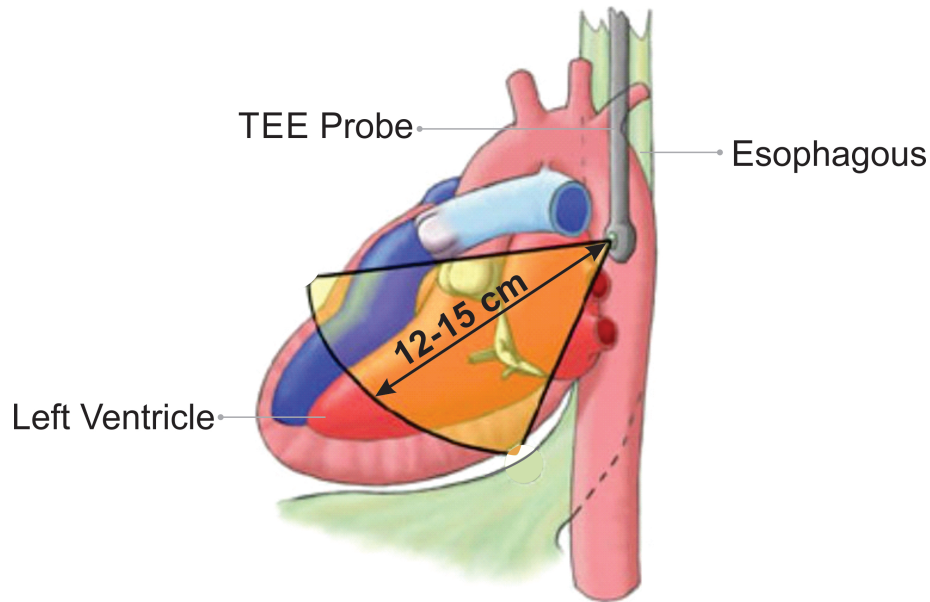
Figure 1.14: TEE placed at mid-esophagous to image LV and MV. Often depth of an image is set to 12-15 cm to perform scanning task. † Adapted from [86].

out the calibration process is a challenging task. In addition, depending on the organ of interest being scanned, the speed-of-sound at the target site of surgery may differ significantly. For instance, in biological liquids and soft tissues the speed-of-sound ranges between 1400 m.s^{-1} to 1800 m.s^{-1} [83]. Therefore, due to the variation of fat content among patients, speed-of-sound varies accordingly (patient specific). The speed-of-sound is temperature-dependent and not frequency-dependent. The speed-of-sound in blood at 37°C is reported as 1580 m.s^{-1} and in cardiac muscles as 1576 m.s^{-1} [57]. There is also a significant difference in the speed-of-sound between normal and diseased tissues such as myocardium [74]. Thus, the target site of surgery is categorized as an in-homogeneity medium, in which predicting the 'true' speed-of-sound prior to surgery is almost impossible. Since the TEE is placed at the mid esophagus to scan the MV from 5-6 cm away (refer to Fig.1.14), even small scale mismatch could lead to significant error at that particular depth.

1.5 Thesis Outline

This thesis proposes, for the first time, an 'in-situ' ultrasound calibration where a tracked surgical tool is used as a phantom to obtain the ultrasound calibration transform. Our technique utilizes the trans-apical surgical tool (NeoChord DS1000), which has the potential to accomplish ultrasound calibration while the tool is inside the left-ventricle of the heart, and the TEE probe is positioned inside the esophagous of the patient. The entire calibration process is automatic and occurs within a minute. The *in-situ ultrasound calibration* is a useful approach for both pre- and intra-operative ultrasound calibration in minimally invasive mitral valve repair surgery.

Chapter 2 of the thesis covers the complete work-flow of our proposed calibration method as a whole. The first objective specifically defines the concept of an *in-situ* ultrasound calibration, describing a directed surgical tool as a phantom for computing the calibration transform. An experimental simulated surgical scene depicted an actual target site of the surgery, to test the feasibility of our approach in a laboratory setup. Moreover, extensive validation techniques have been applied to quantitatively indicate the overall accuracy of the system. The second objective focuses on a comparison of bi-plane vs. single-plane ultrasound imaging, reflecting the quality of ultrasound calibration. Detailed validation experiments provide a quantitative assessment on how well each of the two methods performed in different respects, such as ultrasound acquisition requirements, accuracy in terms of scaling parameters, the time and the overall robustness of calibration performance. The third objective emphasizes the variability of calibration accuracy, exclusively based on the identification of the surgical tool intersection with the ultrasound plane as a source of information for computing the calibration parameters. In this section, the automatic segmentation and identification of the tool with the ultrasound plane was compared to the manual identification by different users.

In the AR guided Mitral valve repair procedure, real-time 3D ultrasound is essential for the positioning of the surgical tool at the target site of surgery. Hence accurate 3D ultrasound calibration is a key requirement for this guidance platform. In the final objective, we propose

a new technique for computing the real-time 3D ultrasound calibration, which is derived from 2D bi-plane ultrasound calibration. Our proposed method offers a more accurate 3D ultrasound calibration: instead of using 3D ultrasound volume we used high quality 2D bi-plane ultrasound images along with the intrinsic relationship between the two modes.

Chapter 2

In-Situ Ultrasound Calibration

2.1 Directed Surgical Tool

Navigated transapical MV repair is a tracked ultrasound-based approach where calibrating the TEE probe with respect to the magnetic tracking system is a requisite. When calibration is obtained prior to surgery, different sources of error (as described in Sec.1.4.1) can cause inaccuracy in calibration, which become noticeable only while the procedure has begun. Incorrect overlay between the virtual model of the surgical tool and its ultrasound reflection in the AV environment is a sign of this. To resolve this issue, we first have to come up with a technique that performs the calibration in-situ and at the target site of surgery by using the surgical tool. Our method is able to compensate for the speed-of-sound at the target and achieve the ideal calibration during the procedure. The proposed approach adopts the line-based calibration [46] based on the orientation of the tracked surgical tool while being scanned by the bi-plane ultrasound. This technique does not require additional hardware other than the actual surgical tool for the purpose of computing the calibration transform.

This section focuses on how NeoChord DS1000, a transapical surgical tool for MV repair, serves as a phantom to compute the calibration transform. A left-ventricle phantom with transapical access is used to simulate the actual surgical scene in a laboratory setup. The in-situ

35
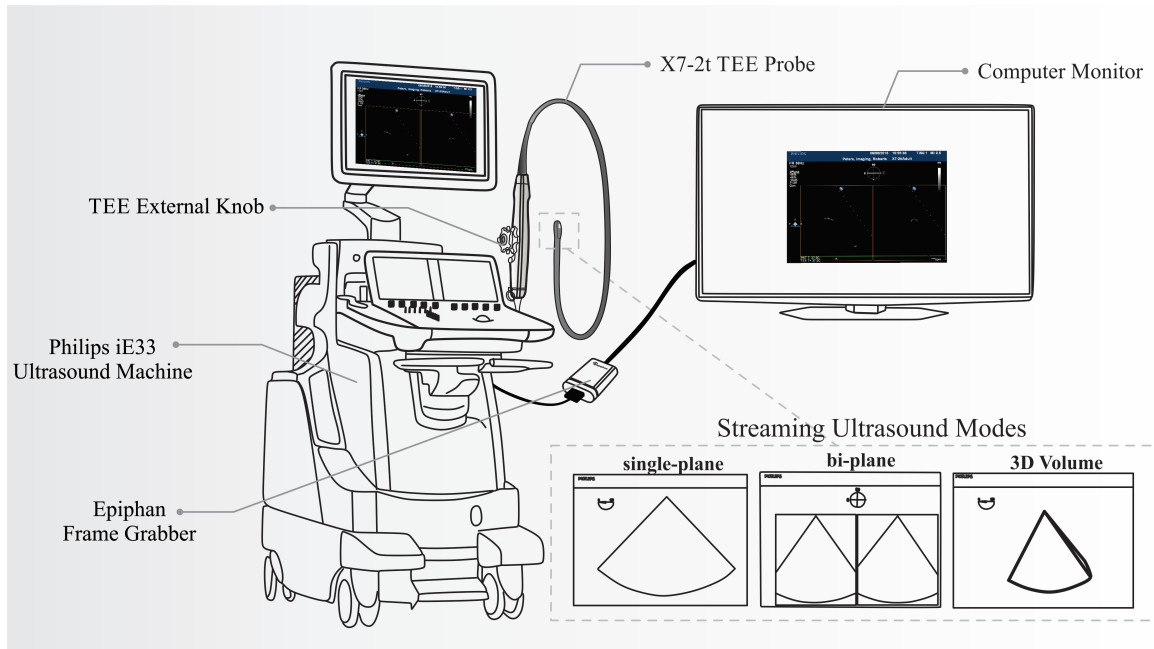
Figure 2.1: The iE33 ultrasound machine with the TEE probe. The probe is capable of producing three imaging modes of: single-plane, bi-plane, and 3D volume. The ultrasound machine is connected to the computer through the Epiphan frame grabber so as to directly stream the information on the computer's monitor.

calibration requires the surgeon to manipulate the tool and the echocardiographer to adjust the TEE probe during surgery so as to obtain the calibration transform within a minute.

2.1.1   Tools and Methods

A Philips iE33 ultrasound machine, equipped with a live 3D TEE probe (X7-2t), was used in this study (Fig.2.1). This TEE probe has the ability to acquire, 2D single-plane, 2D bi-plane, and real-time 3D ultrasound images. The bi-plane ultrasound is based on two simultaneous 2D images that are spatially separated by a specific angle while sharing the same image origin (Fig.2.2). Individual planes in bi-plane ultrasound are related to each other by an internal transform. The origin is pre-defined as the top of 'plane 0', and then, 'plane 90' is simply being translated towards the origin and rotated 90°. In this thesis, the direction on an image that is away from the face of the TEE probe is referred to as the out-of-plane (depth of ultrasound). In contrast, the direction towards the width of the ultrasound fan is referred to as in-plane (See

(a)   (b)
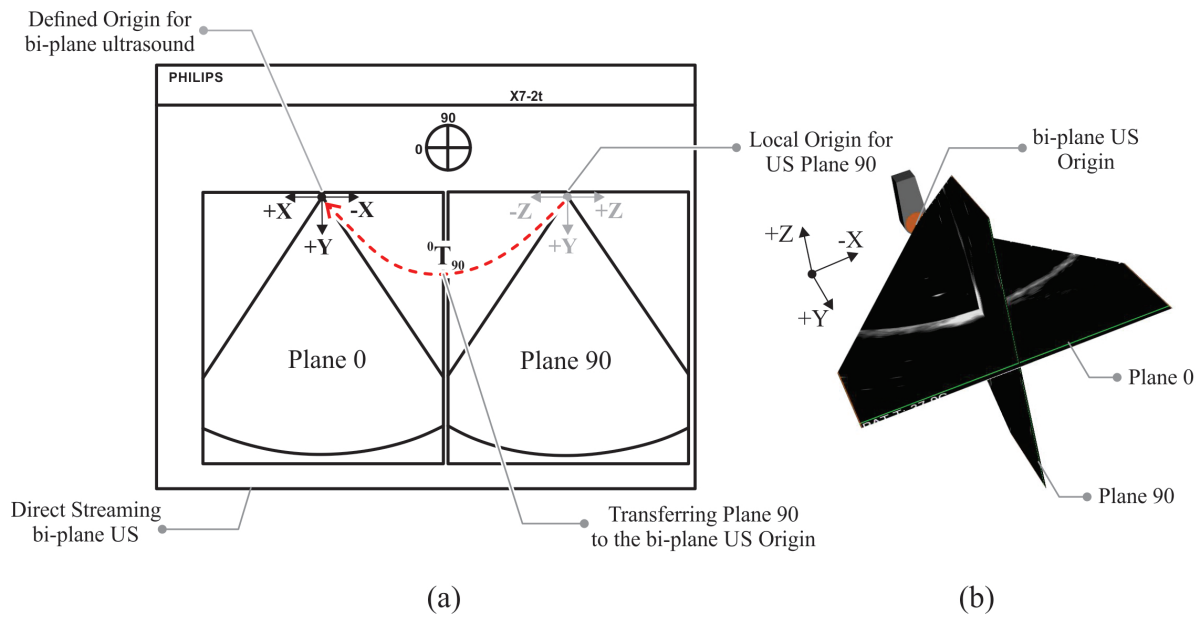
Figure 2.2: Internal calibration between the two planes of the bi-plane ultrasound image.
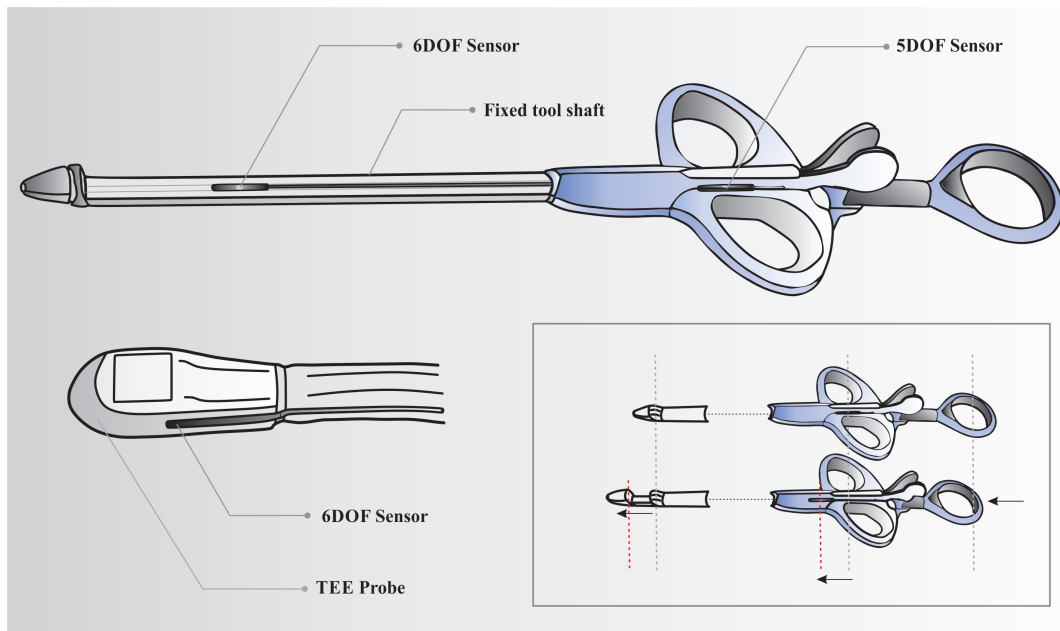
Figure 2.3: Integration of sensors to the NeoChord and TEE probe.

Fig.2.15C). Streaming 2D ultrasound images were acquired through an image frame-grabber (Epiphan System, Canada) at a resolution of 1680×1080 pixels, whereas streaming 3D volume were acquired directly from the ultrasound machine at a resolution of 112×48×112 pixels.

A magnetic tracking system, (Aurora, Northern Digital Inc., Waterloo, ON, Canada.) with a Table-Top FG, was used as a spatial tracking system in the operating room (OR) for this procedure. A 6-DOF magnetic sensor was externally attached to the tip of the TEE probe. In addition, two magnetic sensors, 5- and 6-DOF, were integrated within the NeoChord device to represent the real-time virtual geometry of the tool in the AV environment (Fig.2.3). The 5-DOF sensor, placed at the thumb ring, was responsible for reporting the opening and closing state of the tool tip (about 20mm) that was used for grasping the diseased MV leaflet (Fig.2.3). The 6-DOF sensor was attached near the distal end of the fixed tool shaft to track the tool.

In order to visualize the tracked NeoChord tool in an AV environment, local coordinate systems of the integrated sensors and geometrical model of the tool were calibrated. A custom-built jig was designed for this purpose, where the NeoChord device was placed precisely on the block, so that the tip of the tool was always held in the same location. The jig contained eight spherical divots in a non-symmetrical pattern along with a reference sensor positioned at a close proximity to the tool tip. Micro-CT of the jig served as the ground truth for creating the geometrical model of the jig with the origin of the model defined at the tool tip and the Z-axis along the length of the surgical tool. Based on the micro-CT data, the locations of the divots were defined for the model, by pointing the magnetically tracked pointer at each divot, the tracked surgical tool could be calibrated with respect to the 6-DOF sensor such that the origin and orientation of the tool becomes pre-defined (See Fig.2.4a).

2.1.2   Bi-plane Ultrasound Calibration

Our calibration paradigm extended the concept of the line-fiducial calibration [46] into the tracked NeoChord device, where in this context we call it 'directed' surgical tool. Because the origin and z-axis of the tool are pre-defined with respect to the integrated 6-DOF sensor, its ori-
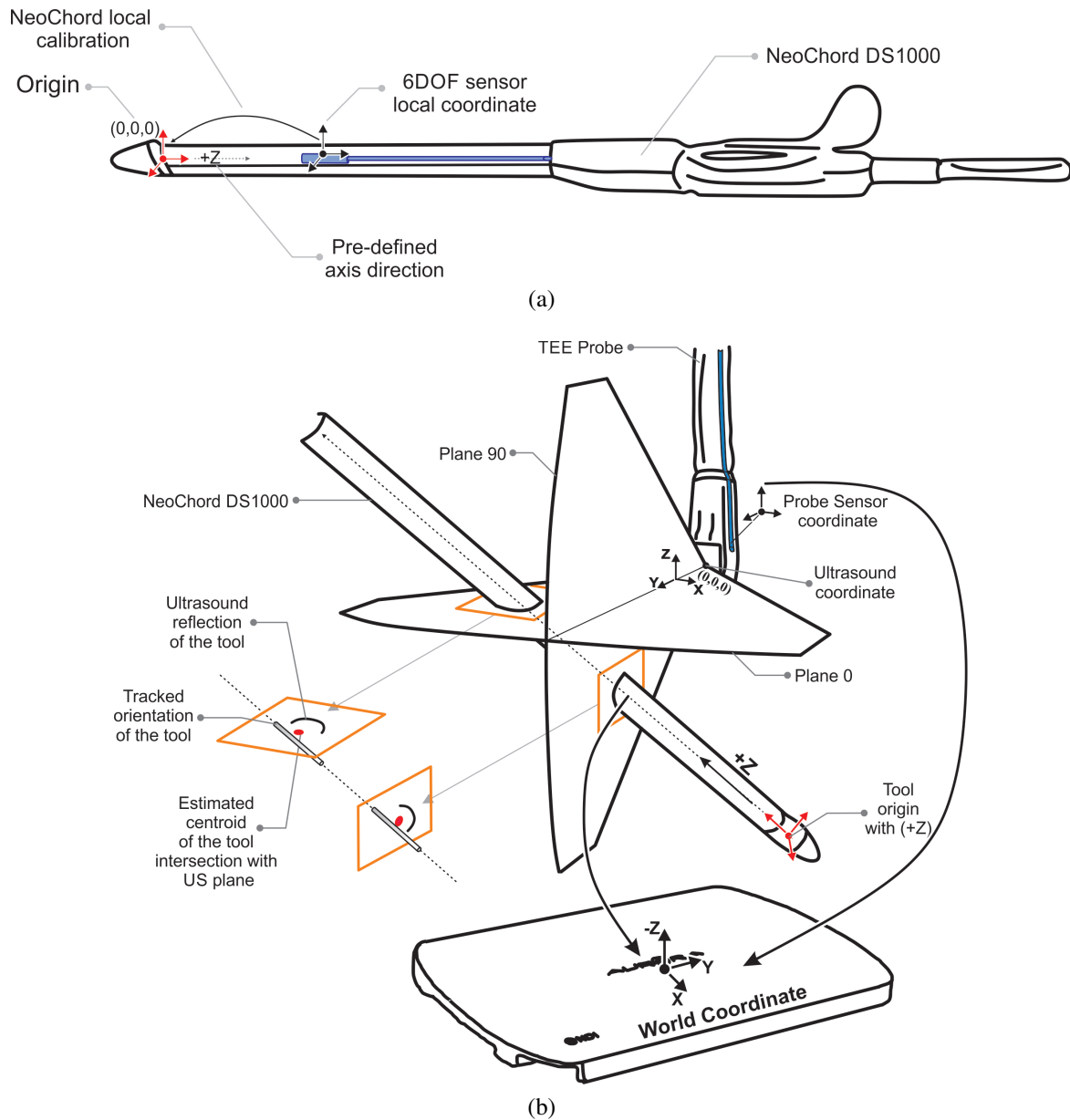
Figure 2.4: Schematic diagram relating devices to the tracking system. (a) NeoChord tool calibration for pre-defined origin and orientation with respect to the integrated 6-DOF sensor. (b) Bi-plane ultrasound calibration by intersecting the surgical tool with bi-plane ultrasound and relating the fiducials on image to the orientation of the tool in tracking system.

entation is known within the tracking system, in a similar manner as the 'line-based' approach (Sec.1.2.2.5.2) where a pointer with a known orientation was scanned by the 2D ultrasound. In our proposed method the directed surgical tool is scanned by the bi-plane ultrasound image, allowing us twice as many fiducials to be imaged in every acquisition (See Fig.2.4). In this case the fiducial is the centroid of the estimated ellipse, from partial-arc ultrasound reflection of the tool, in each plane of the bi-plane image[1]. Therefore, obtaining simultaneous fiducials from the bi-plane ultrasound and the tracking information, reflecting the tool orientation, enables us to perform the 'point-to-line' registration.

Orientation of the directed tool can be obtained from the normalized direction vector (L_z), extracted from the transformation of the embedded 6-DOF sensor in pre-calibrated tool ($^W T_{6dof}$). In addition, the two segmented fiducials from the bi-plane ultrasound are denoted as, $P_0 = (p_x, p_y, 0, 1)$ and $P_{90} = (0, p_y, p_z, 1)$ in pixel unit.

$$L_z = {}^W\mathbf{T}_{6dof} \begin{pmatrix} 0 \\ 0 \\ 1 \\ 0 \end{pmatrix} \tag{2.1}$$

In the case of an ideal transform, fiducials should coincide with the direction vector of the tracked tool in world coordinate system. This concept was thoroughly described in Sec.1.2.2.5.2. The calibration transform consisted of anisotropic scale parameters, (T_s) where $S_x \neq S_y$ and $S_x = S_z$ (inequality between in- and out-of-plane scales and equality in in-plane scales) (Fig.2.2), followed by the rotation and translation parameters in the form of a 4×4 matrix, (T_{rt}). Furthermore, fiducials are transferred to the world coordinate through the transformation (T_{ps}), read from the position sensor attached to the tip of the probe. Therefore, ultrasound fiducials should satisfy the following equations.

$$[L_z]_x \, [{}^W\mathbf{T}_{ps} \, \mathbf{T}_{rt} \, \mathbf{T}_s \, {}^{us}P_0 - {}^W P_{6dof}]_3 = 0_{3 \times 1} \tag{2.2}$$

---

[1]The process of identifying the centroid of an estimated ellipse can be done automatically. In this section the automatic segmentation has been applied for detection of the centroid. However, details regarding the automatic segmentation and identification of the estimated ellipse based on the ultrasound reflection of the directed surgical tool will be detailed in the 3rd objective of this chapter.

$$[L_z]_x \, [^W\mathbf{T}_{ps} \, \mathbf{T}_{rt} \, \mathbf{T}_s \, ^{us}P_{90} - {}^WP_{6dof}]_3 = 0_{3\times1} \tag{2.3}$$

Since the simultaneously acquired fiducials from bi-plane ultrasound images correspond to the same orientation of the tool in tracking system, respective transformations in both Eq.2.2 and Eq.2.3 should be similar. The operator $[.]_x$ converts a vector to a skew symmetric matrix to represent cross products as matrix multiplications of vectors. The operator $[.]_3$ converts homogeneous to Euclidean coordinates by dropping the fourth element and $0_{3\times1}$ demonstrates a null point.

Our method operates based on the optimization technique to compute the calibration. We employ the simplex method [66] to solve for the unknown parameters. The objective function for the minimizer is the angular difference between the direction vector secured from the tracking system and the estimated vector deduced through the calibration transform. The following equation describes this fact.

$$\{\mathbf{T}_{Cal}\} = \underset{[T_{Cal}]}{\arg\min} \frac{1}{2N_f} \sum_{i=1}^{N_f} |\, [L_z^i]_x \, [^W T_{ps}^i \, T_{Cal} \, {}^{us}P_0^i - {}^W P_{6dof}^i]_3 \,|^2$$
$$+ |\, [L_z^i]_x \, [^W T_{ps}^i \, T_{Cal} \, {}^{us}P_{90}^i - {}^W P_{6dof}^i]_3 \,|^2, \tag{2.4}$$

where $T_{Cal} = T_{rt}T_s$ and N_f is the number of tool orientations. To solve for a unique solution at least three different orientations of the tool are required, in which two unique fiducials correspond to every oriented tool for a bi-plane acquisition.

2.1.2.1 Initialization for Calibration

Our iterative optimization requires good initialization to solve for an accurate calibration. Starting off with poor initialization may lead the solution to become trapped in local minima and affect the optimality of the end result. The characteristics of the directed surgical tool, having a pre-defined tip position in the tracking system, allows the initialization to be solved through point-to-point registration [39]. The known tip position of the directed tool in the tracking sys-
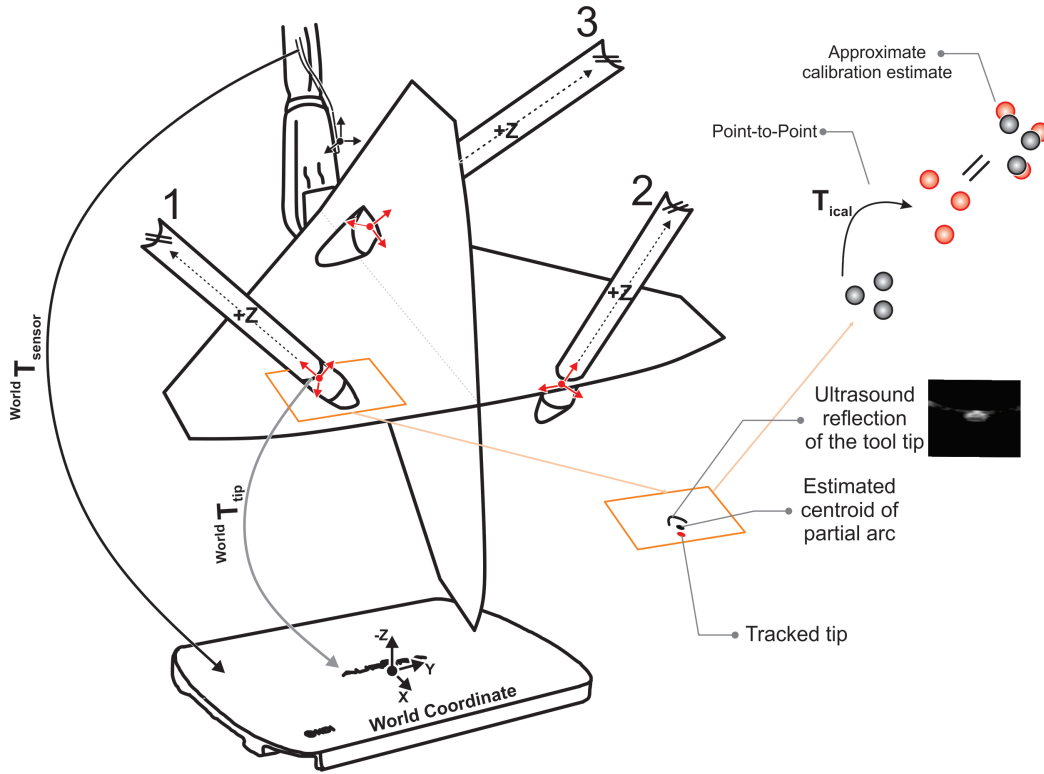
Figure 2.5: Intersection of the directed surgical tool tip with bi-plane ultrasound for estimating the initial parameters to be used in optimization process.

tem ($^{W}P_{track}$) and the pixel location ($^{us}P_{tip}$) found by scanning the tip (See Fig.2.5), establishes the following relationship:

$$^{W}\mathbf{T}^{i}_{6dof}\, P_{track} \;=\; {}^{W}\mathbf{T}^{i}_{ps}\, \mathbf{T}_{irt}\, \mathbf{T}_{is}\, {}^{us}P^{i}_{tip} \tag{2.5}$$

$$\mathrm{FRE} \;=\; \sqrt{\frac{1}{N_f}\sum_{i}^{N_f} |{}^{W}P^{i}_{track} \;-\; {}^{W}P^{i}_{tip}|^2}, \tag{2.6}$$

where T_{is} and T_{irt} are transformations consisting of the initial scale, rotation, and translation parameters. Paired-point registration based on the FRE metric is used to obtain these parameters. At least three or more tip positions over the ultrasound plane (non collinear) are required to achieve a unique initial solution. Once the initialization is achieved it can be used in the optimization process, while the user scans along the length of the tool to complete the calibration.
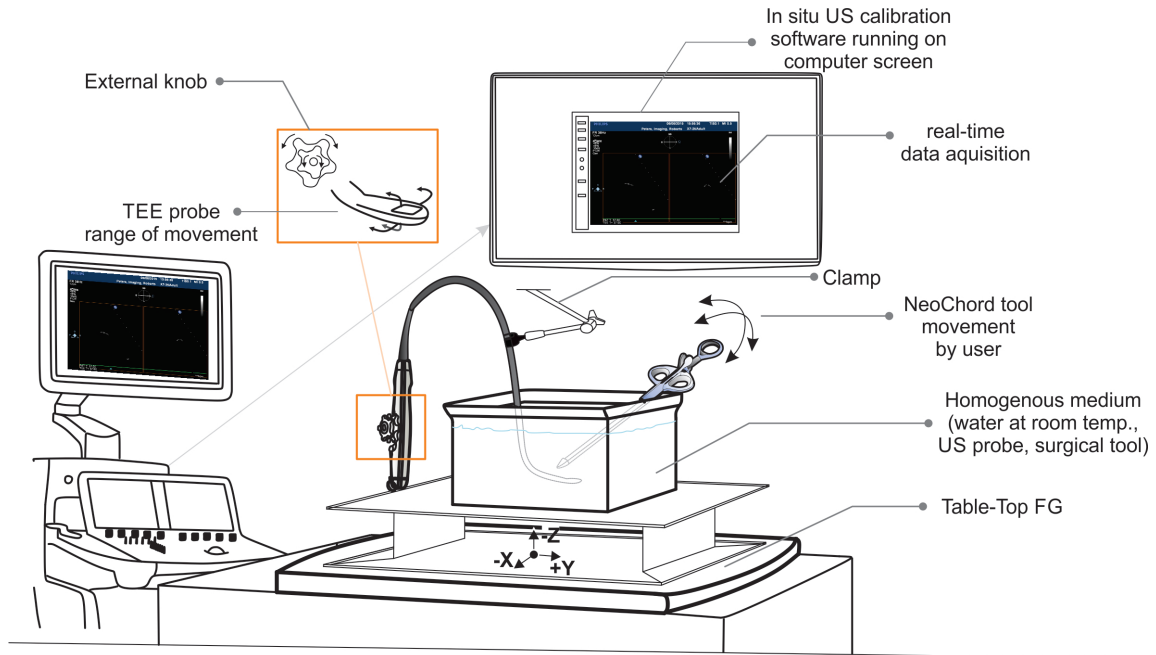
Figure 2.6: Experimental setup for the bi-plane ultrasound calibration using the directed surgical tool.

2.1.2.2 Experimental Setup in a Homogeneous Medium

A homogeneous medium in ultrasound calibration is one in which the speed-of-sound is uniform. This condition is often used to assess the performance of most proposed calibration methods in the literature. In order to test the efficiency of our bi-plane calibration, both the directed surgical tool and the tracked TEE probe were placed in a room temperature water to obtain the calibration. Such a regulated laboratory setup environment was chosen so as to check the quality, robustness, and stability of the calibration technique in itself.

To perform the calibration, a water-bath was placed on top of the Table-Top FG, and the TEE probe was clamped such that the probe's tip was positioned in water (Fig.2.6). In order to manipulate the tip of the probe, the user could turn the external knob on the probe and acquire bi-plane images from different poses. Also, the directed surgical tool was freely moved by the user to perform the calibration. To compute the initialization transform, the user was required to scan the approximate tip location of the directed tool by the bi-plane ultrasound (at least three different acquisitions). Upon obtaining the initial parameters, the directed tool was
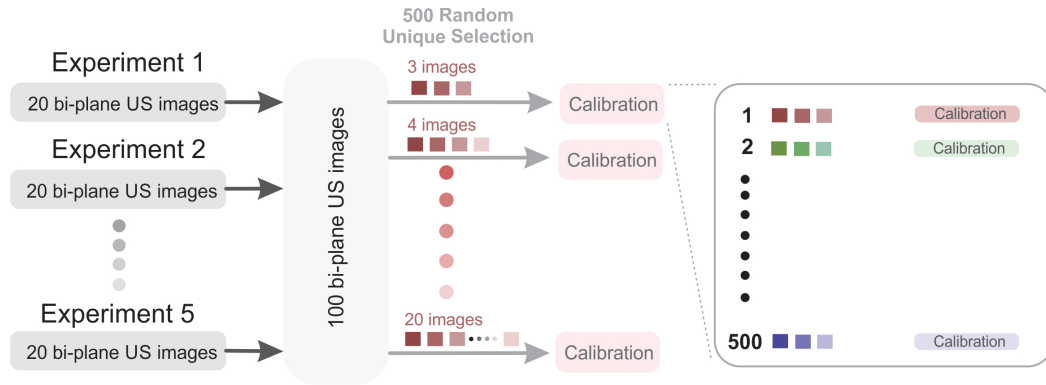
Figure 2.7: Monte Carlo experiment in ultrasound calibration

scanned along the length of the tool-shaft, while the tool in each acquisition was intersected with both planes of the bi-plane image. The scanning process is critical for the calibration, since achieving the unique pose of either the directed tool or the TEE probe in each acquisition is essential. Also, scanning the tool over the larger space (in- and out-of-plane range) in the ultrasound plane could lead to a more accurate calibration result.

The experimental procedure was repeated five times. Prior to each experiment, devices were readjusted and the tracking system was reset. In each experimental setup, 20 bi-plane ultrasound acquisitions were recorded and each of them corresponded to the unique tracking or ultrasound information. Thus in total, a dataset containing of 100 bi-plane ultrasound images was created. This enabled us to perform the Monte Carlo simulation experiment and assess the accuracy, reproducibility, and stability of the calibration procedure (Fig.2.7). A set of k datasets were randomly sampled from the total of 100 acquisitions ($k \in [3 \cdots 20]$), from which two sets of calibrations were derived. One set solves for the rotation and translation parameters with having pre-computed corrected-scale (CS RT), and the other for the scale, rotation, and translation parameters altogether (in-situ RTS). Note that for each k, 500 unique calibrations were computed.

To determine the corrected-scale parameters for the 'CS RT' calibration experiment, a precisely manufactured 'Parallel-Line' phantom was used (similar to a 'grid phantom' [25] which is compatible with MTS). The phantom has two layers, each consisting of 10 parallel 0.1 mm

thick nylon monofilament threads spaced at known distances, wrapped around an accurately machined frame. The distance between the parallel lines in each layer is incremented by 1 mm along the width of the frame, and the two layers are separated by 10 mm. These characteristics of the phantom permits measurement of the correct-scale parameters by scanning the phantom and relating the pixel counts with the corresponding known distances. The scale measurement experiment was implemented in the same controlled medium where the actual calibration took place. In addition, all three scales of an ultrasound image (s_x, s_y, s_z) were individually measured. So with pre-computed scales, the 'CS RT' calibration experiment ended up solving for only six parameters (rotation and translation) using the optimizer. On the other hand, the 'in-situ RTS' calibration experiment solves for all scales, rotation and translation parameters together. These two experiments allow us to assess the performance and stability of our calibration method, where the optimizer solves for more parameters, in the 'in-situ RTS' compared to the 'CS RT' approach.

2.1.3 Validation Techniques for Ultrasound Calibration

Assessment of the quality of individual calibration parameters is necessary for every proposed technique. For our calibration approach, proper evaluation of the scaling, as well as the rotation and translation parameters is requisite, which leads to determining the goodness of recovered parameters. Therefore, different validation metrics such as volume reconstruction, point reconstruction, and distance measurement were performed for this purpose.

2.1.3.1 Volume Reconstruction with Sphere

A precisely manufactured object with known volume is necessary for volume reconstruction (VR) measurement. In this regard, a table tennis ball with a known diameter of 39 mm was chosen to be scanned by the calibrated probe. The ball has strong ultrasound reflection about its surface boundary permitting accurate segmentation from the ultrasound image. In our experimental setup, the ball was positioned stationary within the calibration medium by using a

steady clamp. In the next step, the calibrated TEE probe was freely moved over the surface of the ball to obtain the bi-plane ultrasound images from different directions. Each bi-plane image consisted of the entire surface boundary of the ball in both planes of the bi-plane ultrasound[2]. Meanwhile, in each acquisition, the tracking information regarding the pose of the probe was recorded.

Once the data collection process was completed, the ultrasound reflection of the ball was manually segmented by the user. Ten points form each plane of the bi-plane ultrasound were identified, resulting in 20 fiducials (segmented points) for each acquisition. Subsequently, the calibration transform was applied to each of the points to reconstruct the ball in the tracking system. The centroid and radius of the estimated ball in the tracking system coordinates were achieved through the least square approach. The computed radius enables us to measure the volume of the estimated ball and compare it against the 'true' volume. Therefore, in this type of validation experiment, the overall goodness of scale parameters (combination of in- and out-of-plane) are being evaluated independently from the rotation and translation parameters.

At the same time, we could investigate the quality of the calibration parameters if we knew the 'true' center of the ball in the tracking system. In order to achieve this, a tracked pointer with a rigid straight metal tip (Aurora 6-DOF Probe, Northern Digital Inc., Waterloo, Canada) was used to digitize the entire surface of the ball. The digitized points demonstrated the surface of the stationary ball in the tracking system, and the actual centroid of the ball was obtained through the least square algorithm. Finally, the Euclidean distance between the centroid of the tracked ball and the estimated ball reflected the TRE measurement. Fig.2.8 illustrates the VR experiment. To qualitatively validate our calibration result, a surface representation of the tracked ball was created in the virtual environment. Then, a calibrated bi-plane acquisition was transferred to the common tracking coordinate system so as to demonstrate visual alignment between the ultrasound reflection of the ball and its virtually tracked surface position.

---

[2]Table tennis ball was filled with water to enable the appearance of the entire surface boundary of the ball in ultrasound images.
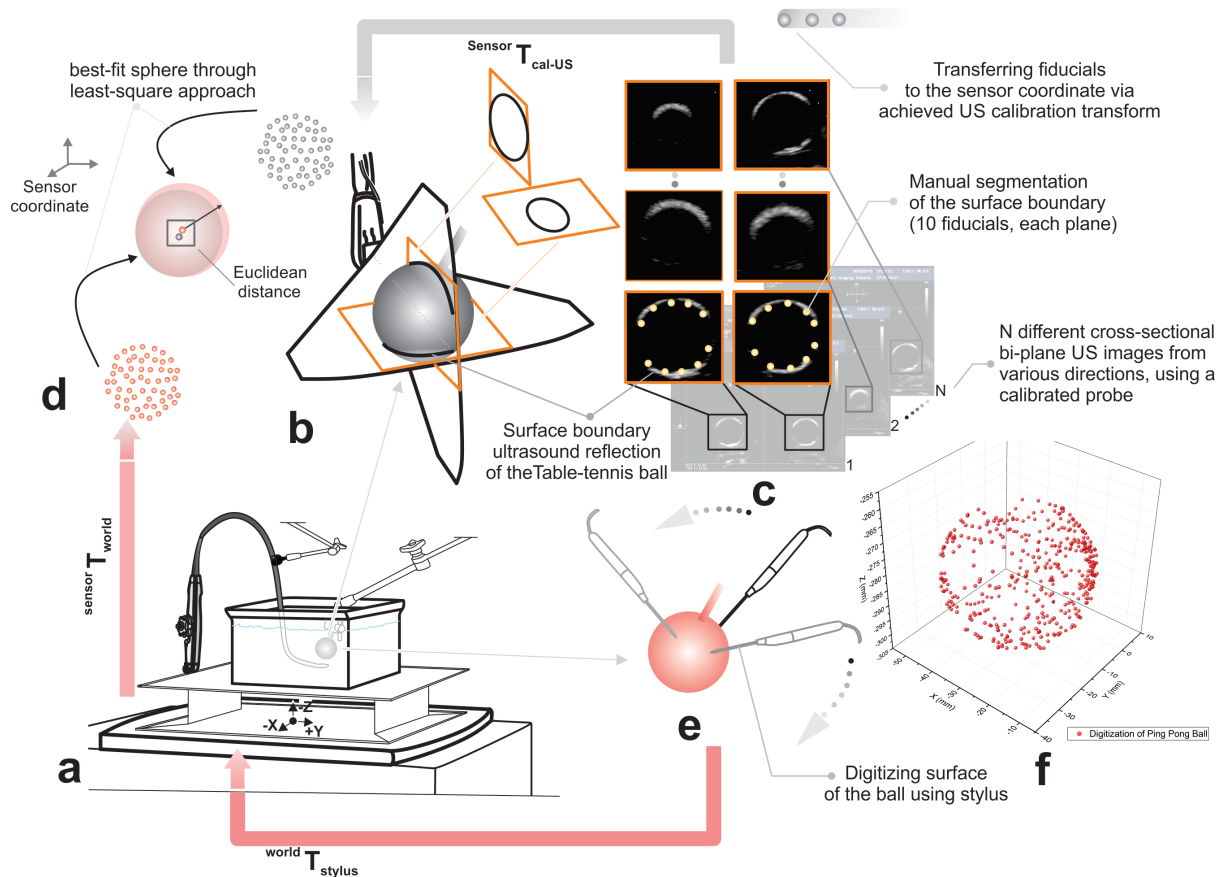
Figure 2.8: Schematic diagram of volume reconstruction accuracy. (a) Experimental setup: the TEE probe and table tennis ball placed in a controlled temperature medium (water) and located on top of the Table-Top FG. The position of the ball was fixed in space. (b) The calibrated tracked probe scanning the ball from different directions. (c) Ultrasound reflections of the ball were manually segmented. (d) Segmented surface of the ball achieved through ultrasound reflections were transferred to the sensor coordinate via computed ultrasound calibration. (e) A tracked stylus was used to digitize the surface of the stationary ball within the world coordinate so that the position of the center of the ball was known in physical space. (f) 400 digitized points collected on the entire surface of the ball in world coordinate system.

2.1.3.2   Measurement of Trueness and Precision

Point reconstruction (PR) measurement is an approach where a known point, in physical space, is scanned by the calibrated probe to determine the trueness and precision of the calibration method. In our validation experiment the tip of a tracked pointer was used as the ground truth (target). The pointer was firmly clamped such that its absolute tip position was fixed in water and within the acceptable field of the tracking system. To perform the precision analysis, the TEE probe was freely moved over the pointer's tip to acquire the bi-plane images from various directions and in different depths of the ultrasound fan. One challenge with scanning the sharp tip is the proper localization of the tip to minimize the TLE in the presence of the beam profile. Nevertheless, since we use the bi-plane ultrasound, simultaneous reflection of the tip in both planes of the bi-plane ultrasound facilitates the proper localization during the scanning process.

A dataset consisted of 65 bi-plane ultrasounds of the pointer's tip, and their tracking information was acquired. In each acquisition, the brightest pixel from ultrasound reflection of the tip was manually segmented (in either of the two planes of the bi-plane ultrasound). The segmented pixels were transferred to the tracking coordinate, passed via calibration transform. This procedure was repeated for all calibrations achieved in Monte Carlo experiment, 500 unique calibrations for every $\mathbf{k}$ ($k \in [3 \cdots 20]$) number of images used for calibration. Since the position of the pointer's tip is fixed in space, in an ideal scenario transferred fiducials based on different calibrations and different depths in ultrasound space should all meet at one particular point within the physical space. The precision of the measurements was calculated as follows:

$$\mathbf{SP}_{\text{precision}} = \sqrt{\frac{1}{\text{MN}} \sum_{i=1}^{N} \sum_{j=1}^{M} |\mathbf{T}_{Cal\ j}\mathbf{P}_{us}^{i} - \overline{\,_{j}^{W}\mathbf{P}_{us}^{i}}|}, \tag{2.7}$$

where $\mathbf{N}$ is the N of images for the pointer's tip, and $\mathbf{M}$ is the number of unique calibrations (i.e. repeated for every $\mathbf{k}$). The $\overline{\,_{j}^{W}\mathbf{P}_{us}^{i}}$ is the arithmetic mean of the ($_1\mathbf{P}_{us}^{i}$, $_2\mathbf{P}_{us}^{i}$, $\cdots$, $_M\mathbf{P}_{US\,us}^{i}$) points in the tracking coordinate system. Then, to measure the trueness, we should know where the 'true' position of the pointer's tip is in space. The tracked tip of the pointer can serve as the

ground truth for this purpose. So the measured distance between the transferred pixel position and the tracked position of the tip in tracking coordinate system is referred to as the trueness or bias of the calibration.

$$\boldsymbol{\mu}_{\text{trueness}} = \frac{1}{\text{MN}} \sum_{i=1}^{N} \sum_{j=1}^{M} | \, ^{W}\mathbf{T}_{ps}^{i} \, \mathbf{T}_{Cal \, j} \mathbf{P}_{us}^{i} - \overline{^{W}\mathbf{P}_{tip}} \, |, \tag{2.8}$$

where $\overline{^{W}\mathbf{P}_{tip}}$ is the mean of the tracking information corresponding to the stationary tip location, and the precision is given by the standard deviation. Fig.2.9 illustrates the experimental setup for this section.

2.1.3.3 Integration of In-situ Ultrasound Calibration into OR Workflow

Since the proposed method is intended to be used during surgery, it is important to determine at what stage of the AR guided workflow the calibration needs to be performed. The workflow requires, firstly, the calibration of the tracked surgical tool and the TEE probe prior to surgery. We may use our bi-plane method to calibrate the TEE probe in a laboratory setup. For the next step, the echocardiographer inserts the TEE probe and places it at mid-esophagus, such that the diseased MV and LV are visible in bi-plane mode. Then, the surgeon identifies a few points along the pertinent anatomy to represent the areas of interest within AR environment. Following that, the surgeon obtains an optimal orientation and entry point with the help of trajectory projection of the surgical tool. Once the apical access is achieved and 3-4 cm of the tool tip is advanced into the LV, the calibration can be assessed qualitatively. In the case of a mismatch between the virtual tool and its ultrasound reflection, then re-calibrating the probe at the target site is necessary.

At this stage, the echocardiographer needs to alter the TEE position to a transgasteric view so that the ultrasound reflection of the tool appears as a partial arc. This step is required because for our calibration, we need to identify the centroid of the estimated ellipse from the partial arc to solve for the unknown parameters. At this configuration, the movement range for either
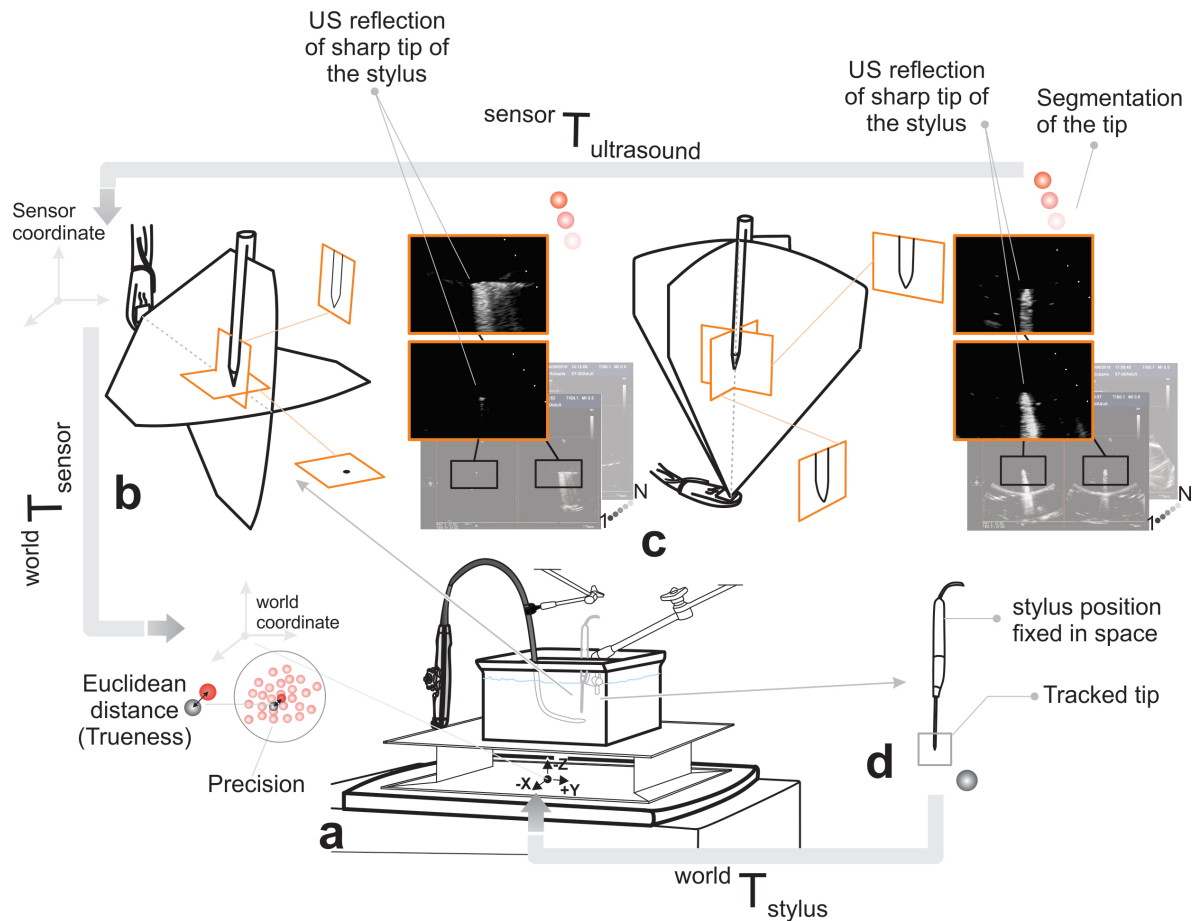
Figure 2.9: Point reconstruction accuracy using the tip of pointer. (a) Experimental setup for quantitative validation of the accuracy; stylus being fixed in space in which along the TEE probe it was placed in a regulated temperature medium. (b) Scanning the tip of the stylus using two simultaneous ultrasound reflections. Appearing as a point on one plane and a cross-section of the stylus's body across the length on the other plane. Ultrasound scanning repeated from different directions and depths within an ultrasound image. (c) Another possibility for efficient localization of the stylus, using bi-plane ultrasound. (d) During scanning process, the position of the stylus remained stationary and the tip was tracked all the time within world coordinate system.

of the tool or the probe is limited, although the echocardiographer could manipulate the tip of the probe, and the surgeon could move the tool slightly inside the LV to achieve different acquisitions. Once we get 10 to 20 bi-plane images, the software computes the calibration and visualizes the calibrated probe with the tracked virtual tool in a common coordinate to check the quality of calibration. Finally the calibration transform is updated and the surgeon can resume the AR guided procedure.

2.1.3.4 Simulated Surgical Scene

The feasibility of our proposed approach was tested in a simulated surgical scene. A silicon-made LV phantom was located in a water medium with an unknown speed-of-sound. The pre-calibrated TEE probe (calibrated in a homogeneous medium) was positioned below the LV phantom, imitating the TEE transgasteric view. The whole scene, relative angle and arrangement of the LV phantom with respect to the TEE probe, resembled the actual surgical scenario (refer to Fig.2.10). Also, transapical access was simulated by introducing the surgical tool through the base of the LV phantom.

Furthermore, to quantitatively validate the calibration in such a non-homogeneous environment, the tip of the tracked pointer was positioned stationary inside the LV phantom. Then, the calibrated TEE probe scanned the LV phantom with the pointer's tip inside, from transgasteric views at different orientations and directions. The tip of the pointer was manually segmented so as to transfer to the same coordinate system where the tracked tip position was recorded. The Euclidean distance between the tracked and transferred tip positions represented the TRE of the updated calibration transform within the non-homogeneous environment.

The estimated scaling parameters in updated calibration were evaluated through scanning a stationary table tennis ball inside the LV phantom. The TEE probe with the updated calibration scanned the LV phantom with the ball inside, from different directions and orientations. The ultrasound reflection of the ball boundary was manually segmented; 10 segmented points from each plane of the bi-plane ultrasound image were obtained. Then, fiducials were transferred
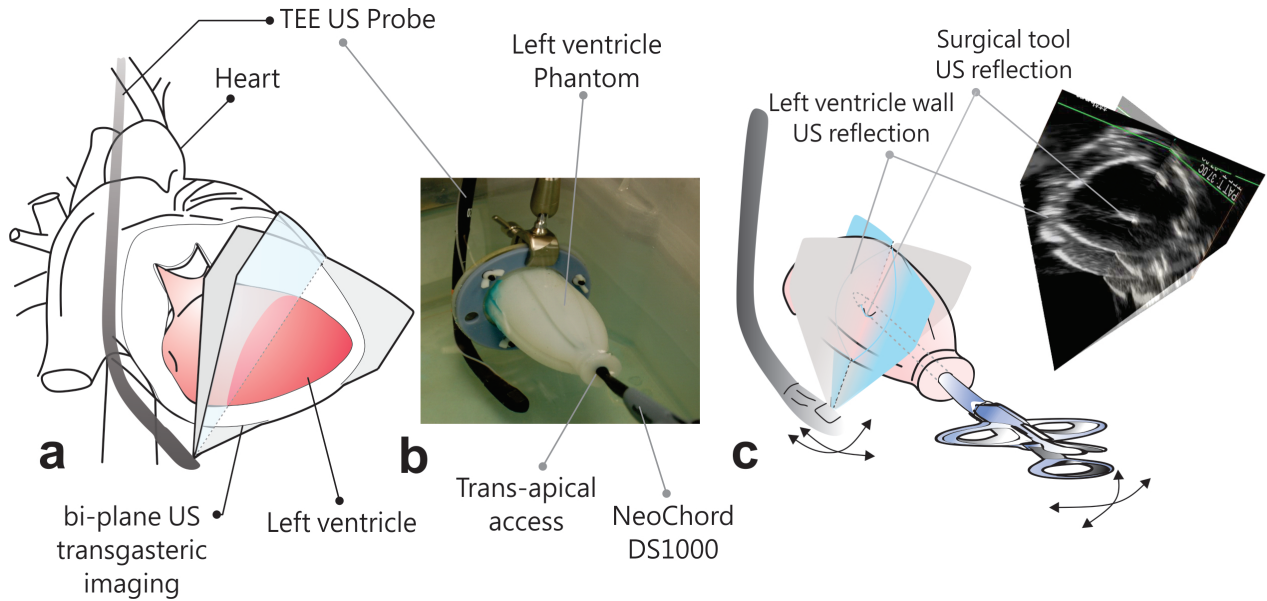
Figure 2.10: In-situ ultrasound calibration in a simulated surgical environment. (a) Schematic diagram demonstrating the transgastric bi-plane imaging of the LV during MV repair procedure. (b) Simulated scene in a laboratory setup using the TEE ultrasound probe, left ventricle phantom, and NeoChord DS1000. (c) Ultrasound reflection of the tool and left ventricle phantom during calibration process.

to the world coordinate system and passed through the least square algorithm [72] to solve for centroid and radius of the sphere. The estimated radius enables us to measure the volume of the ball and compare it against the 'true' volume to assess overall performance of the recovered scale parameters.

2.1.4   Results

The calibration results were based on the limited range of movement (Table 2.1) for the surgical tool and the TEE probe while obtaining calibrations. The overall rotation of the tool/probe was within ±16° and, the translations were ±19, ±36, ±22 mm in x, y and z directions, respectively.

The individual estimated calibration parameters for both of the 'CS RT' and 'in-situ RTS' experiments were plotted against the number of bi-plane acquisitions used in the calibration procedure (Fig.2.11). The rotation matrix was decomposed into X, Y and Z Euler angles using the 'ZYX' combination. The range between the solid lines in Fig.2.11 represents the standard

Table 2.1: Range of movement associated with the TEE probe and the surgical tool while performing the ultrasound calibration. (N) Refers to the number of bi-plane acquisitions.

	Minimum	25% Percentile	75% Percentile	Maximum	N
Rotation (deg.)	-16.59	-2.39	7.18	21	100
Translation X (mm)	-21.40	-7.97	6.92	25.68	100
Translation Y (mm)	-35.90	-19.11	15.67	43.22	100
Translation Z (mm)	-30.03	-7.09	11.67	22.42	100

deviation for the estimated parameters, where the corresponding data came from 500 unique calibrations at each specific number of acquisitions used for calibration. The plots suggests that in both methods, as the number of bi-plane images increases, the standard deviation decreases, and this fact conveys the higher stability of the calibration at higher acquisitions. In 'CS RT' experiment, lower variability of estimated parameters was seen at three to six acquisitions in comparison to 'in-situ RTS' calibration. Nevertheless, at higher acquisitions both methods tend to perform in similar fashion.

To measure the scaling parameters, we first used the on-screen caliper provided by the manufacturer (refer to Fig.2.12a). The scales computed from this approach were based on 1540 m.s^{-1} speed-of-sound for the target medium; the temperature is assumed by the manufacturer. Alternatively, we used the parallel-line phantom to determine the correct scales of the local speed-of-sound of the medium. Specifically, Fig.2.12(b,c) demonstrates the process of computing the correct scale parameters, served as the ground truth in 'CS RT' approach. The corrected-scales were reduced by 3.49% in the in-plane and 3.48% in the out-of-plane directions relative to the on-screen caliper measurement. In 'in-situ RTS', since scaling factors are estimated along with the rotation and translation parameters, goodness of recovered anisotropic scales were compared against the corrected scales (Fig.2.13). The scale accuracy in the in-plane direction (X or Z) was 0.09±0.57% error, and 0.46±0.42% error in the out-of-plane direction (Y), where tends to underestimate in both cases. The scale accuracy improved as the number of image acquisitions increased in computation of calibration, resulting in greater precision in out-of-plane direction than in-plane.
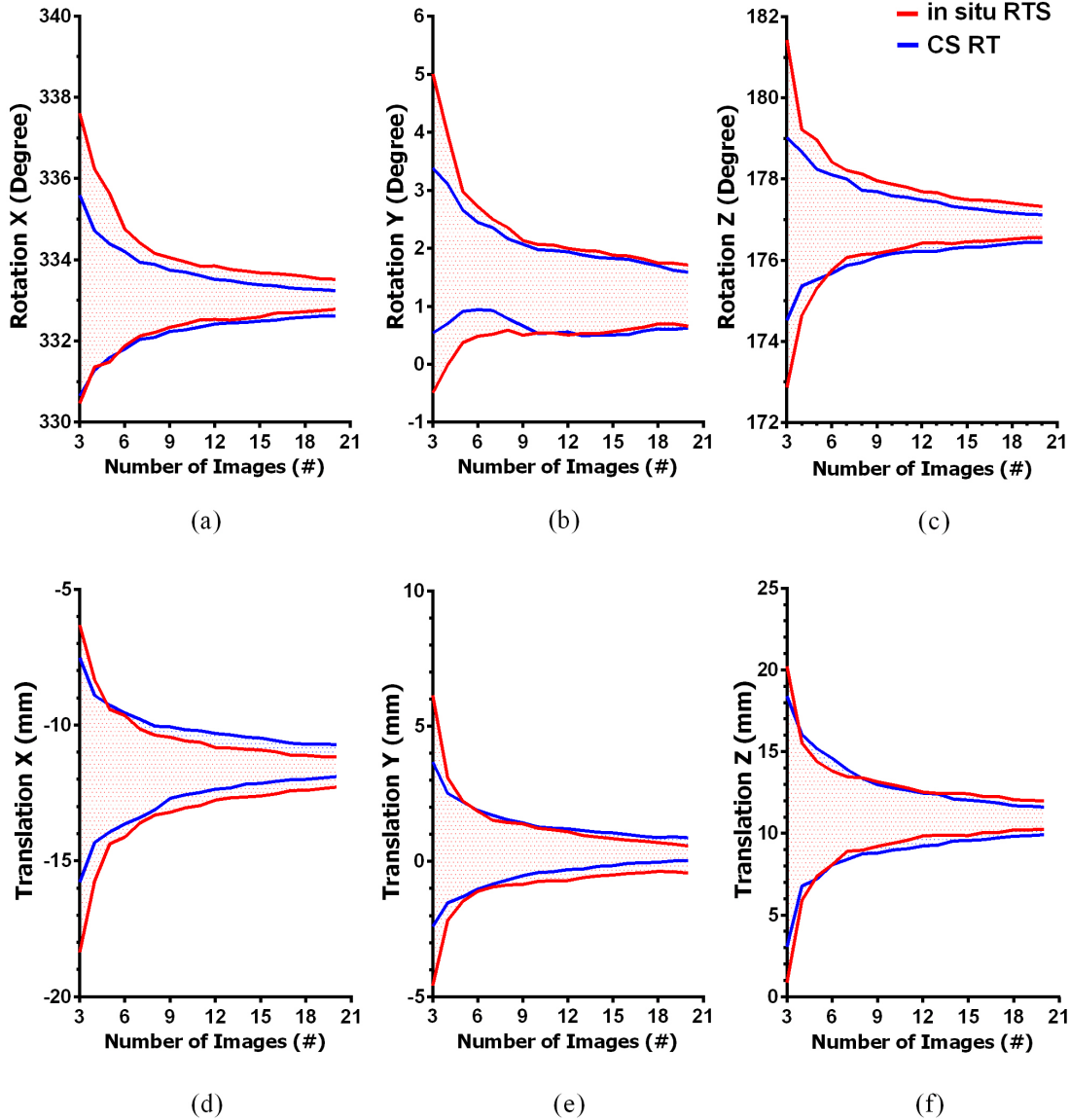
Figure 2.11: Demonstrates six calibration parameters (rotation, translation) solved through the minimization technique. The specified border lines represent the variability of the estimated parameters which have been computed for 500 unique calibrations at every image acquisition count. The *blue* boundary (CS RT) corresponds to the corrected-scaling calibration approach which solves for the rotation and translation parameters. In contrast, *red* boundary (in-situ RTS) solves for the rotation, translation, and scaling parameters all together (eight in total).

(a)

(b)

Scale (%)	On-Screen Caliber	Parallel Line Phantom	N	Localization Error (mm)
Lateral	24.85	24.01	20	0.0022
Axial	25.27	24.39	17	0.0001
Elevational	24.85	24.01	18	0.0024

(c)
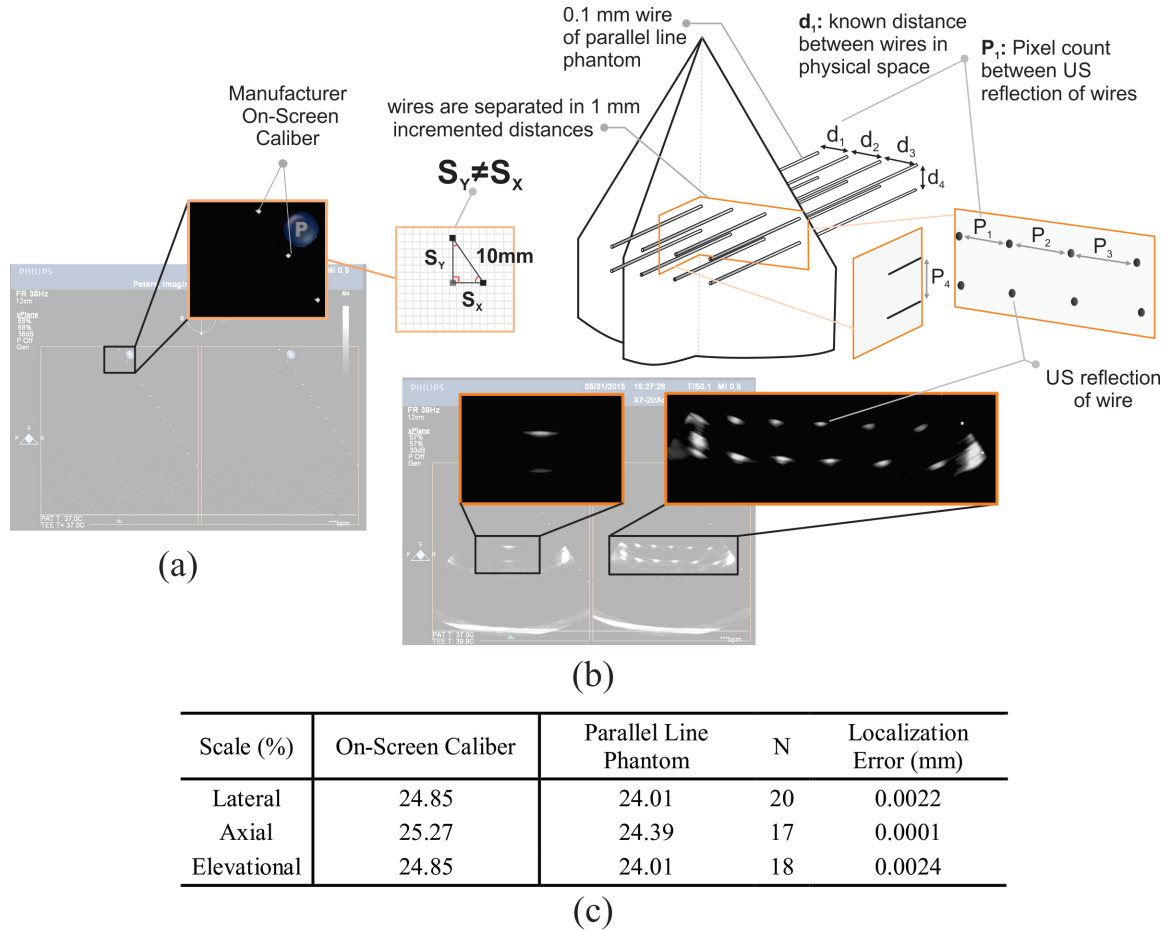
Figure 2.12: (a) On-Screen caliber provided by the manufacturer. The distance between the two brightened pixels on an ultrasound image is given as 10 mm. A crossed line over the two pixels enables us to measure the scales in axial and lateral directions, independently. Note that in-plane, lateral and elevation, directions have equal scales but are significantly different than out-of-plane, axial direction. (b) Precisely manufactured parallel line phantom, used to measure the correct-scale parameters. The simultaneous reflection of the wire threads appear as a point in one plane and a line in the other. Based on the known distance of wires in physical space and their pixels' difference through ultrasound reflections, the scale parameters were computed. (c) The scale measurements were reported as percentage per pixel. The phantom were scanned N times, and the scale parameters were computed.
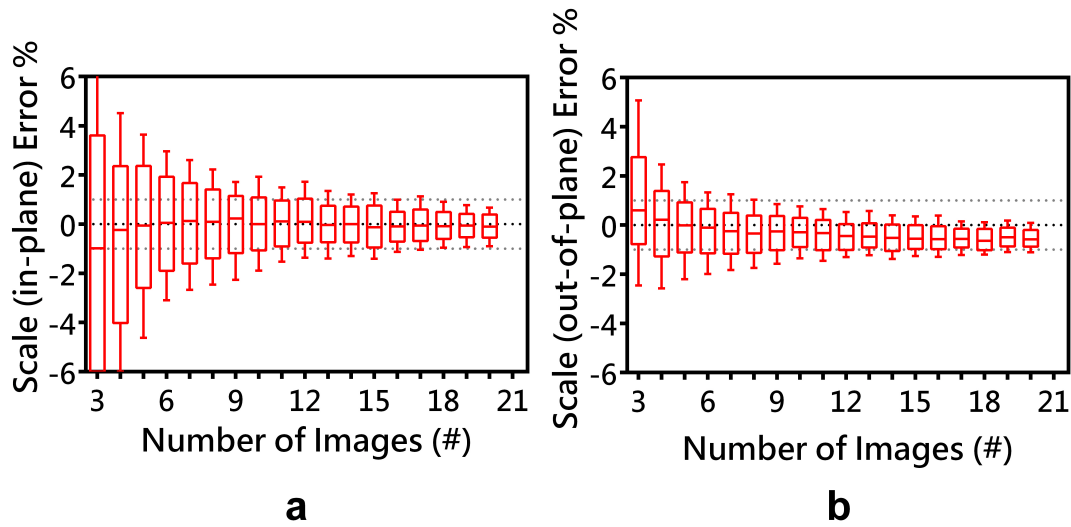
Figure 2.13: (a) and (b) demonstrates the scale difference between the estimated scales through 'in-situ RTS' and corrected-scale by parallel line phantom (ground truth) as percentage error. At every number of acquisitions, 500 scaling differences were computed. The box-plot represents the distribution of errors.

The overall accuracy of recovered scales was evaluated through the volume reconstruction accuracy. The volume difference error of the estimated table tennis ball was $0.36\pm0.67\%$ where similar to the previous scaling test, 'in-situ RTS' tends to underestimate the true volume (Fig.2.14). Also, the TRE achieved based on the centroid of the table tennis ball was 0.75 ± 0.43 mm.

The overall accuracy of the system was assessed through PR validation experiment (Fig.2.15). The plot in Fig.2.15a suggests significant improvement in terms of calibration accuracy with increase of image acquisition in calibration process. In addition, Fig.2.15b shows that 'in-situ RTS' method tends to perform as good as 'CS RT' after using 18 fiducials (9 bi-plane images) in calibration process, even with more parameters to solve for. The distribution of TRE for individual targets is shown in Fig.2.15(d, e), where the highest accuracy occurred at the middle of the fan and decreased slightly over the bottom and the top. The trueness of our method is as good as 0.88 mm and the precision, 0.32 mm (Fig.2.15f, g). Also, the lowest trueness and precision, 1.01 mm and 0.36 mm, corresponded to the bottom of the ultrasound fan.

a

b

c
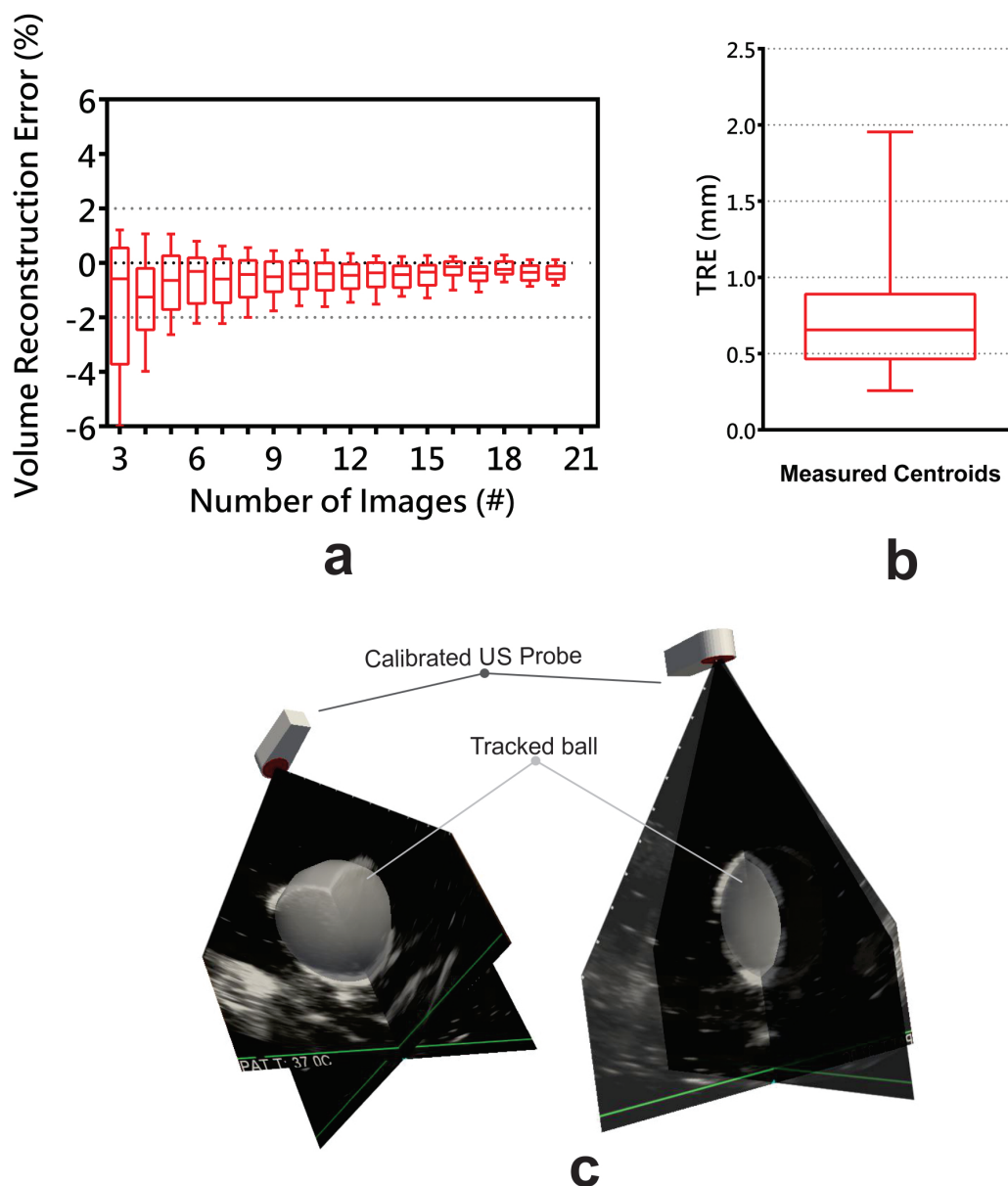
Figure 2.14: (a) Volume reconstruction error in (%) between the measured and tracked ball. Box-plot demonstrates the distribution of volume differences, for the calibrations with specific number of acquisitions. (b) Target registration error was based on centroid of the measured and the tracked ball. (c) Qualitative validation; visualizing the tracked ball in which calibrated TEE ultrasound probe overlapped with the ball in a common coordinate system. The virtual model of the tracked ball and its ultrasound reflection convey the quality of the calibration.
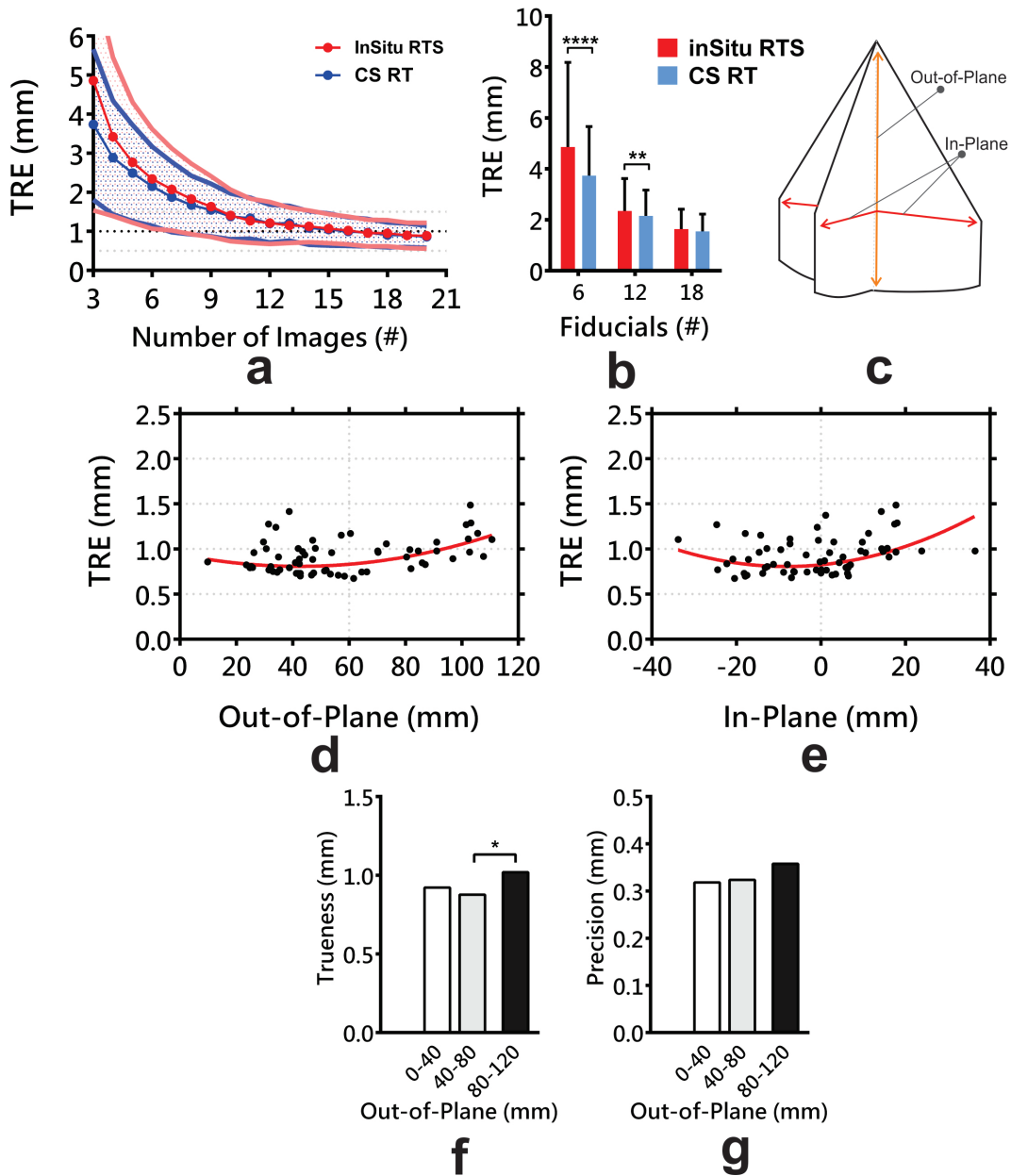
Figure 2.15: (a) Mean TRE of calibrations derived based on different numbers of bi-plane acquisitions. Measurements are based on 65 targets across the bi-plane ultrasound plane. Solid red line indicates the mean and borders, standard deviation, which are obtained from 'in-situ RTS' approach. Blue line and its border corresponds to the 'CS RT' approach. (b) Side by side comparison of fiducials' (#) effect on 'in-situ RTS' and 'CS RT' methods. Tukey multiple comparison test with 95% confidence interval has been applied to test the significance of difference. (c) Schematic demo of the In- and Out-of-Plane directions. (d, e) Demonstrates the TRE of the individual targets across the depth and In-Plane directions. The quadratic line fitted into the measured data. (f) The trueness of the calibration; separated into three sections across the depth of the ultrasound image. (g) The precision of the calibration; separated into three sections across the depth of the ultrasound image. * P<0.05, ** P<0.01, **** P<0.0001
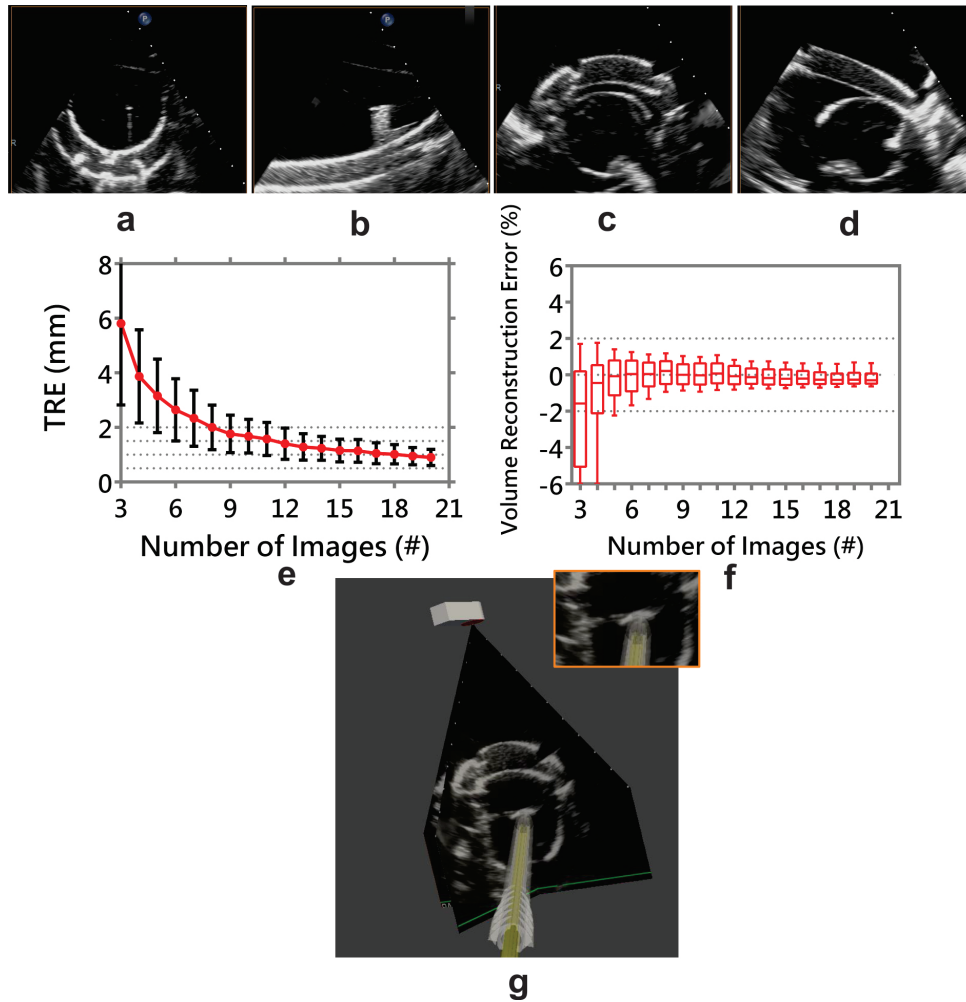
Figure 2.16: (a,b) PRA experiment: placing the tip of the pointer inside the phantom. (c,d) VRA experiment: placing the table tennis ball inside the phantom. (e, f) TRE and VRA results with respect to the number of images used during in-situ calibration procedure. (g) Qualitative validation: overlay of the virtual tool and its ultrasound reflection in AV environment.

Furthermore, our proposed method was evaluated by PR and VR accuracy in a simulated surgical environment with the TRE of 0.9±0.29 mm and VR error of -0.29±0.45% (Fig.2.16). The required time to perform the in-situ calibration was about 60-90 seconds. Note that most of the time was spent for manipulating the tool/probe during calibration in addition to the manually defining ROI on each image, in order to perform the automatic segmentation. In general, the time needed for the calibration process is proportional to the number of images used for computation.

2.1.5 Discussion

In this section of the thesis, for the first time, we presented the in-situ ultrasound calibration paradigm. Our approach uses the tracked surgical tool as a calibration phantom during MV repair surgery, the tool being inserted into the LV and scanned by the tracked TEE probe from transgastric view. Other calibration methods in the literature, despite having accurate results, are often required to be performed in a laboratory setup [42, 36, 64]. And usually such a medium has a different speed-of-sound and non-ideal conditions compared to the actual target site of surgery, leading to significant inaccuracy in calibration. For instance, the intended target site for MV repair is primarily composed of a blood pool and myocardium, which produces potentially higher speed-of-sound than $1540 \, \mathrm{m.s^{-1}}$. In addition, body condition and healthiness of the surrounding tissues could influence the alteration of the speed-of-sound between patients. All of these complications could affect the accuracy of the tracked ultrasound-based systems, and therefore our calibration method is the online solution to resolve these issues.

Our project was also first to obtain the calibration based on the bi-plane ultrasound imaging. Two simultaneous fiducials from each bi-plane image, with double number of constraints per acquisition, enables us to solve for the unknown parameters. Also, since both planes in a bi-plane ultrasound are orthogonal to each other and cover a larger space during acquisition, fewer DOF are required to solve for the calibration transform. Thus, our calibration could be solved with a lower number of acquisitions as well as fewer DOF compared to the previous 2D calibration procedures[3]. This is important when we are aiming to perform the calibration in-situ during surgery, where the surgeon and echocardiographer have limited room for moving the tools. In addition, the time required to obtain the calibration during the surgery must be as short as possible to have the least impact on the actual surgical workflow.

The side by side comparison of 'in-situ RTS' and 'CS RT' methods demonstrates that increasing the parameters to solve did not affect their proper estimation at higher acquisition. In

---

[3]In the next section we have thoroughly compared the performance of the bi-plane against the single-plane imaging for our directed surgical tool calibration method.

Table 2.2: Summary of the effect of increased parameters on TRE corresponding to the number of fiducials used in the calibration.

	inSitu RTS (8 Par.)		CS RT (6 Par.)		
Number of Fiducials	Mean TRE	Std. Dev.	Mean TRE	Std. Dev.	p-value
6	4.85	3.32	3.73	1.92	< 0.0001
12	2.34	1.27	2.15	1.01	< 0.01
18	1.63	0.77	1.54	0.67	NS

fact, there was no significant difference in estimation of parameters between the two methods at higher acquisition. The system tends to be more stable in terms of rotation and translation parameters after employing 18 fiducials (9 bi-plane images, see Table 2.2). This was clearly evident in the 'in-situ RTS' experiment solving 8 parameters rather than 6; significant instability was observed at lower acquisition (steep slope for n<9) than higher image acquisition (moderate slope for n>9), referring to Fig.2.11.

The scales achieved based on the parallel-line phantom were reduced in magnitude compared to the scales obtained from the on-screen caliper. This agrees with the fact that the ultrasound manufacturer assumes the speed-of-sound to be 1540 m.s^{-1} where water has a speed-of-sound of 1480 m.s^{-1}, which mean a reduction of 3.8%. Also, characterization of parallel-line phantom enabled us to repeat the measurements over different depths and through a series of uniquely known and measured distances. Thus, the localization error became negligible, and it suggested high-quality of ultrasound image in localizing the nylon threads. Therefore, it confirmed the true scales used as ground truth.

The estimated scales from 'in-situ RTS' method shows successful compensation for the correct speed-of-sound of a medium by comparing them with the ground truth scales. Specifically, estimated scales in out-of-plane direction were significantly more stable than the in-plane direction. This could be due to the greater uncertainties present in the in-plane than the out-of-plane direction while segmenting the centroid of the tool in an ultrasound image. From Fig.2.13, it can be deduced that our algorithm requires more images to get greater precision in the in-plane scale compared to the out-of-plane. Although, at higher acquisitions mean trueness

Table 2.3: Summary of scale parameters accuracy in the *in-situ* ultrasound calibration.

	Mean	Std. Dev.	N	Repetition
Scale In-Plane Error (%)	-0.09	0.57	20	500
Scale Out-of-Plane Error (%)	-0.46	0.42	20	500
Volume Reconstruction Error (%)	-0.36	0.67	20	500

of the in-plane scale outperformed the out-of-plane scale.

In the VR experiment the measured volume has been under-estimated in comparison to the 'true' volume by 0.36%. This was expected because our algorithm tends to under-estimate the individual scaling parameters as well (Table 2.3). Furthermore, the VR and PR experiments in the LV phantom confirm the accuracy of our method in a simulated surgical environment.

2.2 Single-Plane vs Bi-Plane Imaging in US Calibration

The accuracy of the directed tool calibration was compared between using the bi-plane and single-plane ultrasound imaging. The goal was to demonstrate the effect of double fiducials per acquisition in bi-plane imaging compared to the single fiducial per acquisition in single-plane ultrasound imaging.

2.2.1 Methods

The pre-calibrated surgical tool and the tracked TEE probe were placed in a homogeneous medium. The TEE imaging was set to the bi-plane mode and at the imaging depth of 12 cm throughout the calibration process. Both the tool and the probe were free to move such that the tool could be scanned from different directions and orientations. Each ultrasound acquisition was carefully done so that the ultrasound reflection of the tool appeared on both planes of the bi-plane ultrasound simultaneously. A dataset of 80 bi-plane images was acquired for this study. From the main dataset different subsets were sampled ($m \in [3 \cdots 40]$) such that 300 datasets, each containing m samples, were randomly chosen. For each set of m images, two sets of calibrations were derived: One, using the two fiducials corresponding the tool from the bi-plane ultrasound and the other, single fiducial from just one plane of the bi-plane image. To make a fair comparison between the two methods, the calibration accuracy was compared as a function of the number of fiducials being used in calibration process. The calibration quality was evaluated based on the PR and VR accuracy experiments, detailed in Sec.2.1.3.1 and Sec.2.1.3.2.

2.2.2 Results

Fig.2.17 demonstrates the accuracy of the calibration as a function of the number of fiducials. Based on 20 ultrasound acquisitions, the calibration accuracy through single-plane imaging was 2.77±1.03 mm (20 fiducials being used) and the accuracy through bi-plane imaging was
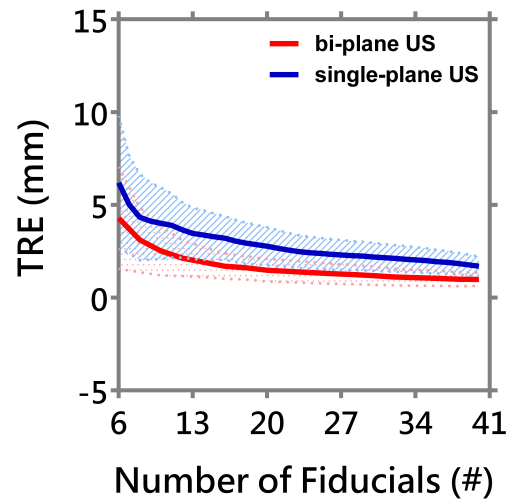
Figure 2.17: TRE as a function of the number of fiducials used in the calibration process. The *red* corresponds to the bi-plane and the *blue* to the single-plane based calibration.

0.96±0.32 mm (40 fiducials being used). Also, at 40 single-plane acquisitions (40 fiducials) the TRE of the system became 1.69±0.56 mm.

The Fig.2.18 demonstrates the VR results of the bi-plane and single-plane imaging in calibration. The plot suggests that, the increase of fiducials in calibration has great effect on the recovered volume and stability of the system. The VR error based on the bi-plane imaging in calibration was -0.58±0.72%, and based on the single-plane imaging it was -8.5±1.6%.

2.2.3   Discussion

The purpose of this validation experiment was to investigate how well the bi-plane ultrasound imaging works in comparison to the single-plane imaging for the ultrasound calibration. It is important to know which one of the TEE imaging modes is advantageous in similar conditions during the surgery. The results of this study suggested that, bi-plane imaging performed significantly better than single-plane ultrasound in terms of estimating the parameters. Also, bi-plane ultrasound provides double the number of constraints per same number of acquisitions. This helps the optimizer to have more information to solve for the unknown parameters. In addition, we could have a greater distribution of fiducials over the ultrasound coordinate system through
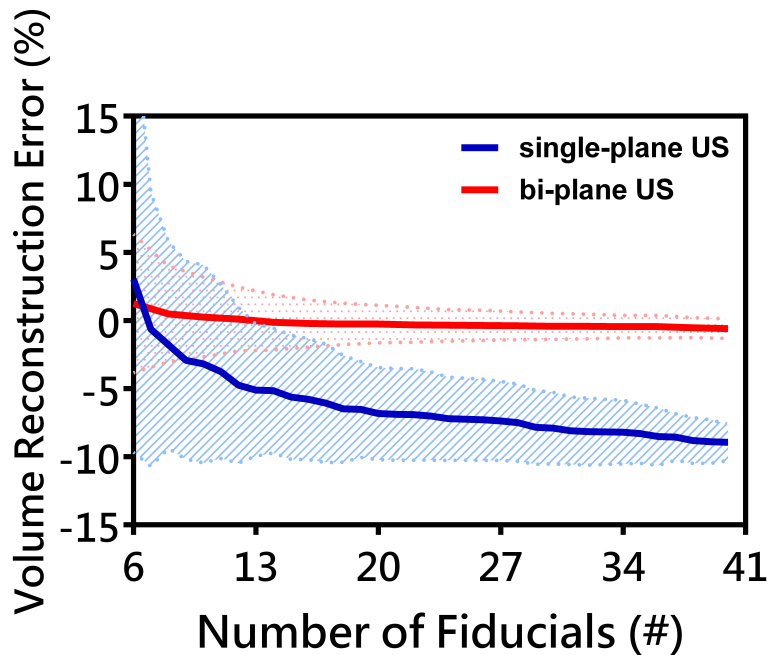
Figure 2.18: The volume reconstruction accuracy as a function of the number of fiducial used in the bi- and single-plane calibrations.

the bi-plane imaging, leading to more accurate calibration results.

In our results, we noticed that in single-plane ultrasound based calibrations most of the rotational error/misalignment occurred in the direction of the missing ultrasound plane; whereas on the same data, when we used the bi-plane ultrasound, the rotations on the corresponding direction were significantly improved. We can infer from the results that within limited range of movement in single-plane imaging, the distribution of the information was not sufficient for the optimizer to estimate the rotation parameter in the direction of the missing plane (ZY plane). This issue was significantly enhanced by the bi-plane ultrasound due to extra information acquired from the ZY plane. Similar results were seen for estimation of the scale parameters. In the in-plane direction, the information from the single-plane ultrasound was not sufficient to properly estimate the in-plane scale, and hence always under-estimated it. On the other hand, when bi-plane ultrasound was used, the estimation of the in-plane scale was significantly improved. As well, there was slight improvement in the out-of-plane scale as well.

2.3   Automatic vs Manual Segmentation - User Study

An automatic segmentation algorithm was developed to replace the laborious error prone manual process. The algorithm detects the ultrasound reflection of the tool and estimates an ellipse based on the segmented pixels. Then, the centroid of the estimated ellipse served as a source of information to compute the calibration. The ellipse estimation process was essential in this scenario because the ultrasound reflection of the tool appears as a partial arc, and not a complete ellipse due to the material properties of the tool.

To understand whether our automatic approach outperforms the manual one in terms of the end accuracy result in calibration, a pilot user study was conducted. Also, we were interested to know how consistent the accuracy of calibration is between different user's manual segmentation, in contrast to the automatic approach. Therefore, different users were asked to perform the manual segmentation, and the calibration result was compared against the calibration derived based on the automatic segmentation.

2.3.1   Methods

2.3.1.1   Automatic Segmentation in Ultrasound Calibration

Accurate segmentation of the tool in an ultrasound image is essential for our calibration procedure. The tool shaft is of cylindrical shape and made of the plastic material which appears as a partial arc in ultrasound image (Fig.2.19). The automatic segmentation system at first requires the definition of a region of interest (ROI) on the ultrasound image. The specified ROI is where our segmentation algorithm runs. The algorithm consists of three main steps; pre-processing, estimating the ellipse, and identifying the centroid.

In the pre-processing stage, a median filter followed by a canny edge-detection are applied to obtain a single-pixel-wide edge image. Then, the edge pixels (x_i, y_i) are stored in the vector $\mathbf{P} = [p_1, p_2, \cdots, p_N]$, where N is the total number of the edge pixels. These pixels correspond to the boundary of the tool's ultrasound reflection, composed of a cloud of pixels representing
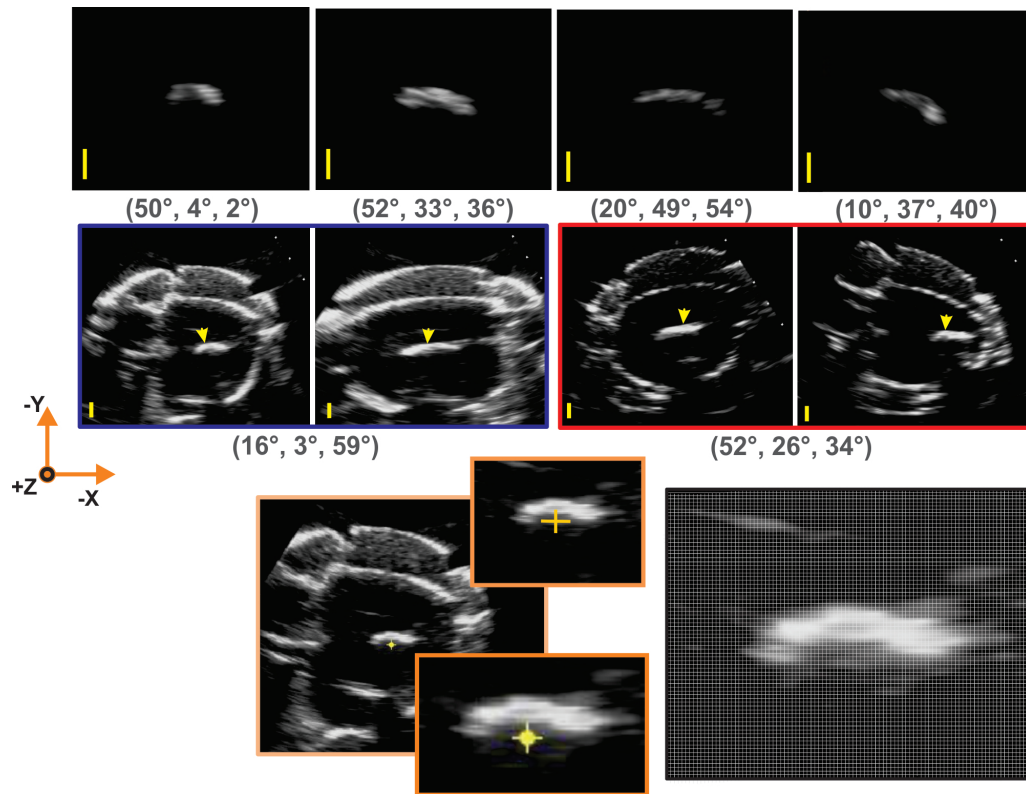
Figure 2.19: Ultrasound reflection of the NeoChord tool. The appearance of the tool while it is oriented at different angles. The second row illustrates the reflection of the tool while it is present inside the left ventricle phantom.
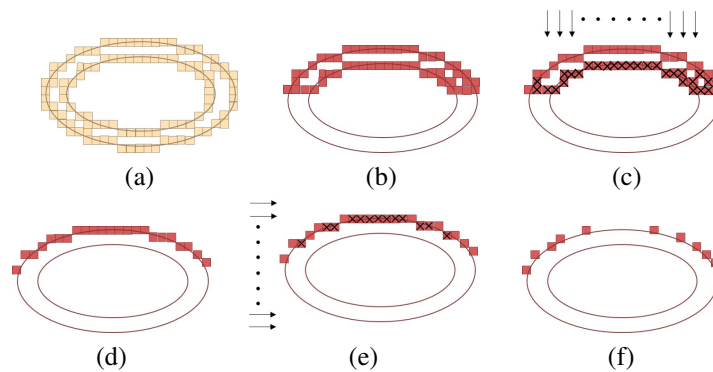
Figure 2.20: Pre-processing steps for automatic segmentation of the surgical tool's ultrasound reflection. (a) Ideal situation, where both inner and outer boundaries are being detected by the edge-detection process. (b) The single-pixel edge detection of the tool's ultrasound reflection. (c & d) The process of upper arc pixels selection and (e & f) are reduction of the extra pixels.

the proximal surface of the tool (Fig.2.20). We further reduce the pixels in the vector, **P**, by rejecting the lower arc pixels and keeping the upper arc. From the remaining pixels, if two or more pixels are being repeated in a row, only the first and last pixels are selected as the most likelihood edge pixels.

The next step is to estimate an ellipse based on the pixels being present in vector **P**. We seek the randomized Hough transform (RHT) [55] method to do this task. In this iterative approach, five random pixels are being picked in each iteration to solve for the five unknown parameters: major and minor axes, centroid of the ellipse coordinates, and angle of the ellipse ($r_{min}, r_{max}, x_c, y_c, \theta$). Then, sampled pixels are mapped to the parameters space by solving a set of equations. If a 'valid' ellipse is estimated, the count for the estimated parameters are increased by one and stored in a discrete storage, known as an accumulator. This process is repeated until the stopping criteria is met (predetermined number of samples). A count peak in the accumulators corresponds to a most probable ellipse based on the segmented pixels. We used five *one* dimensional accumulators, each of which stored the counts for one parameter, instead of a *five* dimensional accumulator to save storage space and to simplify the computation [50]. The following algebraic equations were used to parametrically model an ellipse [18]:

$$Ax^2 + 2Hxy + By^2 + 2Gx + 2Fy + C = 0 \tag{2.9}$$

Then, by solving the involved parameters and dividing by the constant C, the equation can be re-written as:

$$ax^2 + 2hxy + by^2 + 2gx + 2fy + 1 = 0 \tag{2.10}$$

Where the ellipse parameters are solved through the following equations:

$$x_c = \frac{hf - bg}{C} \tag{2.11}$$

$$y_c = \frac{gh - af}{C} \tag{2.12}$$

$$r_{max} = \sqrt{\frac{-2\Delta}{C(a+b-R)}} \tag{2.13}$$

$$r_{min} = \sqrt{\frac{-2\Delta}{C(a+b+R)}} \tag{2.14}$$

$$\theta = \frac{1}{2}\arctan(\frac{2h}{a-b}), \tag{2.15}$$

$$\text{where} \quad \Delta = \det\left(\begin{vmatrix} a & h & g \\ h & b & f \\ g & f & 1 \end{vmatrix}\right), \tag{2.16}$$

$R^2 = (a-b)^2 + 4h^2$ and $C = ab - h^2$ for the above equations. Therefore as of the last step in the segmentation process, the centroid of the estimated ellipse serves as a fiducial to be used in our calibration procedure. The segmentation is repeated for the unique intersection of the tool with the ultrasound plane and runs on both planes of the bi-plane ultrasound.

2.3.1.2   User Study

To evaluate the segmentation on the calibration result, our automatic algorithm was compared against 12 different users involved in the manual process. A dataset comprising of 23 bi-plane ultrasound images of the surgical tool being inside the LV phantom, was used for this purpose. The automatic algorithm was applied to all of the images and the segmented centroids were used to derive the calibration transform. Then, a Monte Carlo experiment based on the auto segmented points was performed, where a set of k dataset ($k \in [3 \cdots 20]$) was randomly sampled from the main dataset, repeated for 500 unique samples.

Alternatively, different users were asked to perform the manual segmentation on the same dataset. Users were required to visually interpret an ellipse from the ultrasound reflection of the tool so as to identify the corresponding centroid. Then, for each user, a Monte Carlo calibration experiment was obtained. Finally, PR accuracy experiment was performed to assess the goodness of the calibration results. Same set of targets were used for all the calibrations achieved.

2.3.2   Results

The TRE as a function of image acquisition is plotted in the Fig.2.21 for calibrations with different segmentation approaches. According to the results, the trueness and precision greatly
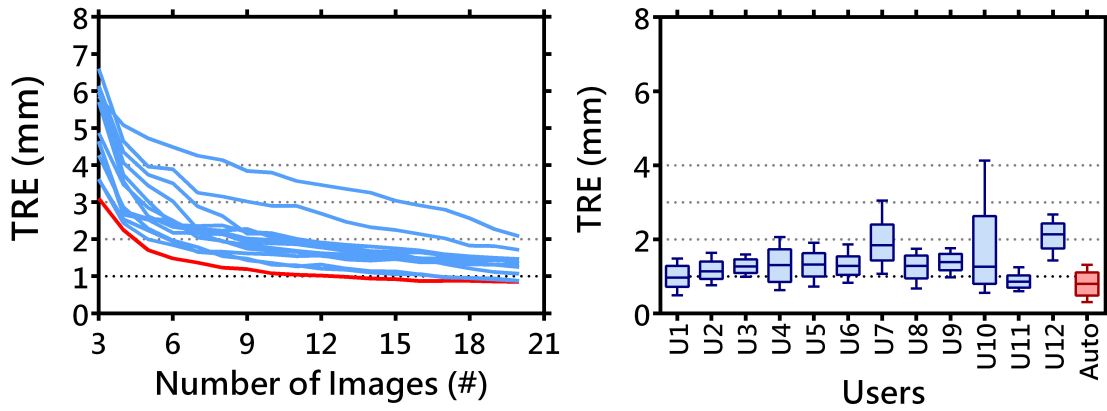
Figure 2.21: (a) TRE as a function of bi-plane acquisitions for all the users and the automatic segmentation. (b) Representing the TRE for the users and the automatic segmentation in which calibrations were computed based on 20 image acquisitions.

Table 2.4: The accuracy of the calibrations through the most/least manual and automatic segmentations. (N) is the number of images which utilized in calibration process.

	Trueness (mm)	Precision (mm)	N	Repetition
Best Manual Seg.	0.86	0.24	20	500
Worst Manual Seg.	2.08	0.47	20	500
Automatic Seg.	0.80	0.36	20	500

varies among users. Between all 12 users, the best two achieved calibrations of a sub-millimeter accuracy and one achieved the least accurate result of more than 2 mm (refer to Table2.4). In contrast, the calibrations derived based on the automatic segmentation were obtained with sub-millimeter accuracy in every attempt.

Fig.2.22(a, b) shows the fiducial localization of the individual users on the same dataset. Fig.2.22a corresponds to the distribution of fiducials (all users) segmented from XY-plane of the bi-plane ultrasound. Similarly, Fig.2.22b demonstrates the distribution in ZY-plane. In both the above-mentioned plots, fiducials are in a pixel coordinate, and all fiducials were normalized about the center of the point spread. Specifically, Fig.2.22(c, d) demonstrates the variability of fiducial localization between users in each direction in physical space. In XY-plane, there is greater instability of fiducial localization in the out-of-plane direction (Y) than in the in-plane
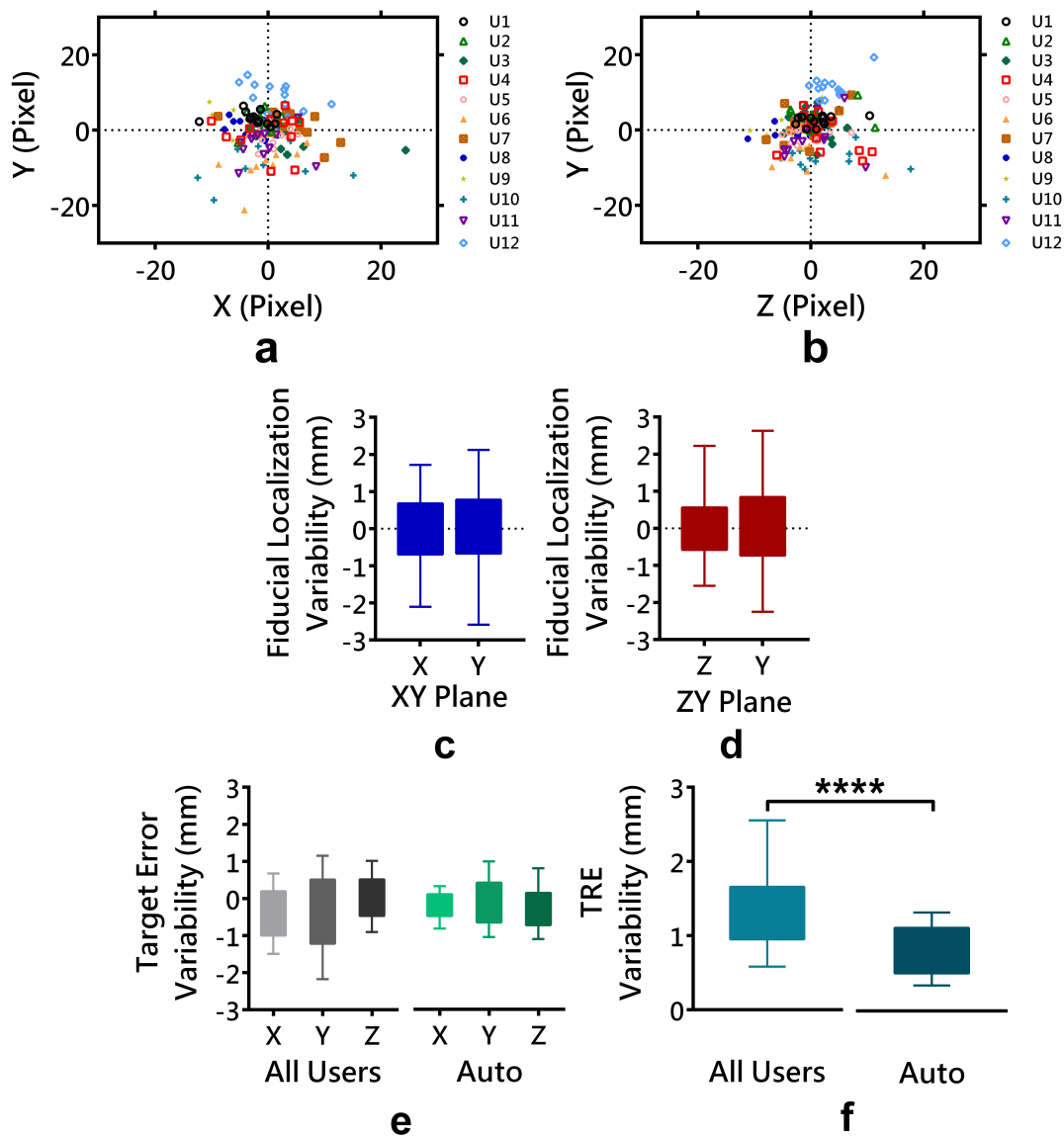
Figure 2.22: The variability of fiducial localization among users and the effect of it on the calibration accuracy. The localization effect was compared between manual and automatic segmentations.

Table 2.5: Summary of the decomposed target error for manual and automatic segmentations in ultrasound calibrations. All measurements are given in millimeter.

Seg. Types	X		Y		Z	
	Mean Err.	SD	Mean Err.	SD	Mean Err.	SD
Users	-0.38	1.0	-0.48	1.44	-0.4	0.78
Auto	-0.20	0.44	-0.08	0.76	-0.23	0.76

(X), ±1.36 mm and ±1.17 mm, respectively. Similar result is noted in ZY-plane, ±1.88 mm (Y) and ±1.62 mm (Z). In Fig.2.22e, the TREs of all calibrations achieved through manual segmentations were combined and decomposed into x, y, and z directions. The plot shows the distribution of errors in each particular direction among all users. Also, the TREs obtained based on the automatic segmentation were decomposed into x, y, and z directions and included in Fig.2.22e. There is significantly less variability of calibration error, in each direction, based on the automatic segmentation compared to the manual ones. In Fig.2.22f, the instability of the calibration accuracy by manual segmentation of different users was shown against the calibration accuracy from automatic segmentation.

2.3.3 Discussion

In this study we have focused on the variability of the calibration accuracy based on manual verses automatic segmentation of the NeoChord tool on the bi-plane ultrasound images. Specifically, we investigated the consistency, repeatability, and robustness of the calibration results as a function of fiducial localization. In our study; we have noted that the users tend to have a lot more discrepancy in the out-of-plane direction among themselves, likely due to the psychology of visual perception differences among users. In ultrasound reflection of the tool, the two tails of the partial arc often occur in the in-plane direction. Therefore, the user has two sources of information to estimate the centroid in the in-plane direction. Alternatively, the ultrasound reflection just represents the superior portion of the ellipse, and the lower part is missing. Therefore, users could have had difficulty estimating the centroid along the out-of-

plane direction with only a single source of information being available. This leads to greater uncertainty along the Y direction than X or Z.

The Mean±SD of the decomposed target errors associated with the user's segmentations that were compared against automatic segmentation, shows inconsistency in calibration accuracy for manual process (Table2.5). Although, few users could perform as well as the automatic segmentation, this was not the case for everyone. Also, manual segmentation could become even less precise in the OR, during surgery, because it depends on the user's level of concentration in that particular situation.

2.4   3D Ultrasound Calibration

In this section, we propose a real-time 3D ultrasound calibration technique which is derived based on the bi-plane calibration. This approach does not require scanning of a specialized phantom or any information from the 3D ultrasound. Instead, the high quality bi-plane images are used to solve for the 3D calibration.

The TEE 3D ultrasound is readily used for the positioning of the surgical tool at the target site in transapical MV repair surgery. Integration of this imaging mode into the navigational platform is tied to the calibration of 3D ultrasound with the tracking system. To date, different methods have been proposed for 3D calibration, which are mostly pre-operative and require a large number of acquisitions. Another limitation is the inability to estimate the correct speed-of-sound of a target medium in the previous methods. The solution to these problems is an 'online' 3D calibration during surgery. The TEE probe can alter the imaging mode from bi-plane to 3D by pressing a button. Since we could obtain the in-situ bi-plane calibration using the directed tool, this suggest the applicability of a similar approach to determine the 3D calibration. This indeed gives us an advantage of using the high resolution bi-plane images rather than the lower resolution real-time 3D ultrasound for scanning the tool. At the same time, by just one calibration process, both the bi-plane and 3D modes are calibrated with respect to the tracking system. It has been noted that the internal coordinate systems for the bi-plane and 3D ultrasound within the TEE probe are different, but are related through a fixed transformation. Therefore, exploring the relationship between these two coordinates enables us to obtain the 3D calibration based on the bi-plane calibration.

Particularly, in this study we have investigated the intended internal transform where the 3D calibration was obtained from the bi-plane calibration. Then, the achieved calibration was compared against the pointer-based real-time 3D calibration method, with different materials used as the tip.

2.4.1 Methods

Similar to the previous studies, the Philips iE33 ultrasound machine, equipped with the TEE probe (X7-2t), was used. The probe consists of a grid of 50 rows and 50 columns, creating a total of 2500 piezoelectric crystal elements on the surface of the probe. Individual elements are activated and generate an ultrasound beam that can be steered in both the azimuthal and elevational planes over 90° angle to cover the pyramidal scanning volume. The same elements can be controlled electronically and are partially activated to produce bi-plane ultrasound imaging mode. Indeed, since the same set of elements are used to create either of the two imaging modes, there must be a fixed relationship between the internal 3D and bi-plane coordinate systems.

The TEE probe provides different 3D modes namely, Live, Zoom, and Full volume. The Live and Zoom modes are real-time, whereas the Full volume mode is created based on an ECG gated (4-7 beats) technique; sub-volumes are stitched together and synchronized to one cardiac cycle. In terms of the volume size, Live 3D constructed ($60° \times 90° \times depth$), which is narrower in comparison to the Full volume ($90° \times 90° \times depth$). In most stages of the transapical MV repair procedure, real-time 3D modes are used for positioning tasks. The direct streaming of the real-time 3D ultrasound mode comprises 112×48×112 pixels, which at an imaging depth of 12 cm, corresponds to the 110×57×120 mm of physical space. Alternatively, Philips allows access to the digitally stored 3D volumes for offline analysis, via analytical software package, QLAB (Philips Medical System). The stored volume based on the software has 160×64×208 pixels for the same physical size in space. The validation and localization experiments for 3D calibration analysis were performed based on the stored volumes.

2.4.1.1 Validation of Intrinsic Transform

The intrinsic transform in this context is referred to as the internally fixed relationship between the bi-plane to the 3D ultrasound coordinate systems (Fig.2.27). The first step in determining the intrinsic transform is to find the relationship between the bi-plane and the position sen-
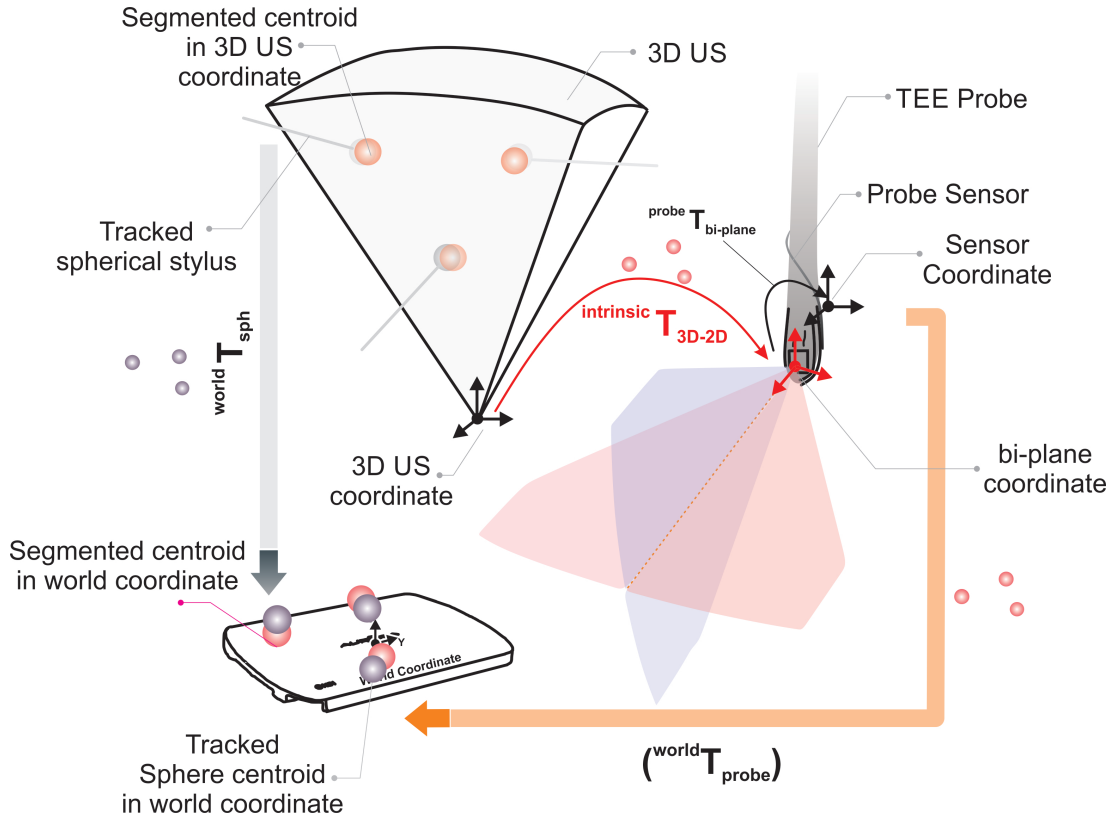
Figure 2.23: Intrinsic relationship between the bi-plane and 3D ultrasound coordinate systems.

sor's ($^{PS}T_{bi}$) coordinate system. This is achieved through our calibration approach, using the directed tool. Then, exploring the direct relationship between the 3D ultrasound and position sensor's coordinate system is necessary. This is accomplished through the point-to-point based calibration approach. An Aurora 6-DOF pointer (NDI Waterloo Canada), with the sharp tip and spherical object attached to it, was used for this purpose. The centre of the spherical tip is known within the tracking system by pivot calibration. The tip is scanned by the 3D ultrasound at different depths and orientations. In each acquisition, the tracking position of the tip and its corresponding 3D volume were stored simultaneously. Then, the centre of the spherical tips in different 3D ultrasound volumes was manually segmented ($^{US}P_{3D}$). The relationship between these two sets of data, solved through the point-to-point registration algorithm [39], represents the transformation relating the 3D ultrasound to the position sensor's coordinate system.

$$^{PS}P_{3D} \ = \ ^{PS}T_W \ ^WT_{Sty} \ P_{3D} \tag{2.17}$$

$$\text{FRE}^2 = \frac{1}{N} \sum_{i=1}^{N} \| R \, ^{US}P_i + t - \, ^{PS}P_i \|^2, \tag{2.18}$$

where $^{PS}P_{3D}$ is a set of N×3, tracking position of the tip in position sensor's coordinate system, and $^{US}P_{3D}$ is a set of N×3, fiducials being segmented from the 3D ultrasound. The rotation, R, is a 3×3 matrix and the translation, t, is a 3×1 vector. Note that, the scale parameters are corrected based on the scales obtained from the bi-plane calibration (detailed in next section). The $^{W}T_{sty}$ is a transformation of the pointer to the world coordinate, and $^{PS}T_{W}$ is the inverse transformation of the position sensor to the world coordinate. Also, in this experiment N=20 fiducials were used to perform the calibration. Finally, based on the obtained transforms, $^{PS}T_{bi}$ and $^{PS}T_{3D}$, we could determine the intrinsic transform, $^{3D}T_{bi}$, of the bi-plane to the 3D ultrasound coordinate as follows:

$$^{3D}T_{bi} = \, ^{3D}T_{PS} \, ^{PS}T_{bi} \tag{2.19}$$

2.4.1.2 Scale Correction in 3D Ultrasound

In computing the ($^{PS}T_{3D}$) transform, scale parameters were those not included with the rotation and translation parameters. In fact, the scales being used were what had already been provided by the manufacturer, having been corrected for the local speed-of-sound of a medium. The ratio of the estimated scales from bi-plane calibration and those provided by the manufacturer allows to correct for the scaling factors. For instance, in bi-plane calibration, the algorithm solves for the two scales of S_x and S_y (in- and out-of-plane scales), while the scales of in-plane directions, X and Z, are equivalent. At the same time, based on the caliper provided by the manufacturer, we can measure the scales in each direction. The percentage difference of the measured and estimated scale in each direction corresponds to the difference of the speed-of-sound of the target medium with what is manufacturer assumed, which is computed through Eq.2.20. The ratio of each axis, can be applied to the scale provided by the manufacturer for the 3D ultrasound in order to correct the scale, Eq.2.21.

$$\% \, S_{\text{diff}}^{\text{bi}} \; = \; \frac{S_{\text{estimated}} - S_{\text{measured}}}{S_{\text{measured}}} \times 100 \tag{2.20}$$

$$S_{\text{Corr}}^{\text{3D}} \; = \; (1 + \% S_{\text{diff}}^{\text{bi}}) \times S_{\text{measured}}^{\text{3D}} \tag{2.21}$$

2.4.1.3   Validation of Derived 3D Calibration

The derived 3D calibration was validated through a new set of 20 unique pointer's tip in 3D ultrasound, $P_i^{\text{3D}} = [P_1 \cdots P_{20}]$. The spherical tip of the pointer was scanned from different directions and depths in ultrasound volume. The centroid of the 3D ultrasound reflection of the spherical tip was manually segmented by the user. The derived 3D calibration consists of, bi-plane calibration obtained through our minimization algorithm following the intrinsic transform. The following equation describes the TRE measurement:

$$\text{TRE} = \frac{1}{500} \sum_{i=1}^{500} \frac{1}{20} \sum_{j=1}^{20} \| \, ^{\text{W}}T_{\text{PS}} \, ^{\text{PS}}T_{\text{bi}}^{i} \, ^{\text{bi}}T_{\text{3D}} \, P_{\text{3D}}^{j} \; - \; ^{\text{W}}T_{\text{sty}} \, P_{\text{sph}}^{j} \|^{2}, \tag{2.22}$$

where $^{\text{bi}}T_{\text{3D}}$ is the intrinsic transform and the points segmented from 3D ultrasound were converted to the physical space based on the corrected-scales measurements. There were 20 targets and 500 unique bi-plane calibrations used for every k sampled image of the main dataset (60 bi-plane images), $k \in [3 \cdots 20]$.

2.4.1.4   Qualitative Validation of Derived 3D Calibration

A visualization experiment was conducted to qualitatively assess the goodness of derived 3D ultrasound calibration. A table tennis ball was fixed within a magnetic field and the surface of the ball was digitized by the sharp tip of the stylus. Using the least-square approach, the centre of the ball was estimated within a world coordinate and the virtual model of the tracked ball was created based on the calculated radius. The calibrated real-time 3D TEE probe was clamped to keep it motionless within a controlled medium. The ball was scanned once by the bi-plane ultrasound and again scanned by 3D ultrasound at the same pose. This enabled us to fuse and visualize the overlay of 3D ultrasound volume, bi-plane image and the tracked table
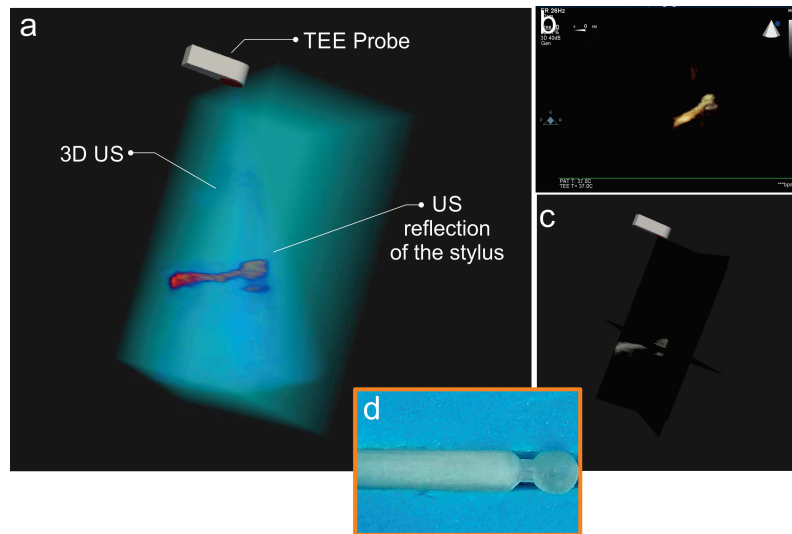
Figure 2.24: (a) 3D ultrasound appearance of the stylus's spherical tip. (b) screen-capture of the 3D ultrasound. (c) cross-sectional slices of 3D ultrasound. (d) 3D printed spherical tip

tennis ball in a common coordinate system.

The second qualitative experiment was performed based on the tracked NeoChord tool. The tool stayed stationary in a controlled medium and was scanned by the calibrated TEE probe in both the 3D and bi-plane modes from the same pose. Then, the virtual model of the tracked tool, calibrated real-time 3D ultrasound, and bi-plane image were fused into a common coordinate. The goodness of the overlaid tool with both of the imaging modes, demonstrated the accuracy of the system.

2.4.1.5 Pointer-based 3D Ultrasound Calibration

Our 'online' derived 3D ultrasound calibration is compared against the pointer-based 3D ultrasound calibration. In this experiment a point-to-point calibration approach between the two sets of points, one from 3D ultrasound and the other from tracking system, were performed. A tracked pointer with the sharp metallic tip was used. However, three different tip conditions were used in order to peruse their effect on the localization and the accuracy of the 3D calibration.

An Aurora 6-DOF pointer served as a tracked tool to perform the calibration. Two add-on
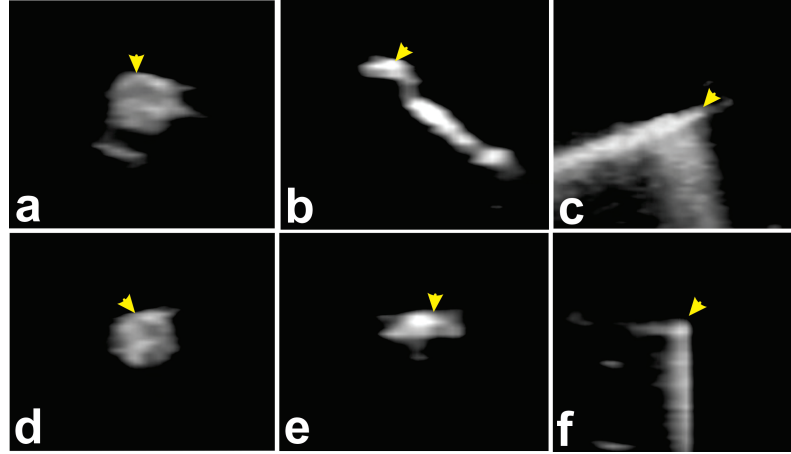
Figure 2.25: The cross-sectional slices from the 3D ultrasound reflection of the stylus's tip, made by different materials. The first row corresponds to the 'XZ-plane' of the 3D ultrasound volume and respectively, the second row 'YZ-plane' . (a,d) Represents the ultrasound reflection of the PVA-C-based spherical tip, (b,e) 3D-printed, and (c,f) the sharp metallic-tip.

custom-made spherical tips were designed to attach to the pointer's tip, one made of PVA-C and the other 3D printed (See Fig.2.24). And, two sets of calibrations were additionally derived based on these tip conditions. In each scenario, the tip was placed stationary so as to achieve the pivot calibration. The tracked tip was scanned by the calibrated 3D ultrasound, and its ultrasound reflection was manually segmented in each image acquisition, $^{US}P_{3D}$ (See Fig.2.25). The tracked positions, $^{W}T_{sty}$, of the pointer and their corresponding ultrasound positions were used to solve for the calibration transform through the point-to-point registration algorithm [39].

$$^{PS}P_{tip} = (^{W}T_{PS})^{-1} \, ^{W}T_{sty} \, P_{tip} \tag{2.23}$$

$$FRE^2 = \frac{1}{N} \sum_{i=1}^{N} \| (RS \, (^{US}P_{3D}^{i}) + t) - \, ^{PS}P_{tip}^{i} \|^2, \tag{2.24}$$

where R is the rotation matrix, S is the diagonal scale matrix, t is the translation vector, and N is the number of fiducials used in the calibration process. Note that, similar to the previous experiment, k fiducials were sampled from the main dataset of 20 fiducials and was repeated for 500 unique combinations ($k \in [3 \cdots 15]$). To evaluate the goodness of the derived 3D calibration, PR experiment was performed by using targets that were not involved in calibration process.

Table 2.6: Intrinsic transform between the bi-plane and 3D ultrasound imaging modes. The rotations are given in degree unit and translations are based on the slice number in 3D ultrasound volume.

	Rotation (deg.)	Translation (Slice No.)
X	90	80
Y	0	0
Z	180	59
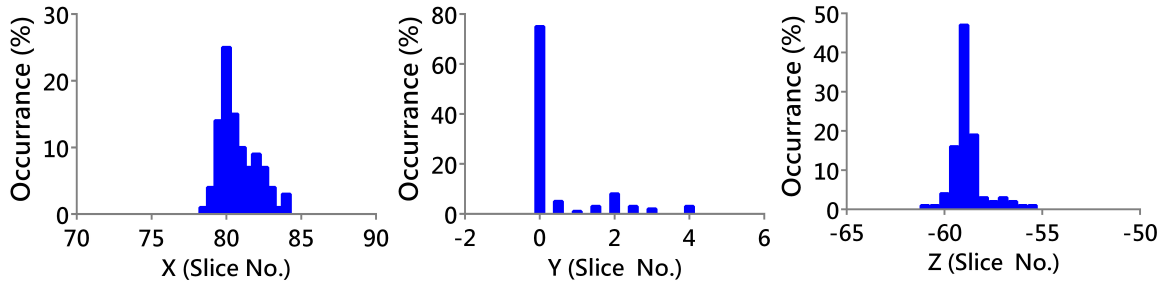
Figure 2.26: Occurrence of the translation parameters for intrinsic transform based on 500 different computations for the intrinsic transform.

2.4.2   Results

The parameters of the intrinsic transform between the bi-plane and 3D ultrasound are given in Table 2.6. The computation of the individual parameters obtained from Eq.2.19 were repeated for 500 unique bi-plane calibrations in order to confirm the intrinsic transform. The rotations are calculated in Euler angle with the rotation axes sequence of 'XYZ'. The translation parameters are provided as slice numbers within the 3D ultrasound coordinate system (see Fig.2.26). In addition, we have qualitatively demonstrated which slices from the 3D ultrasound volume correspond to the individual planes of the bi-plane ultrasound (see Fig.2.27). The 'plane 0' of the bi-plane ultrasound should match a slice from 'YZ-plane' of the 3D ultrasound coordinate system. Interestingly, we noted that the 59th slice of the 'YZ-plane' corresponds to the 'plane 0' of the bi-plane ultrasound, rather than the last slice (64th) in the same direction, Fig.2.27a, b. Also, as expected, the middle slice of the 'YZ-plane' corresponded to the 'plane 90' of the
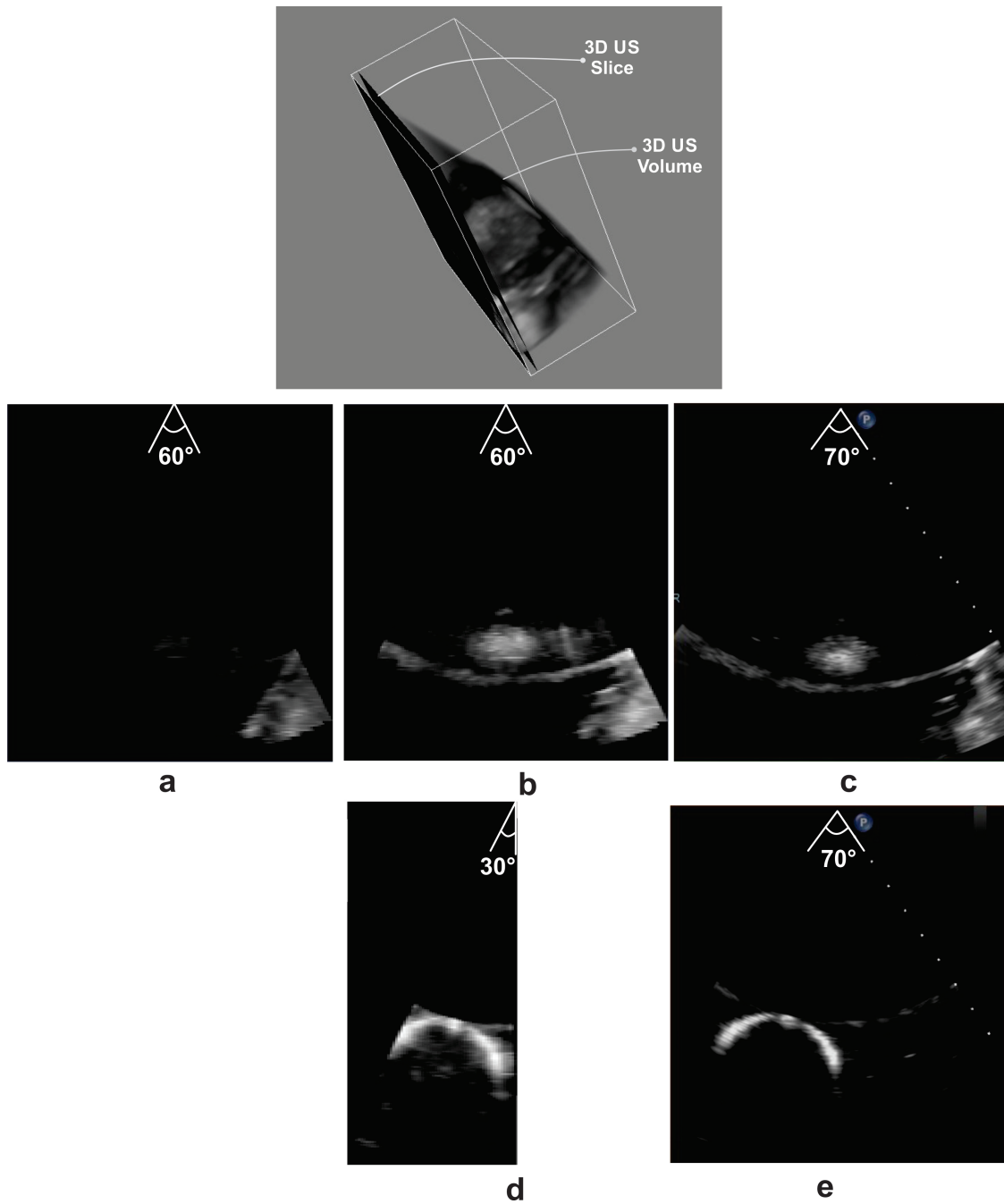
Figure 2.27: 3D ultrasound volume and the extracted slices that correspond to the cross-sectional bi-plane ultrasound image. The 3D ultrasound volume consisted of 64 slices in the 'xz plane'and 160 slices in the 'yz plane'. (a) 64th and (b) 59th slice of the 3D ultrasound volume in the 'xz plane' direction. (c) plane 0 of the bi-plane ultrasound image. (d) 80th slice from 'yz plane'. (e) plane 90 of the bi-plane ultrasound image.

bi-plane ultrasound, Fig.2.27e. The width of the 'YZ-plane' in 3D ultrasound is half of the 'plane 90' in bi-plane image, since the volume of the real-time 3D ultrasound is smaller in size than the full volume 3D mode. Also, the higher spatial resolution of the bi-plane image in comparison to the 3D ultrasound is evident in fine details of the ultrasound reflection of the ball surface.

Three different tip materials were used to be scanned by the 3D ultrasound so as to explore their effect on the fiducial localization. The distribution of the tip locations over the 3D ultrasound volume were shown in Fig.2.28. A dataset containing 27 fiducial points based on the PVA-C-tip, 20 fiducial points based on the 3D printed-tip, and 17 fiducial points based on the sharp-metallic-tip was used. The fiducials, in each experiment, were carefully collected such that to cover the entire 3D volume. The stability, repeatability, and accuracy of the 3D ultrasound calibrations were evaluated through the Monte Carlo experiment. A set of k samples were randomly chosen from the total fiducials to solve for the calibration transform ($k \in [3 \cdots 15]$). For every k, 500 unique combinations of the fiducials were selected. The accuracy of the pointer-based 3D ultrasound calibrations, under different tip conditions, as a function of the number of fiducials, was shown in Fig.2.29a. Similar results were shown in Fig.2.29b for the derived 3D calibration. The trueness of different calibrations were compared against each other using Tukey multiple comparison test with, p-value < 0.05 (see Fig.2.29c). The decomposed error of the calibration result for each individual axes were illustrated in Fig.2.29d, e, f. The summary of the trueness and precision for the different calibration methods is given in Table 2.7. The qualitative validation results of our derived-3D ultrasound calibration are demonstrated in Fig.2.30 and Fig.2.31.

2.4.3 Discussion

This study extends the 'in-situ bi-plane' ultrasound calibration to the 'online 3D' ultrasound calibration. The proposed approach is composed of two distinct calibrations, the bi-plane and the intrinsic. The bi-plane transform, relates the TEE bi-plane coordinate to the magnetic track-
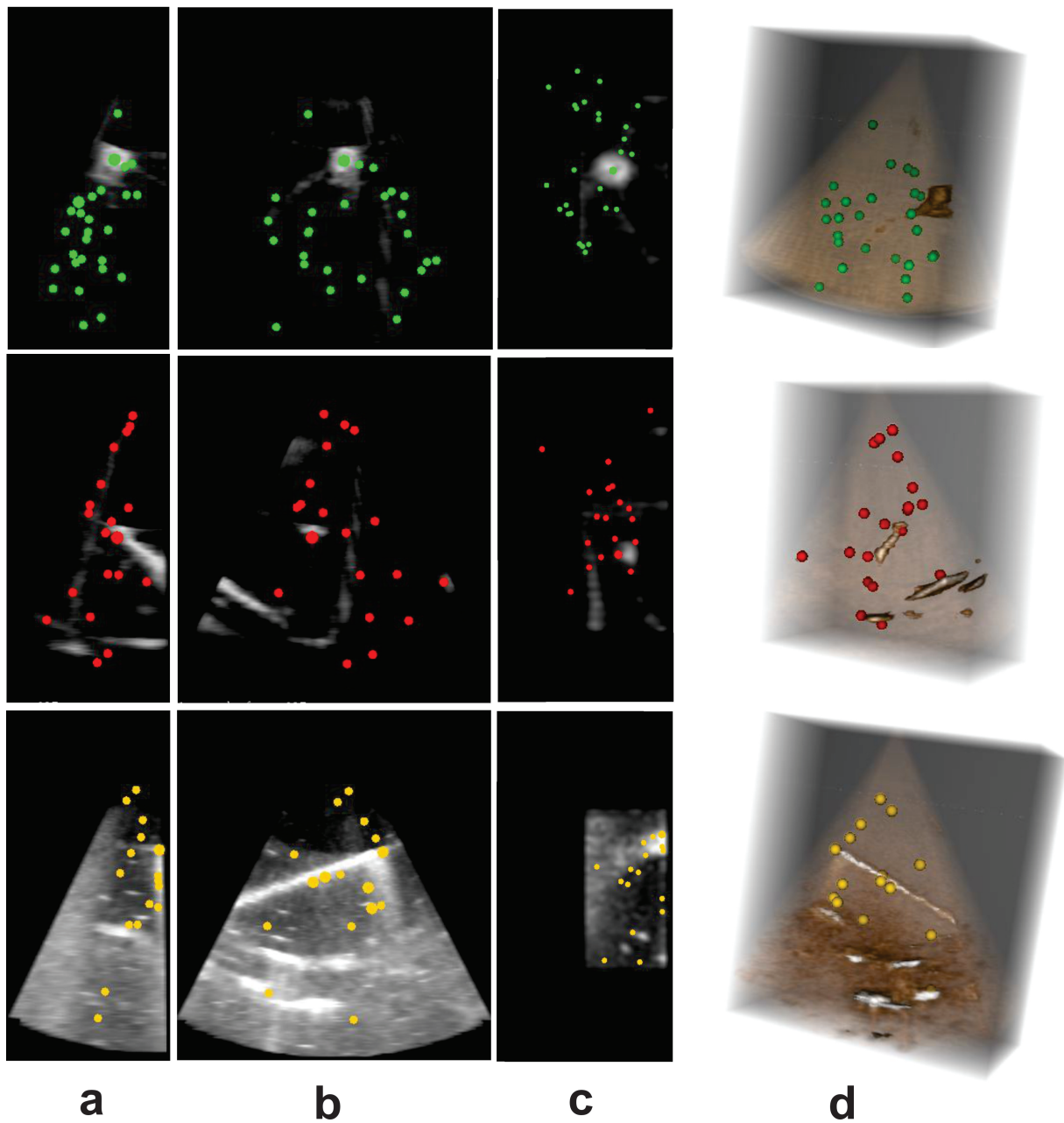
Figure 2.28: Distribution of the fiducials within 3-D ultrasound volume. (a) demonstrates the 'yz plane' (b) 'xz plane' and (c) 'xy plane' of the (d) 3-D ultrasound volume. The colored fiducials are projected on 2D cross-sectional planes of the 3-D ultrasound volume. The green, red and yellow fiducials correspond to the PVA, 3D printed and metallic tip experiments, respectively.
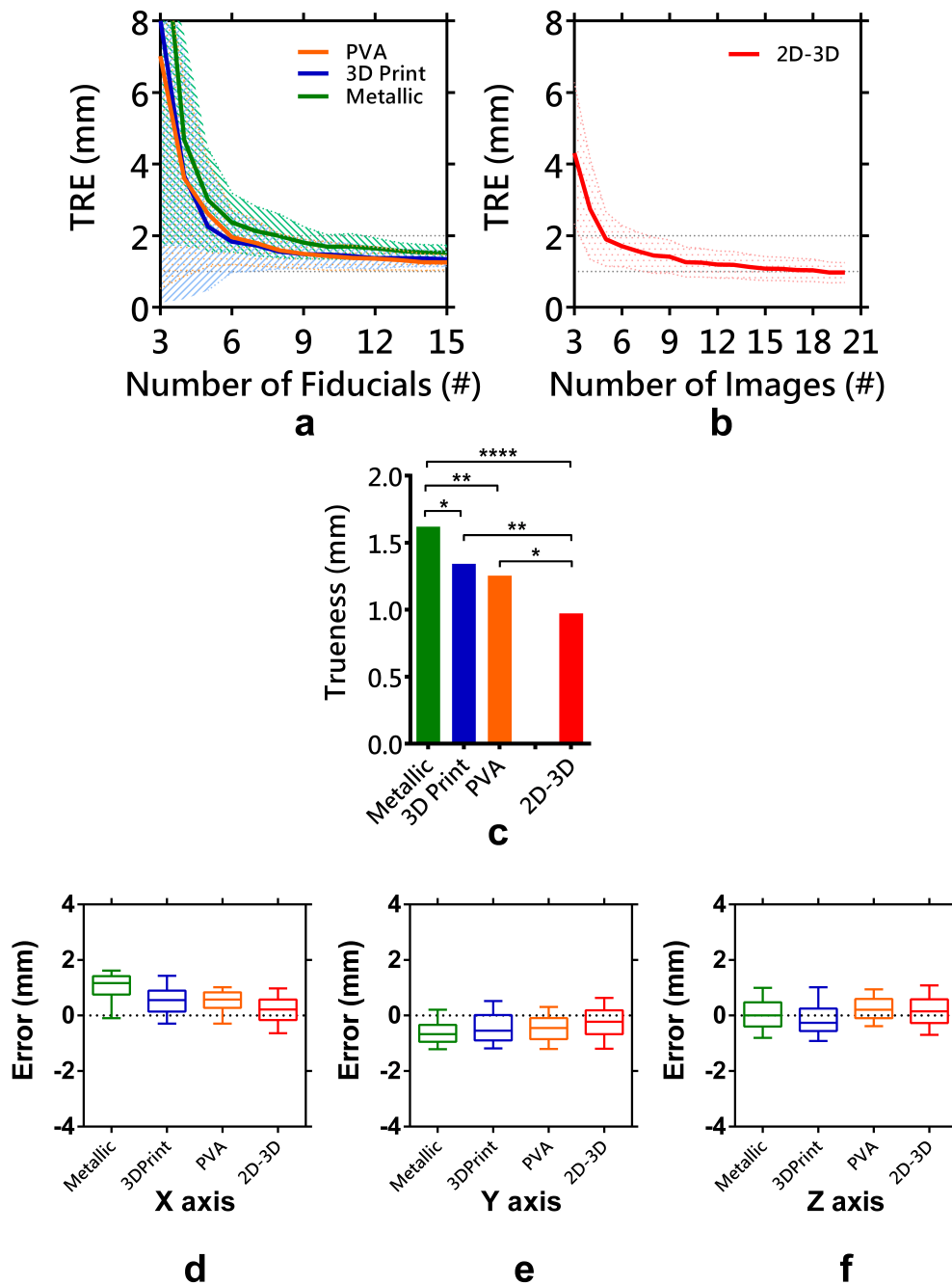
Figure 2.29: The graph (a) demonstrates the accuracy of the 3-D calibrations for every individual tip condition with respect to the number of fiducials used in the computation process. Respectively (b) shows the 3-D calibration accuracy which was derived from bi-plane calibrations, reported based on number of bi-plane image acquisitions. (c) Side by side comparison of the trueness, for each of the 4 calibration approaches. (d, e, f) box-plot of the decomposed errors in each of the x-y-z directions. Middle line indicates the median, boxes interquartile range, notches 95% confidence intervals, whiskers data ranges. * P < 0.05, ** P < 0.01, **** P < 0.0001
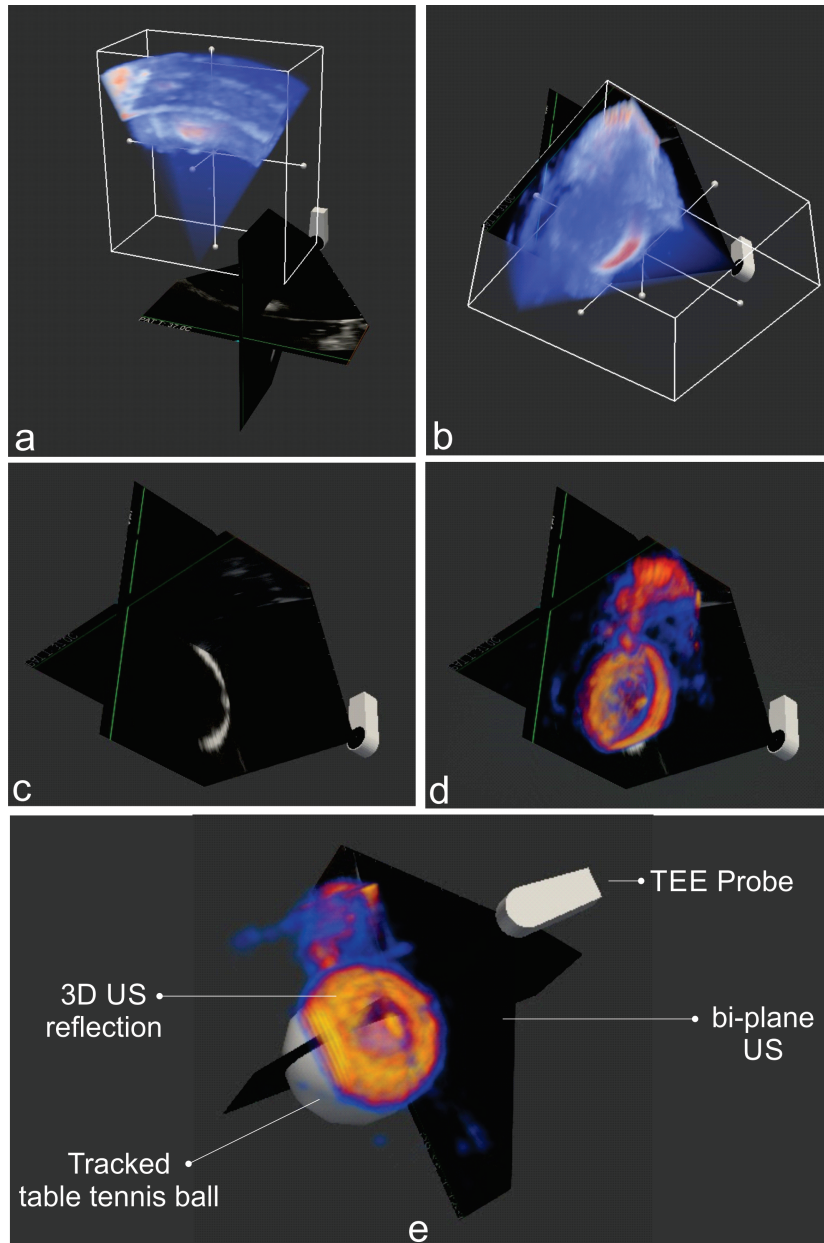
Figure 2.30: Qualitative validation using a tracked Table-Tennis ball. (a) volume rendered 3-D ultrasound and bi-plane coordinates within TEE local coordinate system. (b) the overlay of the two coordinates after applying intrinsic transform between the 3-D and bi-plane coordinates. (c) 2D bi-plane ultrasound reflection of the ball surface. (d) 3-D ultrasound reflection of the ball by adjusting the color mapping data which overlays with its cross-sectional ultrasound reflection. (e) tracked table tennis ball, calibrated bi-plane ultrasound image and calibrated 3-D ultrasound volume are visualized in a common coordinate system.
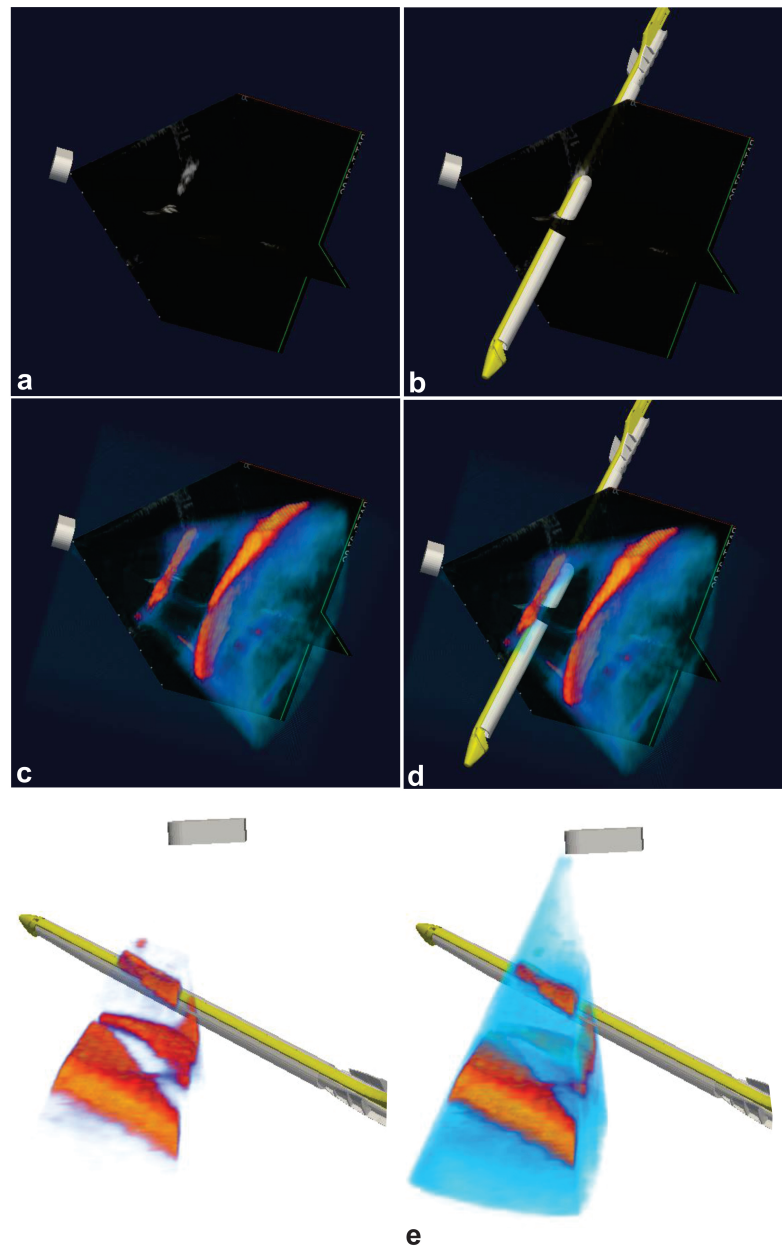
Figure 2.31: Qualitative validation using the NeoChord tool. (a) bi-plane ultrasound reflection of the tool. (b) overlay of the tracked tool's virtual model with bi-plane ultrasound image. (c) 3-D ultrasound volume fused with bi-plane ultrasound image. (d) overlay of the both calibrated 3-D and bi-plane imaging modes with surgical tool in a common coordinate. (e) calibrated 3-D ultrasound volume and the reflection of the intersecting tool.

	Mean TRE (mm)	Std. Dev. (mm)	N	Repetition
Metallic	1.55	0.21	15	500
3D Print	1.34	0.23	15	500
PVA	1.25	0.22	15	500
Derived 3D	**1.01**	**0.29**	15	500

Table 2.7: Summary of calibration accuracy result. N is the number of fiducials for point based methods/bi-plane acquisition for derived-3D ultrasound calibration.

ing sensor's coordinate, while the intrinsic transform relates the 3D to the bi-plane ultrasound coordinate. In this regard, scanning the tracked surgical tool by the bi-plane ultrasound allows 3D calibration during surgery. Since the bi-plane acquisitions are obtained from the same target medium, where the 3D ultrasound volumes are acquired, the scale correction in bi-plane calibration can be applied to the scales in 3D ultrasound calibration. This approach, therefore, compensates for the correct scaling factors of the target medium in 3D ultrasound as well.

The key element in our approach is in fact the intrinsic transform between the 3D and bi-plane coordinates. The rotation parameters for this transform were achieved through the highest frequency of occurrence at 90 and 180 degrees in the X and Z directions. Qualitatively, this rotation is obvious when the stored 3D ultrasound volume was rotated respectively onto the bi-plane ultrasound. Then after applying the translation parameters, the origin of the sector 3D ultrasound volume corresponds to the origin of the bi-plane ultrasound image. The translations in the directions of xy- and yz-slice of the 3D ultrasound volume occurs as expected. However, the challenging translation parameter was in the XZ-slice direction in the 3D ultrasound volume. The 59$^{\text{th}}$ slice received the highest score of occurrence among other slices in this direction, therefore it corresponded to the plane 0 of the bi-plane ultrasound image. Note that, determining the correct slices of the 3D ultrasound that corresponds to the bi-plane ultrasound individual planes is quite important, since it could directly affect the accuracy of the 3D calibration, which is in fact due to the large voxel sizes in the 3D ultrasound volume (e.g. 0.89 mm).

The slice numbers provided in this study corresponded to the stored 3D ultrasound volume

(from QLab software), and knowing the physical sizes of the voxels enables us to identify the origin in physical space within the 3D volume. Nevertheless, the streaming 3D ultrasound is the same as the stored 3D ultrasound with the only difference of the voxel sizes. Therefore, the location of the origin in streaming 3D ultrasound is obvious based on the origin in stored 3D ultrasound.

The PR validation experiment demonstrated the overall inaccuracies in the calibration which includes parameter estimation in both the bi-plane and intrinsic calibrations, segmentation of the tool in bi-plane ultrasound, target localization in the 3D ultrasound, and the tracking uncertainties. The PR accuracy of our proposed 3D calibration method achieved 1.01±0.29 mm using 15 bi-plane images and 0.97±0.27 mm by 20 bi-plane images. In the derived-3D calibration method, the bi-plane images are those used for bi-plane calibration, and therefore no extra 3D ultrasound acquisitions were required to achieve the 3D calibration at the same imaging depth.

The accuracy of our derived-3D calibration approach outperformed the pointer/needle-based method [48]. In particular, our method was significantly superior in comparison to the different tip conditions: PVA-C tip (p-value < 0.05), 3D-printed tip (p-value < 0.01), and metallic-tip (p-value < 0.0001). Among different tip conditions, PVA-C-tip outperformed the other two, because of the characteristics of the PVA-C material that make a full 3D spherical ultrasound reflection. Thus, localizing the centre of full sphere in 3D ultrasound is more accurate than in the proximal surface, 3D reflection of the 3D-printed-tip, or in the 3D reflection of the metallic-tip. Therefore, the PVA-C-tip leads to improved FLE in comparison to the other tip material. Note that using PVA-C material as a tip requires extra caution while performing the pivot calibration. This is due to the lower stiffness of the PVA-C material compared to the 3D-printed and the metallic-tip. The sharp metallic-tip was the least accurate amongst all of the tested tips, due to the large artifact of the tip in 3D ultrasound at different angles. Therefore, the variability of the trueness between the calibration methods is mainly due to the FLE effect. In addition, the bi-plane images have higher resolution than the 3D ultrasound (Pixel size of 0.24

mm vs. Voxel size of 0.9 mm). Therefore, in derived-3D calibration, the ultrasound reflection of an object in bi-plane ultrasound is more accurately interpreted by visual inspection, leading to more accurate fiducial localization.

Summary

In this chapter, we have demonstrated that the directed-surgical tool approach successfully achieved bi-plane calibration in a simulated surgical environment. This was obtained in a condition where the LV phantom was scanned from the trans-gastric view, while a limited range of motion was available. The system was successful in recovering the 'true' scaling factors, and achieving the sub-millimeter accuracy during the process. This implies that the calibration approach has the potential to estimate the correct speed-of-sound at the target site of surgery, and thus to obtain the desirable accuracy.

Furthermore, we have demonstrated that acquiring twice as many fiducials from the bi-plane images in calibration process entails the requirement of fewer acquisitions and, in turn, increased accuracy compared to using single-plane images. It is revealing to echocardiographer that it is highly beneficial to have both planes of the bi-plane ultrasound intersect with the tool throughout the scanning process.

Our project have shown that automatic segmentation of the tool reflection in ultrasound causes the calibration to be more stable and accurate compared to manual segmentation. This is mainly due to the fact that the ultrasound reflection of the tool appears as a partial arc, rather than a full ellipse, and causes discrepancy in identifying the centroid among different users.

Lastly, we have demonstrated that 3D TEE ultrasound calibration can be derived based on the bi-plane calibration followed by the intrinsic calibration between the 3D and bi-plane coordinates. This suggests that during surgery we are only required to obtain the bi-plane images to compute both the bi-plane and the 3D ultrasound calibrations, thus achieving the sub-millimeter accuracy.

Chapter 3

Conclusion and Future Direction

This thesis proposes the directed surgical tool technique that has the potential to perform the ultrasound calibration 'in-situ' during minimally-invasive beating-heart surgery. The desired sub-millimeter accuracy was achieved in a simulated environment, even though the available space for manipulating the tool and the TEE probe was limited. The main goal was to demonstrate successful compensation of the error caused by the speed-of-sound in the medium at the target site of surgery, since this parameter can vary among different patients and different organs of the body. This method enables calibration of a magnetically-tracked probe to be achieved in an operating room environment. The accuracy of our approach was determined through a series of validation techniques: PR, VR, distance measurement. The time required to perform the calibration was about 60-90 seconds which has minimal impact on the actual surgical procedure.

The proposed bi-plane ultrasound imaging of the directed tool during calibration process shows significant improvement on the calibration accuracy, when compared with single-plane imaging. This approach provides twice as many data samples, in a similar acquisition time as the single-plane approach, to solve the calibration transform. The use of the additional plane in the bi-plane technique improved the estimation of the both rotation and scaling parameters.

In terms of segmenting the ultrasound reflection of the directed tool on ultrasound images,

91

automatic segmentation showed significantly improved results compared to the manual segmentation, achieving relatively higher stability and repeatability.

We also proposed an 'online' 3D ultrasound calibration that employs high-quality bi-plane images, rather than low resolution 3D ultrasound volume, during surgery. The derived-3D calibration is based on bi-plane calibration followed by the intrinsic transform between the bi-plane and the 3D coordinate systems. This derived-3D calibration demonstrates significantly enhanced results compared to the pointer-based 3D calibration method. In addition, amongst pointer-based 3D calibrations, a pointer with PVA-C-tip had the best calibration accuracy since its 3D ultrasound reflection appeared as a full sphere compared to the mere proximal surface reflection of the 3D-printed-tip. This, ultimately resulted in a more accurate fiducial localization leading to a more accurate calibration result.

3.1 Future Direction

3.1.1 Animal Study

The main focus of this thesis was to introduce an in-situ ultrasound calibration paradigm that could be performed during trans-apical mitral valve repair surgery. In this regard, we have created a simulated surgical scene in a laboratory environment, where the LV phantom, TEE probe, and surgical tool were placed in a water medium simulating the actual scenario. Performing in such an environment enabled us to assess the feasibility and robustness of our approach while the tool was being scanned from trans-gastric view with a limited range of movement.

That said the next logical step is to integrate our calibration technique into an AR guided surgical workflow and evaluate it in an animal study.

3.1.2 Online Validation

In terms of validation, we have successfully demonstrated the accuracy of the calibration in the laboratory setup through PR, VR, scale, and accuracy measurements. However, these evaluation methods were performed using the additional devices (table tennis ball, parallel line phantom, etc.) that are not practically applicable inside the patients body. They are, in face, used to determine the quality of the calibration technique itself, in a laboratory environment simulating the clinical situation. The only so-called instant validation approach is the qualitative visualization of the overlay between the virtual model of the device corresponding and its ultrasound reflection.

The next step would be to design an online assessment criteria to obtain the accuracy of the calibration during surgery. For instance, any a priori known feature at the target site, such as the tip or shape of the surgical tool, could be used as a validation element. While localizing the tip during surgery might be a challenging task, using the bi-plane ultrasound images could help to simplify this by simultaneous identification along the length. Alternatively, the known distance between the jaws and the absolute tip of the tool provides distance measurement criteria to assess the recovered scale parameters. Anatomical features might also be used as targets. However, this does not prove to be a viable option since the procedure is performed in a beating heart environment, and therefore tracking those targets could introduce greater error than the calibration itself.

3.1.3 Automatic Segmentation

At present, our automatic segmentation algorithm requires the user to determine an approximate ROI on the bi-plane ultrasound image. Thus the system automatically segments the reflection of the tool followed by the centroid identification of the estimated ellipse. Further improvement can be achieved by applying an adapted Kalman Filter or similar techniques to automatically determine the ROI in an image. This could significantly reduce the data acquisition time, as well as user dependency.

3.1.4   Visualization

In terms of 3D ultrasound, currently we are using a direct volume rendering with 1D transfer function to perform the visualization in real-time. However, using a 2D transfer function [47] by incorporating another parameter, such as the depth or gradient, may enhance the 3D ultrasound visualization, potentially providing finer details of the surface boundaries for the tool and the tissue.

Bibliography

[1] Nadine Abi-Jaoudeh, Neil Glossop, Michael Dake, William F Pritchard, Alberto Chiesa, Matthew R Dreher, Thomas Tang, John W Karanian, and Bradford J Wood. Electromagnetic navigation for thoracic aortic stent-graft deployment: a pilot study in swine. *Journal of vascular and interventional radiology*, 21(6):888–895, 2010.

[2] Pietro Bajona, William E Katz, Richard C Daly, Kenton J Zehr, and Giovanni Speziali. Beating-heart, off-pump mitral valve repair by implantation of artificial chordae tendineae: an acute in vivo animal study. *The Journal of thoracic and cardiovascular surgery*, 137(1):188–193, 2009.

[3] Filip Banovac, Jonathan Tang, Sheng Xu, David Lindisch, Ho Young Chung, Elliot B Levy, Thomas Chang, Michael F McCullough, Ziv Yaniv, Bradford J Wood, et al. Precision targeting of liver lesions using a novel electromagnetic navigation device in physiologic phantom and swine. *Medical physics*, 32(8):2698–2705, 2005.

[4] Christoph Bergmeir, Mathias Seitel, Christian Frank, R De Simone, H-P Meinzer, and Ivo Wolf. Comparing calibration approaches for 3d ultrasound probes. *International journal of computer assisted radiology and surgery*, 4(2):203–213, 2009.

[5] Jane M Blackall, Daniel Rueckert, Calvin R Maurer Jr, Graeme P Penney, Derek LG Hill, and David J Hawkes. An image registration approach to automated calibration for freehand 3d ultrasound. In *Medical Image Computing and Computer-Assisted Intervention– MICCAI 2000*, pages 462–471. Springer, 2000.

[6] Emad M. Boctor, Michael A. Choti, Everette C. Burdette, and Robert J. Webster Iii. Three-dimensional ultrasound-guided robotic needle placement: an experimental evaluation. *The international journal of medical robotics + computer assisted surgery: MRCAS*, 4(2):180–191, June 2008.

[7] Lionel G Bouchet, Sanford L Meeks, Gordon Goodchild, Francis J Bova, John M Buatti, and William A Friedman. Calibration of three-dimensional ultrasound images for image-guided radiation therapy. *Physics in Medicine and Biology*, 46(2):559, 2001.

[8] H. Brandl, A. Gritzky, and M. Haizinger. 3d ultrasound: A dedicated system. *European Radiology*, 9(3):S331–S333, November 1999.

[9] Russell A Brown. A stereotactic head frame for use with ct body scanners. *Investigative radiology*, 14(4):300–304, 1979.

[10] A Carpentier, D Loulmet, E Le Bret, B Haugades, P Dassier, and P Guibourt. [open heart operation under videosurgery and minithoracotomy. first case (mitral valvuloplasty) operated with success]. *Comptes rendus de l'Academie des sciences. Serie III, Sciences de la vie*, 319(3):219–223, 1996.

[11] Jonathan Carr. Surface reconstruction in 3d medical imaging. 1996.

[12] Elvis CS Chen, A Jonathan McLeod, Uditha L Jayarathne, and Terry M Peters. Solving for free-hand and real-time 3d ultrasound calibration with anisotropic orthogonal procrustes analysis. In *SPIE Medical Imaging*, pages 90361Z–90361Z. International Society for Optics and Photonics, 2014.

[13] Thomas Kuiran Chen, Randy E Ellis, and Purang Abolmaesumi. Improvement of free-hand ultrasound calibration accuracy using the elevation beamwidth profile. *Ultrasound in medicine & biology*, 37(8):1314–1326, 2011.

[14] Kuan-Ming Chiu. Minimally invasive cardiac surgery. *Formosan Journal of Surgery*, 46(6):183–188, 2013.

[15] Lawrence H Cohn. Fifty years of open-heart surgery. *Circulation*, 107(17):2168–2170, 2003.

[16] Andrea Colli, Erica Manzan, Fabio Zucchetta Fabio, Cristiano Sarais, Demetrio Pittarello, Giovanni Speziali, and Gino Gerosa. Tee-guided transapical beating-heart neochord implantation in mitral regurgitation. *JACC: Cardiovascular Imaging*, 7(3):322–323, 2014.

[17] Roch M Comeau, Aaron Fenster, and Terence M Peters. Integrated mr and ultrasound imaging for improved image guidance in neurosurgery. In *Medical Imaging'98*, pages 747–754. International Society for Optics and Photonics, 1998.

[18] Erik Cuevas, Mauricio González, Daniel Zaldívar, and Marco Pérez-Cisneros. Multi-ellipses detection on images inspired by collective animal behavior. *Neural Computing and Applications*, 24(5):1019–1033, 2014.

[19] DR Dance, S Christofides, ADA Maidment, ID McLean, and KH Ng. Diagnostic radiology physics: A handbook for teachers and students. endorsed by: American association of physicists in medicine, asia-oceania federation of organizations for medical physics, european federation of organisations for medical physics. 2014.

[20] Pedro J. del Nido. Minimal Incision Congenital Cardiac Surgery. *Seminars in Thoracic and Cardiovascular Surgery*, 19(4):319–324, 2007.

[21] Paul R Detmer, Gerard Bashein, Timothy Hodges, Kirk W Beach, Eric P Filer, David H Burns, and D Eugene Strandness. 3d ultrasonic image feature localization based on magnetic scanhead tracking: in vitro calibration and validation. *Ultrasound in medicine & biology*, 20(9):923–936, 1994.

[22] Francis A Duck. *Physical properties of tissues: a comprehensive reference book*. Academic press, 2013.

[23] Jörg Ender and Sophia Sgouropoulou. Value of transesophageal echocardiography (tee) guidance in minimally invasive mitral valve surgery. *Annals of cardiothoracic surgery*, 2(6):796, 2013.

[24] Ted Feldman, Elyse Foster, Mansoor Qureshi, Brian Whisenant, John Williams, Donald Glower, and Laura Mauri. TCT-788 The EVEREST II Randomized Controlled Trial (RCT): Three Year Outcomes. *Journal of the American College of Cardiology*, 60(17_S), October 2012.

[25] Aaron Fenster, Jeff Bax, Hamid Neshat, Derek Cool, Nirmal Kakani, and Cesare Romagnoli. 3d ultrasound imaging in image-guided intervention. In *Engineering in Medicine and Biology Society (EMBC), 2014 36th Annual International Conference of the IEEE*, pages 6151–6154. IEEE, 2014.

[26] Edward A. Fisher, Jeffrey A. Stahl, Jacqueline H. Budd, and Martin E. Goldman. Transesophageal echocardiography: Procedures and clinical application. *Journal of the American College of Cardiology*, 18(5):1333–1348, November 1991.

[27] J Michael Fitzpatrick. Fiducial registration error and target registration error are uncorrelated. In *SPIE Medical Imaging*, pages 726102–726102. International Society for Optics and Photonics, 2009.

[28] J Michael Fitzpatrick, Jay B West, and Calvin R Maurer Jr. Predicting error in rigid-body point-based registration. *Medical Imaging, IEEE Transactions on*, 17(5):694–702, 1998.

[29] JM Fitzpatrick. The role of registration in accurate surgical guidance. *Proceedings of the Institution of Mechanical Engineers, Part H: Journal of Engineering in Medicine*, 224(5):607–622, 2010.

[30] L. Frazin, J. V. Talano, L. Stephanides, H. S. Loeb, L. Kopel, and R. M. Gunnar. Esophageal echocardiography. *Circulation*, 54(1):102–108, July 1976.

[31] Lisa A. Freed, Daniel Levy, Robert A. Levine, Martin G. Larson, Jane C. Evans, Deborah L. Fuller, Birgitta Lehman, and Emelia J. Benjamin. Prevalence and Clinical Outcome of Mitral-Valve Prolapse. *New England Journal of Medicine*, 341(1):1–7, July 1999.

[32] Andrew Gee, Richard Prager, Graham Treece, and Laurence Berman. Engineering a freehand 3d ultrasound system. *Pattern Recognition Letters*, 24(45):757–777, February 2003.

[33] Andrew Gee, Richard Prager, Graham Treece, and Laurence Berman. Engineering a freehand 3d ultrasound system. *Pattern Recognition Letters*, 24(4):757–777, 2003.

[34] Andrew H Gee, Neil E Houghton, Graham M Treece, and Richard W Prager. A mechanical instrument for 3d ultrasound probe calibration. *Ultrasound in medicine & biology*, 31(4):505–518, 2005.

[35] Ingmar Gergel, Jan Hering, Ralf Tetzlaff, Hans-Peter Meinzer, and Ingmar Wegner. An electromagnetic navigation system for transbronchial interventions with a novel approach to respiratory motion compensation. *Medical physics*, 38(12):6742–6753, 2011.

[36] Xiaoyu Guo, Alexis Cheng, Haichong K Zhang, Hyun-Jae Kang, Ralph Etienne-Cummings, and Emad M Boctor. Active echo: a new paradigm for ultrasound calibration. In *Medical Image Computing and Computer-Assisted Intervention–MICCAI 2014*, pages 397–404. Springer, 2014.

[37] Leland H. Hanowell, John T. Anderson, Eric J. Kraut, and Jeffrey D. Bear. Transesophageal echocardiography in the perioperative assessment of intravascular volume. *Seminars in Anesthesia, Perioperative Medicine and Pain*, 17(3):252–266, September 1998.

[38] David M Holzhey, William Shi, Michael A Borger, Joerg Seeburger, Jens Garbade, Bettina Pfannmüller, and Friedrich W Mohr. Minimally invasive versus sternotomy approach for mitral valve surgery in patients greater than 70 years old: a propensity-matched comparison. *The Annals of thoracic surgery*, 91(2):401–405, 2011.

[39] Berthold KP Horn. Closed-form solution of absolute orientation using unit quaternions. *JOSA A*, 4(4):629–642, 1987.

[40] Po-Wei Hsu, Richard W Prager, Andrew H Gee, and Graham M Treece. Rapid, easy and reliable calibration for freehand 3d ultrasound. *Ultrasound in medicine & biology*, 32(6):823–835, 2006.

[41] Po-Wei Hsu, Richard W. Prager, Andrew H. Gee, and Graham M. Treece. Real-time freehand 3d ultrasound calibration. *Ultrasound in Medicine & Biology*, 34(2):239–251, February 2008.

[42] Po-Wei Hsu, Richard W Prager, Andrew H Gee, and Graham M Treece. *Freehand 3D ultrasound calibration: A review*. Springer, 2009.

[43] Po-Wei Hsu, Graham M Treece, Richard W Prager, Neil E Houghton, and Andrew H Gee. Comparison of freehand 3-d ultrasound calibration techniques using a stylus. *Ultrasound in medicine & biology*, 34(10):1610–1621, 2008.

[44] G. Huemer, N. Kolev, and M. Zimpfer. Trans-oesophageal echocardiographic assessment of left ventricular systolic function: the anaesthesiologist's view. *European Journal of Anaesthesiology*, 11(6):437–441, November 1994.

[45] Judy Hung, Roberto Lang, Frank Flachskampf, Stanton K. Shernan, Marti L. McCulloch, David B. Adams, James Thomas, Mani Vannan, and Thomas Ryan. 3d Echocardiography: A Review of the Current Status and Future Directions. *Journal of the American Society of Echocardiography*, 20(3):213–233, March 2007.

[46] Ali Khamene and Frank Sauer. A novel phantom-less spatial and temporal ultrasound calibration method. In *Medical Image Computing and Computer-Assisted Intervention–MICCAI 2005*, pages 65–72. Springer, 2005.

[47] Joe Kniss, Gordon Kindlmann, and Charles Hansen. Multidimensional transfer functions for interactive volume rendering. *Visualization and Computer Graphics, IEEE Transactions on*, 8(3):270–285, 2002.

[48] Andrew Lang, Ameet Jain, and Vijay Parthasarathy. *Calibration of EM sensors for spatial tracking of 3D ultrasound probes*. INTECH Open Access Publisher, 2012.

[49] Thomas Lange and Sebastian Eulenstein. Calibration of swept-volume 3-d ultrasound. *MIUA Proc*, 99(3):29–32, 2002.

[50] Violet F Leavers. The dynamic generalized hough transform: its relationship to the probabilistic hough transforms and an application to the concurrent detection of circles and ellipses. *CVGIP: Image understanding*, 56(3):381–398, 1992.

[51] Daniel F Leotta. An efficient calibration method for freehand 3-d ultrasound imaging systems. *Ultrasound in medicine & biology*, 30(7):999–1008, 2004.

[52] Daniel F Leotta, Paul R Detmer, and Roy W Martin. Performance of a miniature magnetic position sensor for three-dimensional ultrasound imaging. *Ultrasound in medicine & biology*, 23(4):597–609, 1997.

[53] Cristian Linte, James White, Roy Eagleson, Gérard M Guiraudon, Terry M Peters, et al. Virtual and augmented medical imaging environments: enabling technology for minimally invasive cardiac interventional guidance. *Biomedical Engineering, IEEE Reviews in*, 3:25–47, 2010.

[54] Y. Loubieres, A. Vieillard-Baron, A. Beauchet, T. Fourme, B. Page, and F. Jardin. Echocardiographic evaluation of left ventricular function in critically ill patients: dynamic loading challenge using medical antishock trousers. *Chest*, 118(6):1718–1723, December 2000.

[55] Wei Lu and Jinglu Tan. Detection of incomplete ellipse in images with strong noise by iterative randomized hough transform (irht). *Pattern Recognition*, 41(4):1268–1279, 2008.

[56] Andrew Maslow and AC Perrino. Principles and technology of two-dimensional echocardiography. *A Practical Approach to Transesophageal Echocardiography*, 2:3–23, 2008.

[57] T Douglas Mast. Empirical relationships between acoustic parameters in human soft tissues. *Acoustics Research Letters Online*, 1(2):37–42, 2000.

[58] M. Matsumoto, Y. Oka, J. Strom, W. Frishman, A. Kadish, R. M. Becker, R. W. Frater, and E. H. Sonnenblick. Application of transesophageal echocardiography to continuous intraoperative monitoring of left ventricular performance. *The American Journal of Cardiology*, 46(1):95–105, July 1980.

[59] Paul Milgram and Fumio Kishino. A taxonomy of mixed reality visual displays. *IEICE TRANSACTIONS on Information and Systems*, 77(12):1321–1329, 1994.

[60] Paul Milgram, Haruo Takemura, Akira Utsumi, and Fumio Kishino. Augmented reality: A class of displays on the reality-virtuality continuum. In *Photonics for Industrial Applications*, pages 282–292. International Society for Optics and Photonics, 1995.

[61] John T Moore, Michael WA Chu, Bob Kiaii, Daniel Bainbridge, Gerard Guiraudon, Chris Wedlake, Maria Currie, Martin Rajchl, Rajni V Patel, and Terry M Peters. A navigation platform for guidance of beating heart transapical mitral valve repair. *Biomedical Engineering, IEEE Transactions on*, 60(4):1034–1040, 2013.

[62] Diane M Muratore and Robert L Galloway. Beam calibration without a phantom for creating a 3-d freehand ultrasound system. *Ultrasound in medicine & biology*, 27(11):1557–1566, 2001.

[63] Mohammad Najafi, Narges Afsham, Purang Abolmaesumi, and Robert Rohling. Single wall closed-form differential ultrasound calibration. In *SPIE Medical Imaging*, pages 83162A–83162A. International Society for Optics and Photonics, 2012.

[64] Mohammad Najafi, Narges Afsham, Purang Abolmaesumi, and Robert Rohling. A closed-form differential formulation for ultrasound spatial calibration: Single wall phantom. *Ultrasound in medicine & biology*, 41(4):1079–1094, 2015.

[65] José L Navia and Delos M Cosgrove. Minimally invasive mitral valve operations. *The Annals of thoracic surgery*, 62(5):1542–1544, 1996.

[66] John A Nelder and Roger Mead. A simplex method for function minimization. *The computer journal*, 7(4):308–313, 1965.

[67] Catherine M Otto and Alan S Pearlman. Textbook of clinical echocardiography. 2004.

[68] Terry Peters and Kevin Cleary. *Image-Guided Interventions: Technology and Applications*. Springer Science & Business Media, May 2008.

[69] Tony C Poon and Robert N Rohling. Comparison of calibration methods for spatial tracking of a 3-d ultrasound probe. *Ultrasound in medicine & biology*, 31(8):1095–1108, 2005.

[70] Richard W Prager, RN Rohling, AH Gee, and Laurence Berman. Rapid calibration for 3-d freehand ultrasound. *Ultrasound in medicine & biology*, 24(6):855–869, 1998.

[71] Ardawan Julian Rastan, Hartmuth Bruno Bittner, Jan Fritz Gummert, Thomas Walther, Claudia V Schewick, Evaldes Girdauskas, and Friedrich Wilhelm Mohr. On-pump beating heart versus off-pump coronary artery bypass surgeryevidence of pump-induced myocardial injury. *European journal of cardio-thoracic surgery*, 27(6):1057–1064, 2005.

[72] Stephen M Robinson. Fitting spheres by the method of least squares. *Communications of the ACM*, 4(11):491, 1961.

[73] François Rousseau, Pierre Hellier, and Christian Barillot. Confhusius: A robust and fully automatic calibration method for 3d freehand ultrasound. *Medical image analysis*, 9(1):25–38, 2005.

[74] Yoshifumi Saijo, Motonao Tanaka, Hiroaki Okawai, Hidehiko Sasaki, Shin-Ichi Nitta, and Floyd Dunn. Ultrasonic tissue characterization of infarcted myocardium by scanning acoustic microscopy. *Ultrasound in medicine & biology*, 23(1):77–85, 1997.

[75] Adam E. Saltman. Minimally Invasive Surgery for Atrial Fibrillation. *Seminars in Thoracic and Cardiovascular Surgery*, 19(1):33–38, 2007.

[76] Michael A Savitt, Taranpreet Singh, Guangqiang Gao, and Aftab Ahmed. Mitral valve repair on the beating perfused heart. *Asian Cardiovascular and Thoracic Annals*, 14(3):252–253, 2006.

[77] D. P. Shattuck, M. D. Weinshenker, S. W. Smith, and O. T. von Ramm. Explososcan: a parallel processing technique for high speed ultrasound imaging with linear phased arrays. *The Journal of the Acoustical Society of America*, 75(4):1273–1282, April 1984.

[78] C. D. Side and R. G. Gosling. Non-surgical Assessment of Cardiac Function. *Nature*, 232(5309):335–336, July 1971.

[79] Jeffrey A. Skiles and Brian P. Griffin. Transesophageal Echocardiographic (TEE) Evaluation of Ventricular Function. *Cardiology Clinics*, 18(4):681–697, November 2000.

[80] GEORGE D Stetten, TAKAHIRO Ota, CHIKAI J Ohazama, CRAIG Fleishman, JOHN Castellucci, JOHN Oxaal, THOMAS Ryan, J Kisslo, and OT von Ramm. Real-time 3d ultrasound: A new look at the heart. *Journal of Cardiovascular Diagnosis and Procedures*, 15(2):73–84, 1998.

[81] Sreekumar Subramanian, Joerg Seeburger, Thilo Noack, and Friedrich W. Mohr. Future Perspectives in Minimally Invasive Cardiac Surgery. *Texas Heart Institute Journal*, 38(6):678–679, 2011.

[82] K.E. Thomenius. Evolution of ultrasound beamformers. In *, 1996 IEEE Ultrasonics Symposium, 1996. Proceedings*, volume 2, pages 1615–1622 vol.2, November 1996.

[83] RS Thompson and LS Wilson. The effect of variations in transducer position and sound speed in intravascular ultrasound: A theoretical study. *Ultrasound in medicine & biology*, 22(6):719–734, 1996.

[84] David H. Tian, Beth Croce, and Rebecca Harris. Minimally invasive mitral valve surgery. *Annals of Cardiothoracic Surgery*, 2(6):857, November 2013.

[85] Jason W Trobaugh, Darin J Trobaugh, and William D Richard. Three-dimensional imaging with stereotactic ultrasonography. *Computerized Medical Imaging and Graphics*, 18(5):315–323, 1994.

[86] Annette Vegas. *Perioperative Two-Dimensional Transesophageal Echocardiography: A Practical Handbook*. Springer Science & Business Media, 2011.

[87] Annette Vegas, Massimiliano Meineri, and Angela Jerath. Real-Time Three-Dimensional Transesophageal Echocardiography: A Step-by-Step Guide. *Springer eBooks*, 2012.

[88] Marcel Vollroth, Joerg Seeburger, Jens Garbade, Bettina Pfannmueller, David Holzhey, Martin Misfeld, Michael A. Borger, and Friedrich W. Mohr. Minimally invasive mitral valve surgery is a very safe procedure with very low rates of conversion to full sternotomy. *European Journal of Cardio-Thoracic Surgery*, page ezs195, May 2012.

[89] John G. Webb, Lukas Altwegg, Robert H. Boone, Anson Cheung, Jian Ye, Samuel Lichtenstein, May Lee, Jean Bernard Masson, Christopher Thompson, Robert Moss, Ron Carere, Brad Munt, Fabian Nietlispach, and Karin Humphries. Transcatheter Aortic Valve Implantation Impact on Clinical and Valve-Related Outcomes. *Circulation*, 119(23):3009–3016, June 2009.

[90] Jay B West, J Michael Fitzpatrick, Steven A Toms, Calvin R Maurer Jr, and Robert J Maciunas. Fiducial point placement and the accuracy of point-based, rigid body registration. *Neurosurgery*, 48(4):810–817, 2001.

[91] Andrew Donald Wiles. *Navigation accuracy of image-guided interventional systems*, volume 70. 2009.

[92] Kevin Wilson, Gerard Guiraudon, Douglas L Jones, and Terry M Peters. Mapping of cardiac electrophysiology onto a dynamic patient-specific heart model. *Medical Imaging, IEEE Transactions on*, 28(12):1870–1880, 2009.

[93] Ziv Yaniv, Pezhman Foroughi, Hyun-Jae Kang, and Emad Boctor. Ultrasound calibration framework for the image-guided surgery toolkit (igstk). In *SPIE Medical Imaging*, pages 79641N–79641N. International Society for Optics and Photonics, 2011.

Curriculum Vitae

Name: Azharhosein Faraz

**Post-Secondary
Education and
Degrees:**   Aligarh Muslim University
                    Aligarh, UP, India
                    B.Tech Electronics and
                    Communication Engineering, (2011)

                    Western University
                    London, Ontario, Canada
                    Hon. Specialization in Medical Biophysics,
                    Physical Science Concentration, (2014)

**Honours and
Awards:**   Western Graduate Research Scholarship
                    Western University
                    2014-2016

                    Koh Young/ISCAS Young Investigator scholarship
                    Barcelona, Spain
                    2015

**Related Work
Experience:**   Graduate Teaching Assistant
                    Programming fundamentals for Engineers, C++
                    Dept. of Electrical and computer Engineering
                    Western University
                    2014-2015

Publications:

AH Faraz, TM Peters, ECS Chen. Automatic Real-Time Intra-operative 2D Bi-plane Ultrasound Calibration During In Situ Minimal Invasive Heart Surgery. *International Journal of Computer Assisted Radiology and Surgery*, 10(Supp. 1)-2015.

Talks:

Podium Presentation in *19th Annual Conference of International Society of Computer Assisted Surgery*, Barcelona, Spain (2015).

Posters:

Imaging Network Ontario (IMNO) 2016, Toronto, Ontario.
London Health Research Day (LHRD) 2016, Toronto, Ontario.
Imaging Network Ontario (IMNO) 2015, London, Ontario.
London Health Research Day (LHRD) 2015, London, Ontario.